Energy and Emissions Conscious Optimal Following for Automated Vehicles with Diesel Powertrains

by

Chunan Huang

A dissertation submitted in partial fulfillment
of the requirements for the degree of
Doctor of Philosophy
(Mechanical Engineering)
in the University of Michigan
2021

Doctoral Committee:

Associate Research Scientist Tulga Ersal, Co-Chair
Professor Anna G. Stefanopoulou, Co-Chair
Professor Ilya Kolmanovsky
Dr. Rasoul Salehi, General Motors
Associate Professor Ramanarayan Vasudevan

Chunan Huang
huangchu@umich.edu
ORCID iD: 0000-0003-2507-1705

DEDICATION

To my parents and my husband, for their love and support.

ACKNOWLEDGMENTS

First and foremost, I want to thank my advisors and committee co-chairs, Prof. Anna Stefanopoulou and Dr. Tulga Ersal. I am very grateful for their trust when they decided to hire me and provided me the opportunity to work on their project 5 years ago, as well as for the enormous help, support and encouragement throughout the process both in high-level and in detail. I would not be able to go this far without them.

I want to thank the National Science Foundation for providing financial support for this research under Grant Number 1646019; Division of Computer and Network Systems.

I would like to express a special thanks to Dr. Rasoul Salehi for serving on my committee, and for his guidance and patience when we collaborate closely on the projects. I would also like to thank Prof. Ram Vasudevan and Prof. Ilya Kolmanovsky for serving on my committee and providing valuable feedback.

Next, I would like to thank Dr. Michiel Van Nieuwstadt, specialist Brien Fulton and Dr. Cory Hendrickson for generous help and inspiring discussions since the start of this research, together with Dr. Michael Hopka for providing me a valuable internship opportunity at Ford Motor Company. This internship experience stimulated later development of my thesis content.

I am also extremely grateful to associate research scientist John Hoard, my labmates Mitchell Bieniek and Saravanan Duraiarasan for teaching and helping me with labwork, experiments and inspiring discussions, Prof. Andre Boehman for allowing me to use the equipment in the lab for my experiments, Charles Solbrig, Courtney Videchak, Rinav Pillai, Bill Kirkpatrick for assistance with engine tests. I also feel lucky to be a member of the powertrain control lab and spend time with my excellent labmates Shima Nazari, Niket Prakash, Bryan Maldonado, Robert Middleton, Rani Kiwan, Di Chen, Eunjeong Hyeon, Ting Cai, Miriam Figueroa-Santos, Suhak Lee, Peyman Mohtat, Joe Drallmeier, Omar Ahmed, Sravan Pannala.

Finally, I would like to thank my dear parents, Yongli Huang and Huiyun Gao, and my beloved husband, Dan Zhao. Your love, support and company are most valuable to me throughout the entire process. I want to also thank my husband's and my pets, my guinea pigs Juanjuan, MaoQiu, Xiaomao, Jianjian and Xiao Xiaolian, his tortoise Cai Bangbang and Cai Yeye for all the fun you have provided.

TABLE OF CONTENTS

LIST OF FIGURES

FIGURE

LIST OF TABLES

TABLE

ABSTRACT

The emerging application of autonomous driving provides the benefit of eliminating the driver from the control loop, which offers opportunities for safety, energy saving and green house gas emissions reduction by adjusting the speed trajectory. The technological advances in sensing and computing make it realistic for the vehicle to obtain a preview information of its surrounding environment, and optimize its speed trajectory accordingly using predictive planning methods. Conventional speed following algorithms usually adopt an energy-centric perspective and improve fuel economy by means of reducing the power loss due to braking and operating the engine at its high fuel efficiency region. This could be a problem for diesel-powered vehicles, which rely on catalytic aftertreatment system to reduce overall emissions, as reduction efficiency drops significantly with a cold catalyst that would result from a smoother speed profile.

In this work, control and constrained optimization techniques are deployed to understand the potential for and achieve concurrent reduction of fuel consumption and emissions. Trade-offs between fuel consumption and emissions are shown using results from a single objective optimal planning problem when the calculation is performed offline assuming full knowledge of the whole cycle. Results indicate a low aftertreatment temperature when energy-centric objectives are used, and this motivates the inclusion of temperature performance metric inside the optimization problem.

An online optimal speed planner is then designed for concurrent treatment of energy and emissions, with a limited but accurate preview information. An objective function comprising an energy conscious term and an emissions conscious term is proposed based on its effectiveness of 1) concurrent reduction of fuel and emissions, 2) flexible balancing between the emphasis on fuel saving or emissions reduction based on performance requirements and 3) low computational complexity and ease of numerical treatment. Simulation results of the online optimal speed planner over multiple drive cycles are presented, and for the vehicle simulated in this work, concurrent reduction of fuel and emissions is demonstrated using a specific powertrain, when allowing flexible modification of the drive cycle. Hardware-in-the-loop experiment is also performed over the Federal Test Procedure (FTP) drive cycle, and shows up to 15% reduction in fuel consumption and 70% reduction in NOx emissions when allowing a flexible following distance.

Finally, the stringent requirement of accurate preview information is relaxed by designing a

robust re-formulation of the energy and emissions conscious speed planner. Improved fuel economy and emissions are shown while satisfying the constraints even in the presence of perturbations in the preview information. A Gaussian mixture regression-based speed prediction is applied to test the performance of the speed following strategy without assuming knowledge of the preview information. A performance degradation is observed in simulation results when using the predicted velocity compared with an accurate preview, but the speed planner preserves the capability to improve fuel and tailpipe emissions performance compared with a non-optimal controller.

CHAPTER 1

Introduction

1.1 Background

An urgent need of the 21st century is to address the global climate change. According to [10], atmospheric concentrations of carbon dioxide (CO_2), the majority of green house gas (GHG) emissions, has risen 35% since the beginning of the industrial revolution, 10% of which coming from road transportation. To reduce GHGs and mitigate the potential harm from a warming planet, vehicle manufacturers and researchers have made significant improvements in fuel efficiency. Driver behaviors such as avoiding braking, delays caused by stops as well as lowering acceleration levels have been shown to yield lower fuel consumption [23], which in turn generates lower CO_2. Unfortunately, always driving with best fuel consumption performance is not a possible solution in urban traffic, as the actual driving behavior is determined by complex interactions of many factors such as the human driver and the traffic environment. Being studied and developed since the mid-1980s, self-driving car techniques provide the benefit of eliminating the driver from the control loop, and offer more opportunities for energy saving and GHGs reduction [84]. If aided with vehicle-to-vehicle (V2V) or vehicle-to-infrastructure (V2I) communication [79, 8, 73, 61, 39, 53, 57], the automated vehicle could be capable of perceiving the environment better and automated driving assistance systems such as adaptive cruise controllers could provide opportunities to reduce fuel consumption and emissions by adjusting the speed of the vehicle for foreseen, near-future events. This smooth driving style computed using route and/or traffic forecasting information to have min-

imal energy and thus reduced fuel consumption is usually referred to as "eco-driving" [27].

Besides CO_2 emissions, NOx emissions are also generated during vehicle operation due to the high gas temperature behind the flame inside the cylinders when combustion happens [35]. NOx emissions can lead to adverse health impacts from ground-level ozone and microscopic airborne particles. Environmental Protection Agency (EPA) imposes NOx standards on passenger cars and trucks, and these standards have been revised over time [82] to protect public health and as a response to the Clean Air Act. For heavy-duty diesel engines in the U.S., real-world driving emissions (RDE) tests are already a part of emissions regulations. The test procedure requires measurement of in-use emissions while these heavy-duty diesel engines are operated within a broad range of speed and load points (the Not-To-Exceed Control Area), as well as under normal vehicle operation conditions [1]. The time averaged emissions are compared to the standard to be compliant with the regulation.

1.1.1 Fuel Economy Benefits from Automated Vehicles

Advanced driver assistance systems (ADAS) have been developed in recent decades to enhance driving comfort, reduce driving errors, improve safety, increase traffic capacity and reduce fuel consumption for vehicles driving in traffic. Among the multiple functionalities, cruise controller (CC) and adaptive cruise controller (ACC) are two of the most popular and widely available techniques for longitudinal control [90]. Cruise controller, which tracks a constant reference speed, does not rely on perception of environmental information [90]. Adaptive cruise controller, which is an enhanced version of cruise controller, was first launched by Daimler Chrysler at the Paris motor show in 1998 [58, 3]. It typically relies on radar to measure the distance gap between vehicles, and aims at maintaining a reference speed whilst keeping a minimum time-headway [58]. Although the initial goal of ACC was to offer driver comfort support, field tests showed that a well-designed ACC controls the vehicle with much less rapid acceleration transients, fuel consumption and vehicle emissions than a human driver [58, 90].

The next advancement happened when connectivity was present in vehicles. This is also re-

ferred to as cooperative adaptive cruise control (CACC), where vehicle-to-vehicle (V2V) communication is used in coordination of multiple vehicles starting from sharing feedback information obtained by in-vehicle sensors [5], enabling shorter headway time and formation of platoons (i.e., vehicles driving closely behind each other) [27, 5], leading to reduced air drag and increased fuel savings [92, 5]. CACC usually takes a centralized approach, while connected cruise control (CCC) is not cooperative, where vehicles exploit information for their own advantage [27]. Information from vehicle-to-infrastructure (V2I) communication and V2V communication is available to automated vehicles with higher level of connectivity, which may include information of traffic and signalized intersections, and (a potentially forecast) vehicle acceleration information that provides the intents of surrounding vehicles [27]. This information allows the vehicle to make more significant change to its speed trajectory, and provides better safety, passenger comfort and higher fuel economy.

In such cases, model predictive control (MPC) method can be applied to solve for the optimal policy or speed trajectories. In fact, this technology provides a high chance of improvement of the performance of automated vehicles. For instance, authors of [47] show that a 10 to 20% fuel consumption reduction can be achieved with a good information for the next 10 to 15 seconds when the speed trajectory is adjusted to achieve minimal fuel consumption. With traffic signal prediction, an optimal velocity trajectory solved with deterministic dynamic programming in a receding horizon manner is used to avoid unnecessary energy loss due to speed adjustment at red lights [7]. Simulation results show a 6% increase in fuel economy on average is achieved if traffic light information is available, compared with the case when the information is not available. V2V information is also usually utilized in car-following scenarios. In such cases, the inter-vehicular distance may be adjusted to avoid abrupt acceleration and brake events and increase energy efficiency [79, 76]. Receding horizon optimization is again often used to generate the optimal velocity trajectories [76, 70, 27]. Vehicle following trajectory that is directly optimized for fuel consumption follows a pulse-and-glide strategy [75, 54], but this strategy sacrifices driver comfort. Another effective objective is to penalize acceleration and deceleration [70], which, in addition to reduced energy

use, gives a much smoother and thus comfortable driving style. The effect of reduced acceleration and deceleration on improving fuel efficiency was demonstrated in [70], where the controller was tested using different drive cycles on an Advanced Light-Duty Powertrain and Hybrid Analysis Tool developed for a 2013 Ford Escape with a 1.6L EcoBoost engine.

1.1.2 Emissions Reduction Techniques for Diesel Powered Vehicles

NOx emissions reduction is a crucial performance metric for a vehicle, which is strictly required by federal organizations [82]. Exhaust gas re-circulation (EGR) is a technique to reduce the formation of NOx inside cylinders and is used in many engine control systems. EGR affects NOx formation mainly through reduced flame temperature - by recycling the exhaust gas and diluting the engine intake, it increases the heat capacity of the cylinder charge per unit mass of fuel, and reduces the flame temperature [35]. An equivalent emission minimization strategy is developed in [93] for causal minimization of CO_2 emissions in diesel engines while keeping pollutant emissions at certain levels. In [89], a model-based Integrated Emission Management (IEM) strategy is proposed to minimize operational costs including fuel consumption and diesel exhaust fluid (DEF) within emission constraints by controlling fuel consumption, EGR and Variable Turbine Geometry (VGT) valve positions.

To further reduce NOx emissions outside of the engine cylinders, many diesel vehicles are equipped with a catalytic aftertreatment system, which usually includes devices such as diesel oxidation catalyst (DOC), selective catalytic reduction (SCR) and diesel particulate filter (DPF). An example configuration of the aftertreatment system is shown in Fig. 1.1. SCR technique has been the leading de-NOx approach in recent years [45, 12]. SCR technique (also called Urea-SCR or ammonia SCR), reduces NOx by converting NOx into nitrogen and oxygen with the aid of catalyst and reactant ammonia, which is generated from urea solution (or often called diesel exhaust fluid, DEF) injected on the upstream of the SCR catalyst [42, 12]. For Cu/Zeolite SCR catalysts, 95% de-NOx efficiency is achieved between $220 - 320^{\circ}$C during laboratory evaluation, but efficiency drops rapidly to 50% at 150°C [15]. For a given catalyst and exhaust gas with given chemical com-

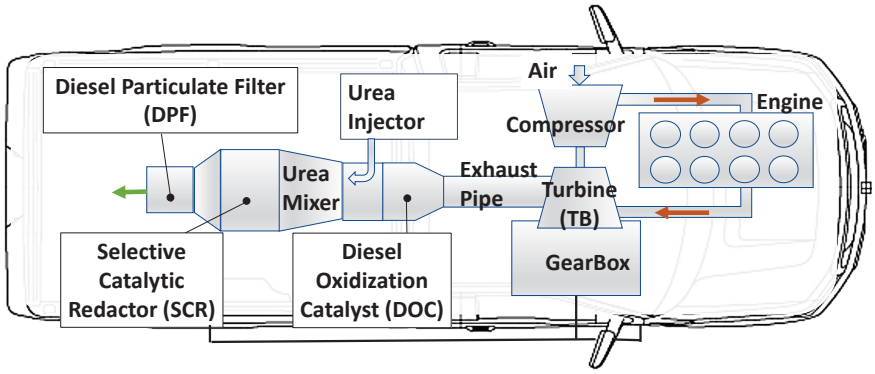

Figure 1.1: Engine and aftertreatment system configuration for 6.7L diesel engine considered in this thesis.

position, de-NOx efficiency is usually also dependent on the concentration of ammonia and mass flow rate beside temperature [42, 88, 12, 43, 17]. Although increasing the amount of ammonia by injecting more urea helps with increasing the reaction efficiency, the concern is that excessive urea injection may lead to high ammonia slip especially during large catalyst bed temperature ramps [18]. Since mass flow rate is decided majorly by the engine operation condition, reduction efficiency is usually improved through thermal management of the SCR [12, 17].

In-cylinder post fuel injection is a commonly used technique for SCR thermal management and maintaining the temperature at the high efficiency range [67, 52], however, the late injection reduces the vehicle fuel economy, as the post-injected fuel decreases combustion quality [91], or is burned in the DOC block instead of cylinder so it does not contribute to the torque output. In [16], a control-oriented thermal model is developed to capture the thermal behaviors of the aftertreatment systems with and without post-injection. The same group also proposes a coordinated active thermal management and SCR control strategy to maintain high NOx conversion efficiency and low tailpipe ammonia slip with the least post-injected fuel and urea usage for a known and fixed speed profile [17]. For hybrid vehicles, because of the extra degree of freedom introduced by the torque split ratio, fuel consumption and emissions can be successfully balanced if the effect of

aftertreatment on reducing tailpipe emissions is taken into account explicitly [46, 80].

If the vehicle torque demand is controllable, e.g., in vehicle-following scenarios when the velocity trajectory is adjusted to achieve performances benefits, it is possible to reduce engine emissions by choosing the torque demand that optimizes engine operation points. For instance, the engine raw emissions reduce inherently when full pedal accelerations are avoided [73, 69]. In [73], the authors suggest integrating the reduction of engine-out NOx emission with the fuel consumption minimization problem to find an optimal, variable distance car following policy, which results in a 13% fuel consumption reduction and 24% engine NOx emissions reduction. Similarly, velocity trajectory is optimized for a known route considering fuel consumption, trip time and total emissions constraint [69]. The problem is simplified into a multi-objective optimization problem and trade-offs between fuel and NOx is studied. Authors of [86] consider the engine emissions reduction problem for a chain of automated vehicles in a congested platoon, and show that reduced emissions and travel delay could be achieved through MPC-based longitudinal control.

1.2 Relationship to the State-of-the-Art Eco-Driving

In previous efforts in the powertrain control community, eco-driving and eco-following are majorly done to reduce engine fuel consumption via platooning, better engine efficiency, or eco-driving, especially if some preview information is available [70, 79] and the automated vehicle can follow a carefully planned, smooth trajectory to save fuel while satisfying all traffic constraints. Although low torque demand can lead to a reduced engine NOx emissions [73], little attention has been paid to the performance of the vehicle tailpipe emissions and the corresponding aftertreatment system during eco-driving. In fact, result from a comparison of real-world fuel economy and tailpipe emissions from parallel hybrid and conventional diesel buses shows that due to lower exhaust temperature, hybrid diesel buses emit higher tailpipe NOx, although the engine NOx is lower [28]. The same may also happen to the eco-following vehicle, as temperature in the aftertreatment system will drop inevitably when torque demand drops during the smoothing.

In this work, we explore the opportunity to perform a type of eco-driving such that the trajectory is not only fuel efficient, but it also yields less engine raw emissions and a well-maintained aftertreatment system activity level to reduce tailpipe NOx emissions. To achieve this, the aftertreatment system should be included in the optimal control problem. Due to the relatively large heat capacity of the turbine, the DOC and the SCR, the thermal dynamics of the aftertreatment system is very slow and subject to highly varying delays [50]. This varying delay increases the difficulty to model as well as to control the aftertreatment thermal dynamics. Although models of various levels of complexity exist for estimating the temperature (distribution) in the turbine as well as each catalyst blocks in the aftertreatment system, including multiple thermal states in the eco-driving-related optimization problem is a challenging task. Thus, some simplification of the thermal dynamics is necessary. In this thesis, we present an MPC-based speed planning algorithm with a surrogate optimization function instead of directly doing the optimization with full-order system dynamics for fuel and emissions, to reduce the computation complexity. The effectiveness of this proposed algorithm for reducing fuel consumption and tailpipe NOx in vehicle-following scenarios for connected vehicles is shown using simulation results and hardware-in-the-loop test results.

Another challenge raised from using the preview information of the leader vehicle is prediction inaccuracy. The preview information of the leader vehicle can be obtained through velocity prediction [61, 53, 37, 33] and/or V2V communication [61]. Either case presents a challenge for having an accurate preview. In the former case, it is difficult to predict the motion of the lead vehicle, as it needs to react to the movements of the other traffic participants, creating high uncertainty. In the latter case, even if the leader vehicle knows its future speed trajectory perfectly, perturbations may be applied to the information to be shared over V2V due to privacy concerns [2, 94]. Hence, achieving a robust eco-driving performance while maintaining safety is crucial.

Some researchers have recognized this challenge and shown that preview inaccuracy can have enormous impact on fuel-saving performance [61, 33]. Authors of [61] also develop a chance constrained MPC and a randomized MPC to reduce the risk of constraint violation and the fuel

consumption at the same time. Unfortunately, constraint violations still exist. To resolve the constraint violation problem, provably-correct controllers have been designed when uncertainties exist in the speed preview. Controllers presented in [63, 31] generate car-following trajectories that satisfy minimum headway specifications, and controllers in [49, 59, 44] aim at avoiding collision with front vehicle. The main method used in the literature to synthesize the correct control variables is the calculation of a robust control invariant set. Efforts typically focus only on the constraint satisfaction and only consider the vehicle kinematic performance. The only exception known to the author is the work reported in [44], where the researchers report 12% energy saving using their robust adaptive cruise controller compared with the non-optimized leader. To the best of the author's knowledge, there does not yet exist a fuel and emissions-efficient controller that is robust to errors in preview information.

In this thesis, an optimal speed controller that is robust to inaccuracies in leader velocity preview is presented. To simulate real-world driving scenarios, a realistic speed prediction is considered where the speed preview does not rely on knowledge of the future velocity profile (even partially) of the leader vehicle. Simulation results are used to demonstrate the effectiveness of the controller in reducing fuel and NOx compared with the non-optimal counterpart, as well as in guaranteeing constraint satisfaction.

1.3 Thesis Organization and Contributions

The main focus of this work is on developing an MPC application on speed planning for automated diesel vehicles in eco-following scenarios. The target is to achieve not only fuel efficiency, but also to reduce emissions for diesel vehicles with emissions aftertreatment systems. The main contributions of this thesis are summarized as follows:

- **Demonstration of fuel economy - tailpipe NOx emissions trade-offs for diesel-powered vehicles in an optimal vehicle-following scenario.**

  A control oriented vehicle and aftertreatment model is presented in Chapter 2 and is used to

calculate optimal velocity trajectories for an autonomous vehicle to follow a leader vehicle, assuming the whole trajectory of the leader is known beforehand. Constraints are imposed on the inter-vehicular distance, vehicle speed and acceleration. Four objective functions are considered including minimizing acceleration, minimizing fuel consumption, minimizing engine NOx emissions and minimizing tailpipe NOx. Dynamic programming method is applied [77] on a reduced-order model to solve the constrained trajectory optimization problem and calculate an optimal vehicle velocity profile over the temperature stabilized phase (Bag 2) of the EPA Federal Test Procedure (FTP), and fuel consumption and emissions performances are evaluated in simulation. This part of the work is presented in Chapter 3.

Chapter 2 and Chapter 3 are based on the following paper:

- Huang, C., Salehi, R. and Stefanopoulou, A.G., 2018, June. Intelligent cruise control of diesel powered vehicles addressing the fuel consumption versus emissions trade-off. In 2018 Annual American Control Conference (ACC) (pp. 840-845). IEEE [39].

- **Design of an online, real-time implementable energy and emissions conscious optimal speed planner.**

  Motivated by the work in Chapter 3, a novel MPC-based, online speed planner (called energy and emissions conscious MPC, or E^2C-MPC) is designed for concurrent treatment of energy and emissions of the connected and automated diesel vehicles in car-following scenarios. The MPC design process involves a selection of the appropriate objective function for better performance, and extensive simulation is performed to support this selection, as well as to determine its parameters for acceptable optimality and computational performance. This part of the work is presented in Chapter 4.

  Chapter 4 is based on the following paper:

  - Huang, C., Salehi, R., Ersal, T. and Stefanopoulou, A.G., 2020. An energy and emission conscious adaptive cruise controller for a connected automated diesel truck. Vehi-

cle System Dynamics, 58(5), pp.805-825 [38].

- **Hardware-in-the-loop validation with a real-time implementation of E^{2}C-MPC.**

  Experimental validation is performed using a hardware-in-the-loop setup with a Ford 6.7L V8 Powerstroke diesel engine and a stock emissions aftertreatment system from a Ford F250 medium-duty truck, allowing detailed and realistic evaluation of fuel economy, tailpipe NOx emissions as well as vehicle following metrics. A full vehicle model with longitudinal dynamics, engine dynamics, gear shift logic, and torque converter is designed and implemented. The optimal speed planner is used as a high-level planner to generate an optimal reference velocity and a PI-based cruise controller is used as a low-level controller to track the optimized speed.

  Chapter 5 is based on the following paper:

  - Huang, C., Salehi, R., Stefanopoulou, A.G., Ersal, T., Hardware-in-the-loop exploration of energy vs. emissions trade-off in eco-following scenarios for connected automated vehicles, under preparation.

- **A robust re-formulation of the energy and emissions conscious optimal speed planner to ensure satisfaction of traffic constraints with inaccurate preview information.**

  Real-world velocity prediction is hardly accurate due to prediction error. Issues raised from prediction error in real-world vehicle following scenarios are considered. To ensure satisfaction of constraints and guarantee driving safety, a robust formulation of the predictive speed controller is presented. Simulation is performed first with perturbation modeled as zero-mean Gaussian noise to show that the presented formulation is robust to inaccuracies in leader vehicle velocity and preserves the trade-off between optimizing fuel consumption and emissions. Additional simulation is performed with a realistic speed predictor based on Gaussian mixture regression, where online preview of the leader vehicle is generated only

using history velocity information. Results show effectiveness of the controller in reducing fuel and NOx compared with the non-optimal counterpart in real-world driving scenarios. This part of the work is presented in Chapter 6.

Chapter 6 is partially based on the following papers:

- Zhang, X., Huang, C., Liu, M., Stefanopoulou, A. and Ersal, T., 2019. Predictive cruise control with private vehicle-to-vehicle communication for improving fuel consumption and emissions. IEEE Communications Magazine, 57(10), pp.91-97 [94].
- Huang, C., Zhang, X., Salehi, R., Ersal, T. and Stefanopoulou, A.G., 2020, July. A Robust Energy and Emissions Conscious Cruise Controller for Connected Vehicles with Privacy Considerations. In 2020 American Control Conference (ACC) (pp. 4881-4886). IEEE [40].

CHAPTER 2

Control-Oriented Vehicle Model

A vehicle model including longitudinal dynamics, powertrain steady-state maps and the thermal dynamics of the aftertreatment system is developed for a Ford F250 medium-duty truck and is presented in this chapter. This model is used for the development of model-based controllers in later chapters, as well as simulating fuel consumption and tailpipe emissions of the vehicle.

The model structure of the studied vehicle in this thesis is shown in Fig. 1.1 in the last chapter. The aftertreatment system includes a Diesel Oxidation Catalyst (DOC), a Selective Catalytic Reduction (SCR) block, and a Diesel Particulate Filter (DPF). The vehicle model in Fig. 2.1 includes a single varying input, namely, the vehicle acceleration a_{veh}, and the key outputs are the vehicle position p_{veh}, speed v_{veh}, fuel consumption rate $\dot{m}_{\text{fuel}}$ and tailpipe NOx emissions rate $\dot{m}_{\text{NOx.TP}}$. The details of each submodel in Fig. 2.1 are described as follows.

2.1 Longitudinal Model

Assuming the vehicle as a point mass system, the vehicle state vector $\left[p_{\text{veh}}, v_{\text{veh}}\right]^T$, which comprises vehicle position and speed, is calculated using:

$$\begin{bmatrix} \dot{p}_{\text{veh}} \\ \dot{v}_{\text{veh}} \end{bmatrix} = \begin{bmatrix} 0 & 1 \\ 0 & 0 \end{bmatrix} \begin{bmatrix} p_{\text{veh}} \\ v_{\text{veh}} \end{bmatrix} + \begin{bmatrix} 0 \\ 1 \end{bmatrix} a_{\text{veh}}, \tag{2.1}$$

given the vehicle acceleration a_{veh} as the input.

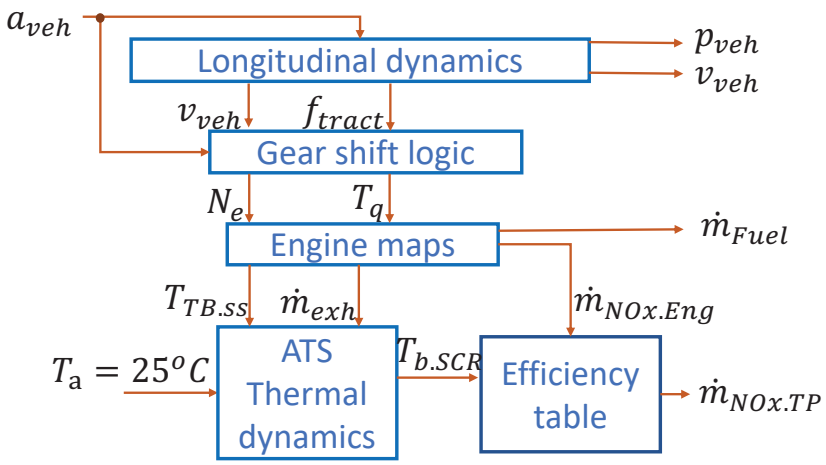

Figure 2.1: Vehicle schematic and its model structure for the diesel powered vehicle considered in this paper.

With the vehicle speed v_{veh} and acceleration a_{veh}, the demanded vehicle traction force f_{tract} is calculated using the longitudinal dynamics model:

$$f_{\text{tract}} = M_{\text{v}} a_{\text{veh}} + f_{\text{rr}} + f_{\text{air}}. \tag{2.2}$$

In (2.2), M_{v} represents the vehicle mass, and f_{rr} and f_{air} represent the rolling resistance and the air drag resistance, respectively. They are calculated as:

$$f_{\text{rr}} = C_{\text{R}}\, M_{\text{v}}\, g\, \mathbf{sgn}(v_{\text{veh}}), \tag{2.3}$$

$$f_{\text{air}} = 0.5\, \rho_{\text{air}}\, A_{\text{f}}\, C_{\text{d}}\, v_{\text{veh}}\, |v_{\text{veh}}|, \tag{2.4}$$

with C_{R} being the rolling resistance coefficient, ρ_{air} and C_{d} the air density and air drag coefficient, and A_{f} the vehicle frontal area. In this work, the effect of road grade is ignored for simplicity.

2.2 Engine Model and Gear Shift

2.2.1 Gear Shift Model

A unique gear level (GL) is assigned based on the vehicle speed v_{veh} and acceleration a_{veh} as shown in Fig. 2.2[1]. Then, the engine speed N_{e} and the calculated torque T_{q} are obtained as:

$$N_{\text{e}} = F_{\text{R}} G_{\text{R}}(GL) \frac{1}{R_{\text{w}}} v_{\text{veh}}, \tag{2.5}$$

$$T_{\text{q}} = \begin{cases} g_{\text{Tq}}(f_{\text{tract}} \frac{v_{\text{veh}}}{N_e \eta_t}), & \text{if not at idle} \\ T_{\text{idle}}, & \text{if at idle} \end{cases} \tag{2.6}$$

where F_{R}, $G_{\text{R}}(GL)$ and R_{w} represent the final drive ratio, gear ratio at present gear level GL and wheel radius, respectively, and η_t represents the lumped transmission efficiency. g_{Tq} is a mapping from the physical engine torque to the non-negative calculated torque T_{q} that the manufacturer uses as input to the look-up tables. When the vehicle is stopped, the engine idle speed is set to be 600 rpm and the engine idle torque demand is a constant number T_{idle}.

2.2.2 Engine and Efficiency Models

Fuel rate $\dot{m}_{\text{fuel}}$, exhaust flow rate $\dot{m}_{\text{exh}}$, engine out NOx emission rate $\dot{m}_{\text{NOx.Eng}}$ and steady state turbine out temperature $T_{\text{TB.ss}}$ are calculated using look-up tables mapped with engine speed N_{e} and torque T_{q}, as shown in Fig. 2.3. These maps are created, validated, and provided by the manufacturer. This calculation is based on the following three simplifying assumptions: (1) The engine air path dynamics are ignored, (2) the engine raw NOx contains only NO, and NO oxidization in diesel catalytic converter is ignored since DOC temperature is nearly always lower than 250 °C in the stabilized phase [14], (3) the SCR efficiency η_{SCR} is determined by an efficiency table for the NO conversion, based on SCR brick temperature $T_{\text{b.SCR}}$ [14]. Based on these assumptions, tailpipe

[1]This gear level map is used for the sake of study in this work, and does not represent the actual gear shift logic used in the corresponding vehicle.

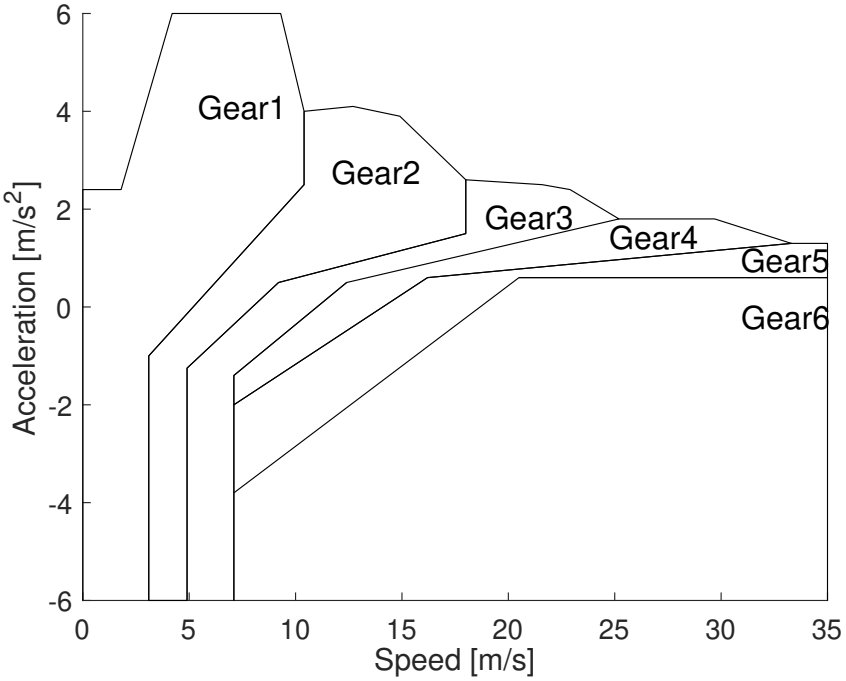

Figure 2.2: Look-up tables used to calculate engine outputs.

NOx emissions rate $\dot{m}_{\text{NOx.TP}}$ is calculated as

$$\dot{m}_{\text{NOx.TP}} = (1 - \eta_{\text{SCR}}(T_{\text{b.SCR}}))\dot{m}_{\text{NOx.Eng}}, \tag{2.7}$$

where the calculation of SCR temperature $T_{\text{b.SCR}}$ is presented in the next section.

2.3 Aftertreatment Dynamics

2.3.1 Full-Order Model

To calculate the SCR brick temperature $T_{\text{b.SCR}}$ in (2.7), a complete thermal model, including that of turbine, DOC and SCR, is needed. A first-order lag is assumed for the dynamics of the turbine outlet gas temperature T_{TB}:

$$T_{\text{TB}} = \frac{1}{1 + \tau s} T_{\text{TB.ss}}, \tag{2.8}$$

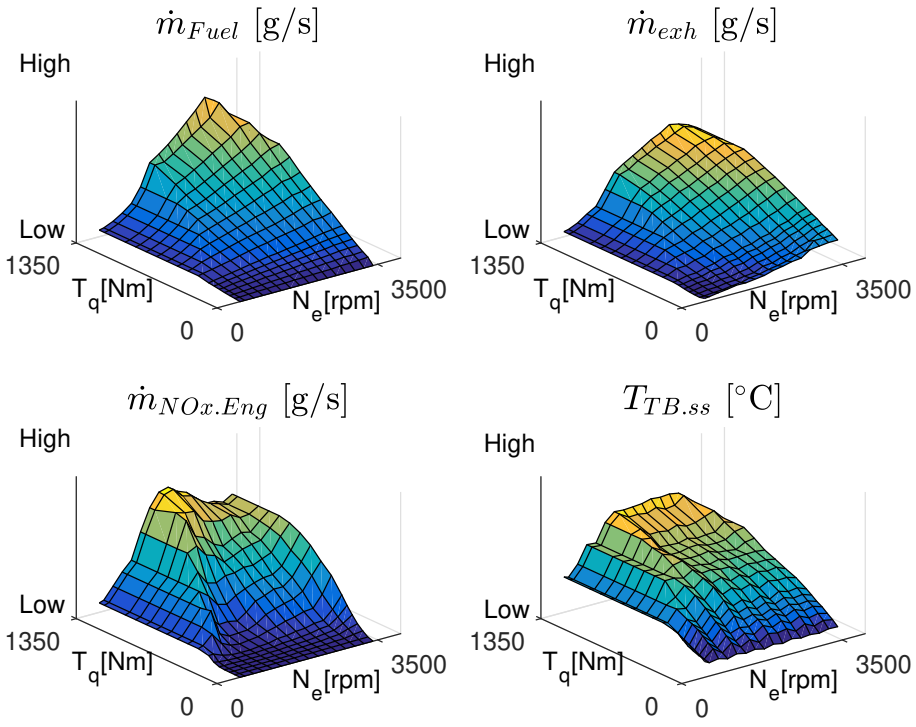

Figure 2.3: Gear shift and engine maps used in the vehicle model.

where τ is assumed to be inversely proportional to exhaust mass flow rate [16], i.e., $\tau \propto \frac{1}{\dot{m}_{\text{exh}}}$.

The DOC and SCR catalysts are modeled as thermal masses, and their thermal models are derived under the following assumptions: (1) Heat conduction from the exhaust gas into the catalytic brick is negligible compared with heat convection between them. (2) Axial heat diffusion in the fluid phase and axial conduction in the solid phase are ignored. (3) Heat capacity of the gas trapped in the catalytic brick is too small compared with that of the brick. Hence, there is no dynamics for the gas temperature inside the catalyst. (4) Heat radiations between the gas and the brick, and between the brick and the ambient are ignored based on the experimental validation results in the literature [51]. With these assumptions, the following first-order system is utilized to model the

thermal dynamics of the DOC [51, 13].

$$T_{\text{g.DOC}} = \frac{\frac{\dot{m}_{\text{exh}} C_{\text{pg}}}{V_{\text{DOC}}} T_{\text{in}_{\text{delay}}.\text{DOC}} + (h_1\alpha_1)_{\text{DOC}} T_{\text{b.DOC}}}{(h_1\alpha_1)_{\text{DOC}} + \frac{\dot{m}_{\text{exh}} C_{pg}}{V_{\text{DOC}}}}, \tag{2.9}$$

$$(1-\epsilon_{\text{DOC}})\rho_{\text{b}} C_{\text{b}} \frac{dT_{\text{b.DOC}}}{dt} = (h_1\alpha_1)_{\text{DOC}}(T_{\text{g.DOC}} - T_{\text{b.DOC}}) - (h_2\alpha_2)_{\text{DOC}}(T_{\text{b.DOC}} - T_{\text{a}}), \tag{2.10}$$

where $T_{\text{g.DOC}}$ and $T_{\text{b.DOC}}$ are the DOC outlet gas and brick temperatures, ρ_{b} and C_{b} are the density and specific heat capacity of the monolith, ϵ_{DOC} is a parameter showing the fraction of the DOC open cross sectional area [66], C_{pg} is the specific heat capacity of the exhaust gas, V_{DOC} is the volume of the catalytic brick, h_1 and h_2 are the heat convection coefficients from the gas flow to the monolith, and from the block surface to the ambient, α_1 and α_2 are the corresponding geometric surface area-to-volume ratios [66], and T_{a} is the ambient temperature, which is set to be $25°\text{C}$ in this paper. Both h_1 and h_2 are assumed to be changing linearly depending on the exhaust mass flow rate.

$T_{\text{in}_{\text{delay}}.\text{DOC}}$ in (2.9) is calculated as:

$$T_{\text{in}_{\text{delay}}.\text{DOC}}(t) = T_{\text{TB}}(t - \Delta\tau_{\text{d.DOC}}), \tag{2.11}$$

and the variable $\Delta\tau_{\text{d.DOC}}$, which causes a dead-time in DOC temperature when engine operation condition changes, is defined by the following equation and calculated using an iterative method:

$$\int_{t-\Delta\tau_{\text{d.DOC}}}^{t} \frac{C_{pg}}{A_{\text{DOC}}(1-\epsilon_{\text{DOC}})\rho_b C_b} \dot{m}_{\text{exh}} ds = c_{\text{d.DOC}}, \tag{2.12}$$

with $A_{\text{DOC}}(1-\epsilon_{\text{DOC}})$ being the cross sectional wall area of DOC brick [13]. This equation corresponds to a transport phenomenon, with the integrand being the speed of flow, and the constant parameter $c_{\text{d.DOC}}$ is the distance that heat propagates in the DOC brick. The delay time $\Delta\tau_{\text{d.DOC}}$ accounts for a residence time needed for heat to propagate into the monolith. It corresponds to a transport phenomenon according to a Plug-Flow assumption; see [13] for details. As shown in (2.9) and (2.10), the presented thermal model ignores exothermic reactions of CO and unburned

hydrocarbons with oxygen in the DOC, which happens mainly when there is in-cylinder post injection.

The same model structure is considered to calculate the SCR output gas temperature $T_{\text{g.SCR}}$ and brick temperature $T_{\text{b.SCR}}$ because of the similar physical structures of SCR and DOC.

$$T_{\text{g.SCR}} = \frac{\frac{\dot{m}_{\text{exh}} C_{pg}}{V_{\text{SCR}}} T_{\text{in}_{\text{delay}}.\text{SCR}} + (h_1\alpha_1)_{\text{SCR}} T_{\text{b.SCR}}}{(h_1\alpha_1)_{\text{SCR}} + \frac{\dot{m}_{\text{exh}} C_{pg}}{V_{\text{SCR}}}}, \tag{2.13}$$

$$(1-\epsilon_{\text{SCR}})\rho_{\text{b}} C_{\text{b}} \frac{dT_{\text{b.SCR}}}{dt} = (h_1\alpha_1)_{\text{SCR}}(T_{\text{g.SCR}} - T_{\text{b.SCR}}) - (h_2\alpha_2)_{\text{SCR}}(T_{\text{b.SCR}} - T_a), \tag{2.14}$$

$$T_{\text{in}_{\text{delay}}.\text{SCR}}(t) = T_{\text{g.DOC}}(t - \Delta\tau_{\text{d.SCR}}). \tag{2.15}$$

$\Delta\tau_{d.SCR}$ is calculated using a similar equation as (2.12) with different parameters identified for SCR. Furthermore, based on simulation results, the changes of $\dot{m}_{\text{exh}}$ and $T_{\text{in}_{\text{delay}}.\text{SCR}}$ caused by urea solution injection are found to be small and are therefore ignored in the SCR model.

2.3.2 Reduced-Order Model

Since including all the states in vehicle longitudinal model and thermal model will lead to a huge computation burden, instead of the thermal model described in Section 2.3.1, a reduced-order model with only one state is used in DP to simulate SCR temperature. In the reduced-order model, the aftertreatment system including SCR is assumed to be lumped to a thermal mass with the following dynamics:

$$T_{g.rSCR} = \frac{\frac{\dot{m}_{exh} C_{pg}}{(A\Delta x)_{rSCR}} T_{TB.ss} + (h_1 a_1)_{rSCR} T_{b.rSCR}}{(h_1 a_1)_{rSCR} + \frac{\dot{m}_{exh} C_{pg}}{(A\Delta x)_{rSCR}}} \tag{2.16}$$

$$\begin{aligned}(1-\epsilon_{rSCR})\rho_b C_b \frac{dT_{b.rSCR}}{dt} &= (h_1 a_1)_{rSCR}(T_{g.rSCR} - T_{b.rSCR}) \\ &\quad - (h_2 a_2)_{rSCR}(T_{b.rSCR} - T_a)\end{aligned} \tag{2.17}$$

where $T_{g.rSCR}$ and $T_{b.rSCR}$ represent outlet gas and brick temperature for the SCR reduced model. Compared with the original model, the reduced lumped model has only one state (instead of three) and the delay terms in (2.11) and (2.15) are ignored.

2.4 Model Validation

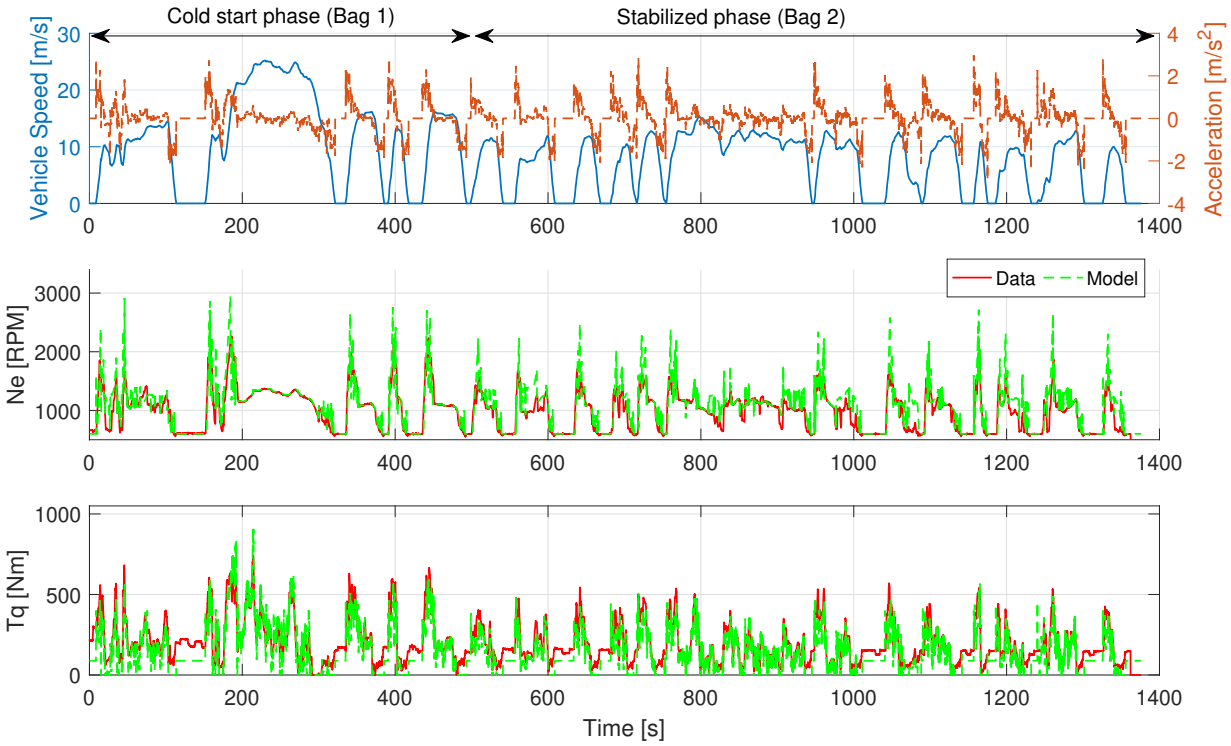

Figure 2.4: Validation results for the vehicle longitudinal model

The parameters in the above models are identified using measured vehicle speed, engine speed and torque, and aftertreatment gas temperatures for a MY2013 Ford F-250 Super-duty truck with a 6.7 L diesel engine when it is running a federal test procedure (FTP). Validation results for engine speed and torque prediction are shown in Fig. 2.4. Due to the fact that this model does not include a torque converter, the simulated engine speed and torque during transient conditions are more oscillatory than the measured variables as shown in the second and third subplots in Fig. 2.4. During slow transients and steady operation conditions, the model follows engine speed and torque

trajectory sufficiently closely for the purposes of this study.

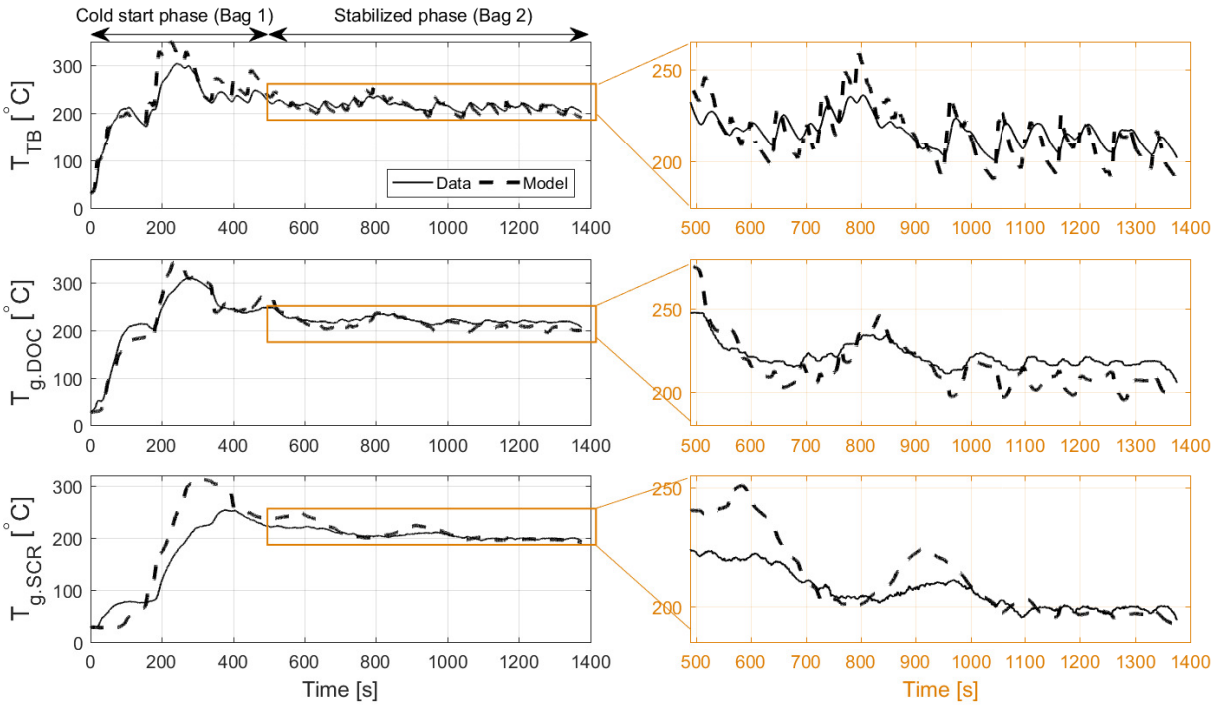

Figure 2.5: Thermal model validated over the standard FTP drive cycle.

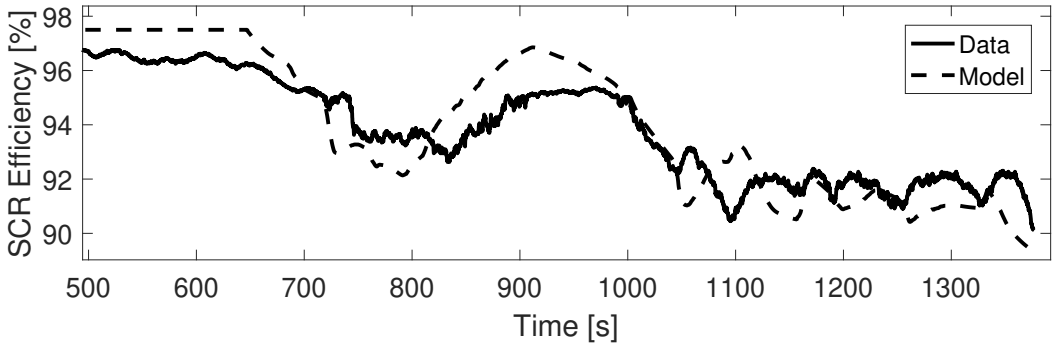

Figure 2.6: Comparison of SCR efficiency traces calculated with modeled SCR temperature and data over the standard FTP drive cycle.

Figure 2.5 shows the validation results of the aftertreatment system gas temperatures compared with real vehicle measurements. Due to the delayed structure of the thermal dynamics presented in (2.9)-(2.15), temperature histories from the cold start phase are required as initial conditions in the DOC and SCR models in the stabilized phase. Thus, in all temperature calculations in this paper,

simulations start from the starting point of the cold start phase to provide reasonable initial conditions for the stabilized phase of FTP. However, only the stabilized phase is used for comparison and verification, or for control purposes in Section 4.3. As observed, the gas temperature dynamics is effectively slowed down from T_{TB} to $T_{g.SCR}$. The thermal model sometimes misses the dynamics in Bag 1 as it does not include post-injection or water condensation effect. The root-mean-square errors for the turbine, the DOC and the SCR temperatures in Bag 2 are $9.0°$C, $10.6°$C, and $10.4°$C, respectively. SCR efficiency traces calculated using the model and the measured SCR temperature are shown in Fig. 2.6. Here we model the SCR efficiency using an efficiency table based on SCR temperature [15]. The root-mean-square error for efficiency is 1.12%. Thus, the model is considered to be accurate enough for the purpose of this thesis.

CHAPTER 3

Offline Speed Optimization Using Dynamic Programming

Vehicle autonomy, semi-autonomy, or plain driver-advisory velocity signal could assist in reducing emissions and fuel consumption by allowing a flexible speed trajectory to the autonomous vehicle in a given traffic condition. Assuming a vehicle-following traffic scenario, the follower autonomous vehicle should be able to navigate itself to stay in a distance after the leader vehicle, ensuring the driver safety and no car cuts in from other lanes. Enforcing the distance constraint, the follower's speed profile can be optimized to have minimal acceleration, so that fuel economy is improved indirectly due to the removal of acceleration spikes [70]. Other constraints such as trip time [60], road topography [81], traffic conditions [32] and traffic signals [41] can also be included in the fuel optimization to replicate all conditions that happen in real road traffic and travel missions.

Similar to the fuel economy, vehicle emissions also depend on vehicle velocity and how the autonomous vehicle follows the leader. An aggressive acceleration, for example, generates a peak in the engine out emissions which can challenge the clean-up capability of the vehicle aftertreatment system. With the traffic preview, the vehicle might be driven such that the engine raw emissions are low or/and the aftertreatment system is active enough to keep the tailpipe emissions, such as NOx, within regulation limits. NOx emissions reduction in modern diesel engines heavily relies on a Selective Catalytic Reduction (SCR) aftertreatment system [62]. The SCR catalyst uses a reducing agent, ammonia (NH_3), to react with NOx and reduce it to nitrogen and oxygen, and its

efficiency is highly dependent on catalyst brick temperature. For example, a Cu/Zeolite based SCR system has more than 95% efficiency in the range [220-320] °C, while the efficiency drops to 60% at 150 °C and is only 20% at 130 °C [14]. Therefore, it is critical to control the aftertreatment temperature as well as the engine raw emissions to reduce the vehicle tailpipe (TP) emissions, both dependent on the driving style.

The engine raw emissions reduce inherently when full pedal accelerations are avoided [73], however, tailpipe emissions also depend on the aftertreatment system performance and its control. In-cylinder post fuel injection is a common technique used to increase SCR temperature [67], [52], however, the late injection reduces the vehicle fuel economy. In [17], a coordinated active thermal management is applied to control post-injection and urea injection into SCR for reducing 97.8% of engine out NOx emissions while satisfying NH_3 slip requirements in a known and fixed speed profile. For hybrid electric vehicles, combustion engines and electric motors can be coordinated by the energy management to optimize fuel economy and tailpipe emissions for a given drive cycle by choosing torque split ratio [80], [46]. In all aforementioned works the aftertreatment system is controlled when the vehicle speed profile is assumed as a fixed trajectory with limited violation boundary permitted by the standard FTP test, and modifications are made inside the engine, aftertreatment system, or the torque split demand is changed if for hybrid vehicles. Less works have been done to approach the problem through modification of the velocity trajectory. In [73], a following distance corridor is considered to optimize speed profile for better fuel economy and diesel engine emissions. Through reducing fast transients of pedal input, their experimental results showed 24% engine NOx reduction with 13% fuel consumption reduction. However, performance of aftertreatment was not included in their work.

In this chapter, an optimal car-following scenario is used to study fuel economy-tailpipe NOx emissions trade-offs, assuming an SCR aftertreatment system. The leader vehicle is scheduled to transverse the standard FTP drive cycle, and the following vehicle is an autonomous diesel vehicle. Optimal speed trajectory for the following vehicle is calculated, and multiple key performances are utilized as objective functions, including acceleration, fuel consumption, engine NOx and tailpipe

NOx emissions. The model presented in Chapter 2 is applied to evaluate the resulting fuel consumption and emissions performances, and dynamic programming method [77] is applied to find the global optimal solution of the above optimization problems.

The main contribution of this chapter is to demonstrate a clear fuel economy-NOx emissions trade-off and indicate the importance of the aftertreatment system in optimal vehicle-following scenarios. This observation will motivate formulation of a fuel and tailpipe emissions co-optimization problem, as well as the change to solve the optimal velocity trajectory using a causal methodology in later chapters.

The content of this chapter has been presented in [39],

- Huang, C., Salehi, R. and Stefanopoulou, A.G., 2018, June. Intelligent cruise control of diesel powered vehicles addressing the fuel consumption versus emissions trade-off. In 2018 Annual American Control Conference (ACC) (pp. 840-845). IEEE.

3.1 Problem Formulation

We consider a car-following scenario where the ego vehicle, which is automated, follows a leader vehicle and optimizes its velocity trajectory utilizing information of the future motion of the leader vehicle. To explore the benefit of autonomy while making the ego vehicle follow the leader with a relatively short distance, spacing constraint on the following distance are imposed to mimic the traffic constraints to avoid rear end collisions and keep the following distance from being too long to avoid frequent cut-ins from adjacent lanes. Any following trajectories that satisfy this spacing constraint are considered feasible.

In this chapter, it is assumed that the whole drive cycle of the leader vehicle is available to the ego follower, such that it can perform offline computation to calculate its preferred velocity trajectory.

3.2 Optimal Control Problem Formulation

The speed trajectory of the autonomous vehicle is optimized when it is following a leader vehicle driving the standard FTP drive cycle. The optimization minimizes one of these four objectives: acceleration, fuel consumption, engine raw NOx emission and tailpipe emission. The following vehicle is designed to drive exactly the FTP cycle during the cold start phase in all optimization cases where post injection and other warm up control strategies are active. Thus, the speed optimization only considers the second phase of the FTP. To simulate real traffic conditions, upper and lower limits of the following vehicle position are defined based on the leader vehicle position and speed, and used as a constraint in the optimization.

The dynamic programming function from MATLAB [77] is used to solve the speed trajectory optimization problem. Dynamic programming method is subject to the curse of dimensionality, which in this context means that the computation complexity grows exponentially with the number of states and inputs. To reduce the number of states included in the system, the reduced-order model presented in Section 2.3.2 is utilized when solving for the optimal trajectories.

Four optimization scenarios are tested with a single objective function in each case as:

$$\min_{\{a_{veh}(k)\}_{k=0}^{N}} \quad J_i(x) = \sum_{k=0}^{N} C_i(k), \quad i = 1, 2, 3, 4 \tag{3.1a}$$

$$\text{subject to} \quad -6 \text{ m/s}^2 \leq a_{veh}(k) \leq 6 \text{ m/s}^2 \tag{3.1b}$$

$$\underline{p}(v_l(k)) \leq p_{veh}(k) \leq \bar{p}(v_l(k)) \tag{3.1c}$$

$$\bar{p}(v_l(k)) = p_l - v_l \cdot \Delta t_L \tag{3.1d}$$

$$\underline{p}(v_l(k)) = p_l - \begin{cases} v_l d_{max} & \text{if } v_l < 20 \text{ MPH} \\ v_l d_{min} & \text{otherwise} \end{cases} \tag{3.1e}$$

$$0 \leq v_{veh}(k) \leq 67 \text{ MPH} \tag{3.1f}$$

$$150^{\circ}\text{C} \leq T_{b.rSCR}(k) \leq 300^{\circ}\text{C} \tag{3.1g}$$

$$\text{System dynamics and constraints (2.1)-(2.8)} \tag{3.1h}$$

$$\text{for } k = 0,1, ..., N_{\text{P}} - 1. \tag{3.1i}$$

System dynamics (2.1)-(2.8), (2.16)-(2.17) discretized using $dT = 0.1$ s, with a zero-order hold on input a_{veh}. In above, $k = 0$ and N represent the starting step and ending step of the stabilized phase in FTP, p_l and v_l are the position and velocity of the leader vehicle, Δt_L is selected proportional to the vehicle length, d_{max} and d_{min} are selected 10 ft/MPH and 4 ft/MPH. $\bar{p}(v_l(k))$ is the closest position of follower car considered for safety and $\underline{p}(v_l(k))$ is the farthest position that would prevent cut-ins from other lines [70]. Table 3.1 describes the cost function used in each optimization scenario and its corresponding states.

Table 3.1: Cost functions defined for optimization scenarios

Objective	Cost function	States
(optimal) acceleration	$C_1(k) = a_{veh}(k)^2$	$[p_{veh}, v_{veh}]^T$
(optimal) fuel or MPG	$C_2(k) = m_f(k)$	$[p_{veh}, v_{veh}]^T$
(optimal) Engine NOx	$C_3(k) = m_{\text{NOx.Eng}}(k)$	$[p_{veh}, v_{veh}]^T$
(optimal) TP NOx	$C_4(k) = m_{\text{NOx.TP}}(k)$	$[p_{veh}, v_{veh}, T_{b.rSCR}]^T$

Finally, inputs and states are discretized before applying DP with grid sizes

$$\text{Input: } \Delta a_{veh} = 0.5 \text{ m/s}^2, \tag{3.2a}$$

$$\text{States: } \begin{cases} \Delta p_{veh} = \frac{\bar{p}(v_l(k)) - \underline{p}(v_l(k))}{30} \text{ m} \\ \Delta v_{veh} = \frac{1}{4} \text{ m/s} \\ \Delta T_{b.rSCR} = 3 \text{ °C}. \end{cases} \tag{3.2b}$$

3.3 Results

Table 3.2: Effect of optimization objective on major vehicle outputs

Objective	Orig.	Acce.	Fuel	Eng. NOx	TP NOx
MPG	16.3	18.2	19.3	19.2	13.7
Engine NOx [g]	5.20	3.50	8.09	3.24	5.47
Tailpipe NOx [g]	0.342	0.388	0.664	0.385	0.141
NOx Reduction [%]	93.4	88.9	91.8	88.1	97.4
Urea Solution [g]	14.2	9.10	21.7	8.33	15.6

The following autonomous vehicle is simulated with the optimized speed profile for each of the four scenarios listed in Table 3.1. Main results for the two extreme cases, namely least fuel and least TP emissions, are shown in Fig. 3.1. Detailed key results including the vehicle fuel

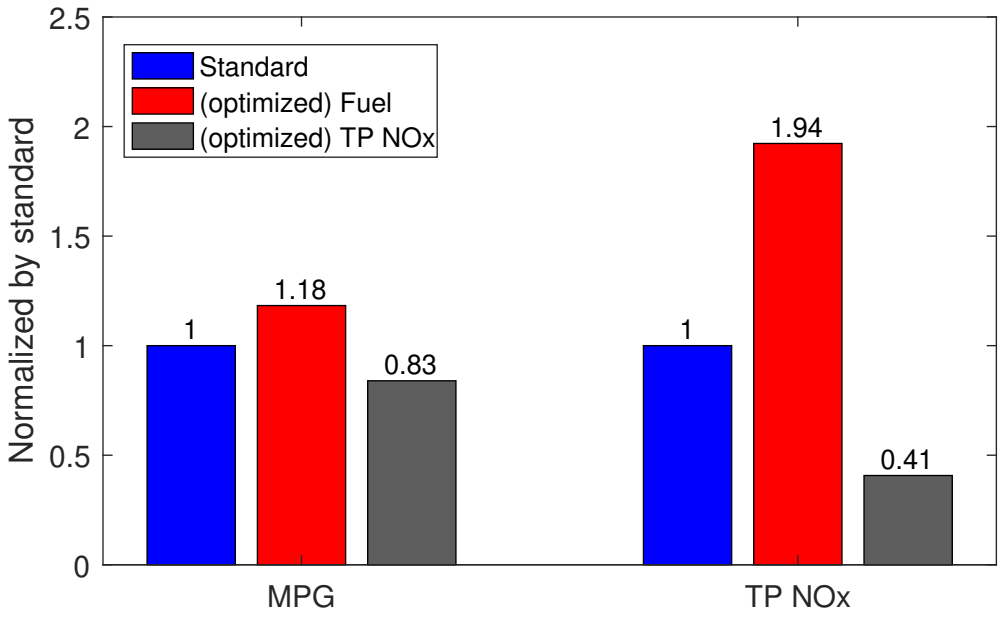

Figure 3.1: Summary of the fuel & TP NOx optimization results normalized by the standard FTP drive cycle

economy (in MPG), engine raw emissions, NOx reduction rate, and tailpipe emissions are listed in Table 3.2 for all four cases. As plotted in Fig. 3.1, MPG in fuel optimized scenario is 18% higher than the standard baseline, but tailpipe NOx is almost doubled; while directly optimizing tailpipe emission decreases NOx 59% compared to the standard with 17% less fuel efficiency. Therefore, a complete trade-off exists between the vehicle fuel economy and emissions such that improving one deteriorates another.

Speed trajectories for the four scenarios in Table 3.1 and the standard driving are shown in Fig. 3.2. As shown, all four optimization scenarios recommend a relatively constant speed over [690-710] s. When the fuel is minimized, a pulse and glide speed trajectory is generated. This commands the engine to operate with high torque as is shown in visitation plot in Fig. 3.3-(d). The engine, however, generates very high amount of NOx at high torque conditions, specifically if the engine speed is low (Fig. 3.3-(b)). This is the reason that raw emissions increase with fuel optimized drive cycle as shown in Table 3.2.

SCR temperature traces for all five cases are shown in Fig. 3.4 along with 97.5%, 95% and

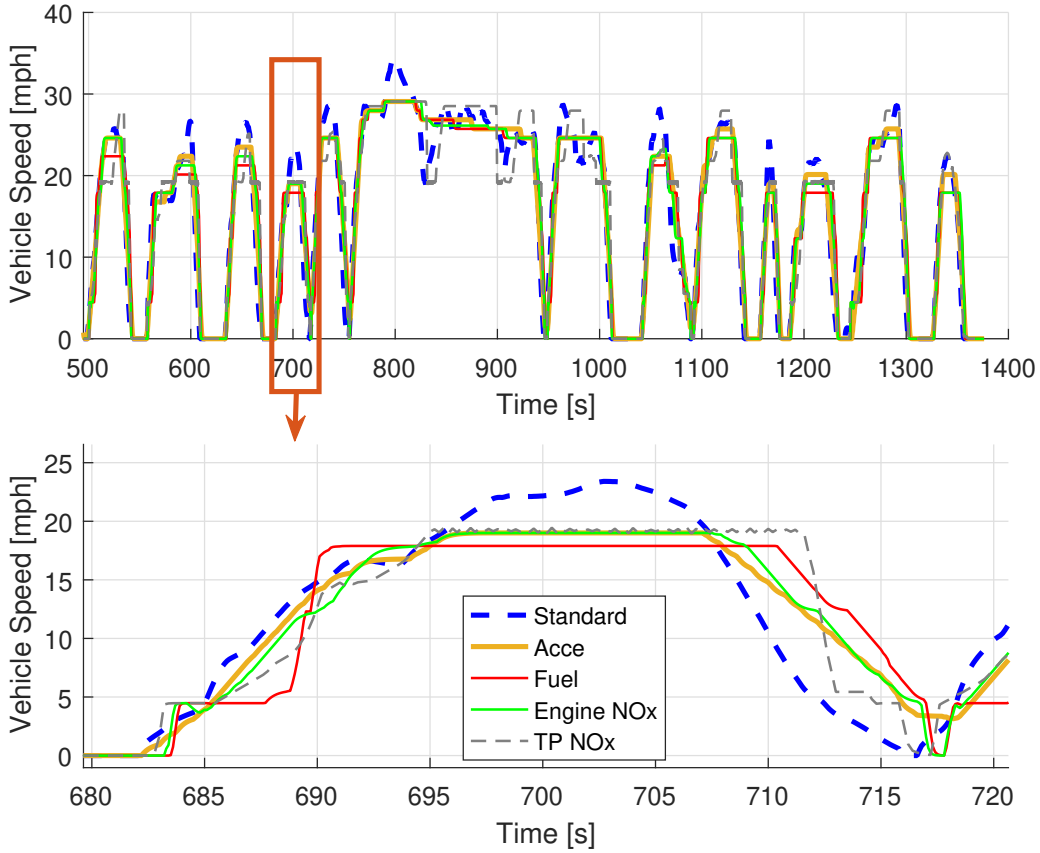

Figure 3.2: Comparison between the standard and optimized vehicle speed trajectories

85% SCR efficiency levels. As observed, the SCR temperature and consequently its efficiency are low when only the fuel economy is optimized. The low SCR efficiency together with the high raw engine emissions are reasons that the tailpipe NOx is doubled compared to the standard FTP driven speed profile as Table 3.2 shows. From Fig. 3.4 it is observed that maintaining high temperature for the SCR is required to minimize the tailpipe NOx emissions. To increase the SCR temperature, DP designs the vehicle speed such that the turbine out temperature rises as verified by $T_{\text{TB.ss}}$ distribution shown in Fig. 3.5. The cost for this high SCR temperature, however, is higher fuel consumption since the high $T_{\text{TB.ss}}$ points are not necessarily located in high engine efficiency regions.

Finally, results from the acceleration and engine NOx minimized optimizations are found to

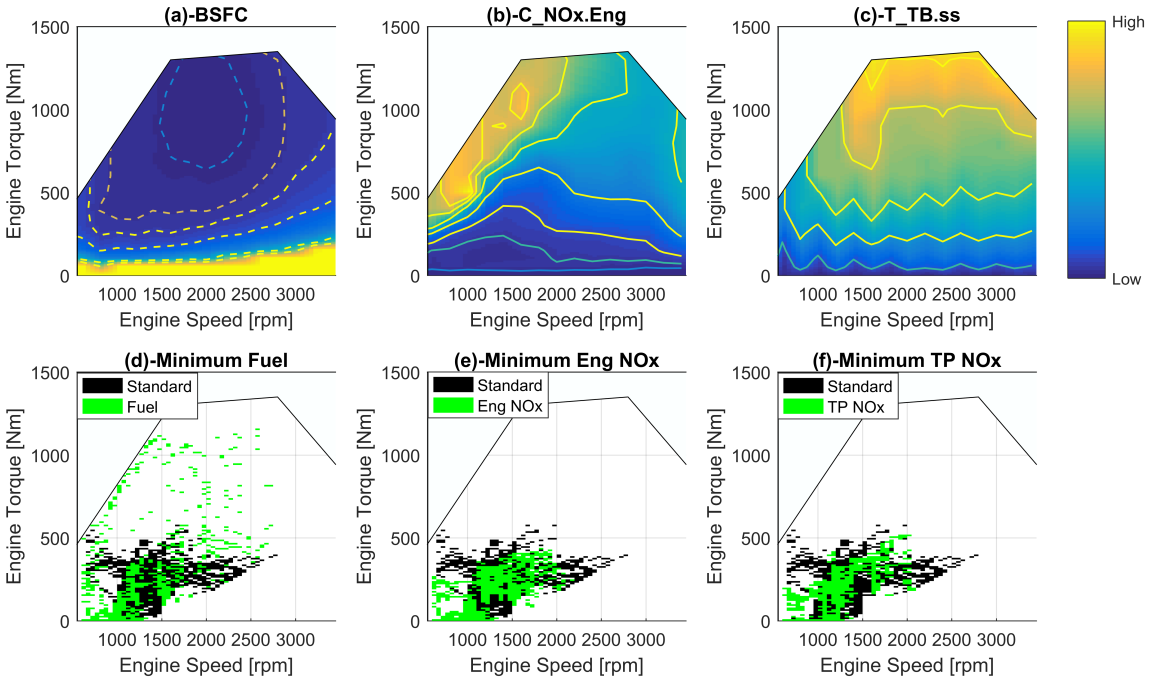

Figure 3.3: Engine maps for brake-specific fuel consumption (BSFC), $C_{\text{NOx.Eng}}$, $T_{\text{TB.ss}}$, and visitation points from different optimization scenarios compared with the standard FTP drive cycle

be between the fuel and the tailpipe emission minimized scenarios (Table 3.2). Therefore, the two former objective functions can be used to compromise between fuel and tailpipe emissions. Especially, the raw emissions minimization scenario is recommended since it improves fuel economy while maintaining tailpipe emission level close to the baseline speed profile.

3.4 Summary

In this chapter, vehicle speed trajectory optimization scenarios are tested to minimize four objective functions, namely acceleration, fuel consumption, engine NOx emissions, and tailpipe NOx emissions. A model is developed for a medium duty diesel truck to calculate fuel consumption and NOx emissions. The vehicle follows a leader which is driven based on the standard FTP drive cycle. Then, dynamic programming is applied to calculate optimal velocity trajectory for the following vehicle during the stabilized (warmed-up) phase of the FTP.

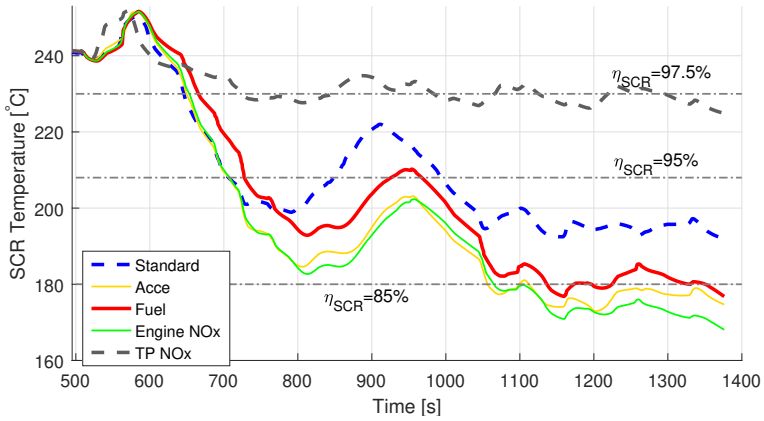

Figure 3.4: SCR temperature for the various optimization objectives

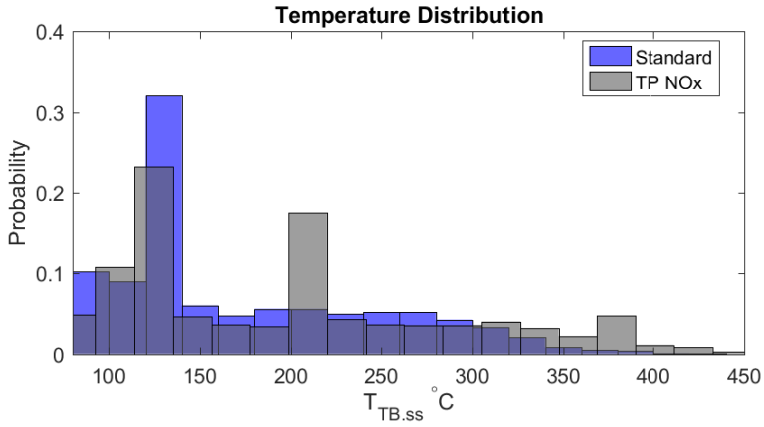

Figure 3.5: $T_{\text{TB.ss}}$ probability distribution comparison between tailpipe NOx optimization scenario and the standard FTP drive cycle

Results show when only the fuel economy is optimized, the tailpipe NOx emissions are doubled (compared to a non-optimized baseline) due to low aftertreatment efficiency and high engine emissions. When the optimization target is changed to the tailpipe emissions, however, 17% of the fuel efficiency is sacrificed to keep the aftertreatment efficiency high, which lowers down tailpipe NOx emissions by 59%. Therefore, it is concluded that maximum fuel saving from an autonomous driving cannot be achieved at the same time as the maximum emission reduction is reached. Finally, it is observed that minimizing the engine out emissions would not reduce tailpipe emissions and one should include the aftertreatment system thermal dynamics in the optimization problem.

Since none of the single objective optimization considered in this chapter achieves concurrent

reduction in fuel consumption and tailpipe NOx, this observation also motivates us to consider a multi-objective function and include both fuel and emissions performance in the objective function to find a set of pareto optimal solutions. Ideally, we are looking for points on the pareto curve that reduce both the total amount of fuel and emissions. Moreover, it is assumed in this chapter that the whole drive cycle of the leader vehicle is available to the follower to perform offline optimization. The next step is to solve the optimization problem using a causal methodology to react to real-time changes in the traffic conditions.

CHAPTER 4

Online Optimal Speed Planner with Accurate Preview

In the previous chapter, we have seen a clear fuel economy-NOx emissions trade-off and as well as the importance of the aftertreatment system in optimal vehicle-following scenarios. But the assumption that accurate information of the whole cycle of the leader vehicle is available to the ego follower makes the solution non-causal and cannot be used in real-world driving scenarios.

A commonly used method for causal trajectory optimization is through model predictive control (MPC). Model predictive control is usually used to control a process when the system needs to satisfy a set of constraints, which is a suitable for the considered problem when traffic constraints and system feasibility constraints of the vehicle should be enforced when optimizing the speed trajectory of the ego follower. In literature, MPC has been used for speed planning to achieve eco-driving of connected and automated vehicles and usually targets at reducing total fuel consumption [70, 36, 6, 39, 76, 61, 53] and sometimes also engine NOx emissions [73]. [73] consider engine feedgas emissions performance for a conventional diesel engine while optimizing the velocity trace during eco-driving, and show that a trade-off among cycle time, emissions and fuel consumption should be addressed carefully to avoid excess NOx emissions. When following a fixed drive cycle, existing literature use variable geometry turbocharger (VGT), exhaust gas recirculation (EGR) techniques as well as airpath controllers to improve fuel efficiency and reduce feedgas emissions for diesel engines [30, 55, 56, 29, 72] via modifying the engine control strategy. As the system is highly nonlinear and constrained, again these papers use model predictive controllers to handle

the high-level objectives and constraints, e.g., minimizing brake-specific fuel consumption (BSFC) [30, 29, 87], pumping loss [56, 72], tracking EGR rate target and fueling rate [55, 72] under instantaneous emissions constraints [30, 29], engine safety constraints [55] or average emissions limits [72]. For vehicles with emissions aftertreatment systems, researchers have also studied control strategies to achieve near-optimal tailpipe emissions with lowest cost through aftertreatment operations [17], without changing the driving behavior at vehicle level. None of the existing literature considers the problem at vehicle level by modifying the driving behavior.

Motivated by the observation in the previous chapter, we propose to tackle the fuel consumption and emissions minimization problem by modifying the vehicle behaviors. The vehicle following problem is formulated as an online fuel and tailpipe emissions co-optimization problem, and the optimal following velocity trajectory is solved using MPC.

Due to the relatively large heat capacity of the turbine, the DOC and the SCR, the thermal dynamics of the aftertreatment system is very slow and subject to highly varying delays [50]. The varying and long delay that exists in the aftertreatment system increases the difficulty to perform real-time optimization directly on the aftertreatment thermal dynamics. To solve this problem, a surrogate cost function is proposed in this chapter, leading to an energy and emissions conscious, MPC-based, vehicle-following algorithm named E^2C-MPC. Simulation is performed to show the effectiveness of the proposed algorithm, instead of including the full aftertreatment system and the tailpipe emissions directly in the objective function. The E^2C-MPC algorithm is the main contribution of this chapter.

The content of this chapter has been presented in [38],

- Huang, C., Salehi, R., Ersal, T. and Stefanopoulou, A.G., 2020. An energy and emission conscious adaptive cruise controller for a connected automated diesel truck. Vehicle System Dynamics, 58(5), pp.805-825.

4.1 General Architecture for Optimal Vehicle Speed Planning

The predictive controller solves the following optimal control problem (OCP) to acquire the optimal input at each time step t:

$$\min_{U} \quad \mathbf{J}(t) = \sum_{k=0}^{N_\mathrm{P}-1} J(k|t) \tag{4.1}$$

where N_P is the number of samples in the prediction horizon, $\mathbf{J}$ is the optimization objective function, with several possible selections presented in later sections, and the optimization variable $U = \begin{bmatrix} a_{\text{veh}}(0|t) & a_{\text{veh}}(1|t) & \cdots & a_{\text{veh}}((N_\mathrm{P}-1)|t) \end{bmatrix}^T$, is the evenly sampled vehicle acceleration over the prediction horizon, with a constant sampling time dt. Thus the prediction horizon is equal to $N_\mathrm{P} \cdot dt$. The notation $z(k|t)$ (here z is used to represent a generic variable) refers to the predicted value of the variable z at the k^{th} step in the prediction horizon, which is the predicted value at time $(t + k \cdot dt)$ given the information at time t.

The OCP is solved under the following constraints $\forall k = 0, 1, \ldots N_\mathrm{p} - 1$:

$$\begin{aligned} \underline{p}(v_\mathrm{l}(k \cdot dt + t + 1)) \leq & p_{\text{veh}}(k+1|t) \leq \overline{p}(v_\mathrm{l}(k \cdot dt + t + 1)) \\ \underline{v_\mathrm{f}} \leq & v_{\text{veh}}(k+1|t) \leq \overline{v_\mathrm{f}} \\ \underline{a_{\text{veh}}} \leq & a_{\text{veh}}(k|t) \leq \overline{a_{\text{veh}}} \\ & x(k+1|t) = x(k|t) + dt \cdot f(x(k|t), u(k|t)), \end{aligned} \tag{4.2}$$

where $v_\mathrm{l}(k \cdot dt + t + 1)$ is the future speeds of the leader at time $(k \cdot dt + t + 1)$, which is used to generate constraints in the OCP. The above four constraints are:

- upper and lower limits of the follower vehicle position ($\overline{p}$, $\underline{p}$) for keeping a positive inter-vehicular distance and avoiding cut-ins from other lanes, constructed using the leader vehicle's position p_l and speed v_l:

$$\overline{p} = p_\mathrm{l} - 0.3 v_\mathrm{l} \tag{4.3}$$

$$\underline{p}(s) = \begin{cases} p_{\text{l}} - (4v_{\text{l}} + 3), & \text{if } v_{\text{l}} > 9 \\ p_{\text{l}} - (10v_{\text{l}} + 3), & \text{if } 0.7 < v_{\text{l}} \leq 9 \\ p_{\text{l}} - 10, & \text{if } v_{\text{l}} \leq 0.7 \end{cases} . \tag{4.4}$$

This formulation is the same as in [70], except that the distance gap is enlarged by changing the values for the multipliers in (4.4) and (4.3), as well as adding the constant offset in (4.4). These numbers are design parameters and can be adjusted by the user based on the traffic condition and controller performance. Enlarging the distance gap will provide more flexibility in varying the speed and thus will deliver better performance, but traffic capacity will drop [48]. Note that the Heaviside step function can be utilized to formulate the expression for (4.4). The parameters in (4.4) and (4.3) are design parameters and can be changed by the user.

- upper and lower limits of the follower speed, with the upper limit $\overline{v_{\text{f}}}$ set to be the road speed limit, and the lower limit $\underline{v_{\text{f}}}$ set to be 0 to enforce a non-negative speed.

- upper and lower limits of the follower acceleration, with $\underline{a_{\text{veh}}} = -6$ m/s^2 and $\overline{a_{\text{veh}}} = 6$ m/s^2. The limits are chosen to be twice that of the maximum vehicle acceleration/deceleration driving the FTP drive cycle.

- system dynamics, which is explained in detail in Sections 4.2 and 4.3.

Through selection of different cost functions, the vehicle speed trajectory can be calculated to optimize a required criterion. For instance, one can select to minimize a_{veh} as done in [57, 70] if an energy conscious optimization is of interest. The selection of the cost function impacts the outcome of velocity trajectory and its critical performance parameters, namely, tailpipe NOx and fuel economy. In the following sections, these performance parameters are simulated with the vehicle model presented in Chapter 2.

Table 4.1: Cost functions defined for both EC-MPC optimization scenarios

i	Case name	Objective to minimize	Cost function
1	EC-MPC$_{\text{f}}$	Fuel	$J_1(k\|t) = \dot{m}_{\text{Fuel}}(k\|t)dt$
2	EC-MPC$_{\text{a}}$	Acceleration	$J_2(k\|t) = a_{\text{veh}}(k\|t)^2$

4.2 Conventional Energy Conscious Model Predictive Controller (EC-MPC)

4.2.1 EC-MPC Control Strategy

With fuel consumption as the optimization objective, the OCP in (4.1) can be solved with different energy conscious cost functions to calculate the optimal speed trajectory of the ego follower. For instance, the vehicle acceleration is used in [57, 70] as a variable correlated with fuel consumption, and in [32, 76, 73] the fuel consumption model is used for optimal speed planning. In this chapter, two cases are studied as benchmarks, where in each of them a cost function from Table 4.1 is used for optimal fuel speed planning calculated using the predictive controller in (4.1). Therefore, the cost at every step t

$$\mathbf{J}_i(t) = \sum_{k=0}^{N_{\text{P}}-1} J_i(k|t), \quad i = \{1, 2\}, \tag{4.5}$$

is used in (4.1) over a horizon of N_{P} steps. The problem in (4.1)-(4.5) is solved numerically using the optimization command fmincon in Matlab with the sequential quadratic programming algorithm. The sampling time dt is set to 0.1 s and then the length of prediction horizon is $(0.1N_{\text{P}})$ s.

4.2.2 EC-MPC Performance Evaluated over FTP Drive Cycle

Vehicle fuel consumption and NOx emissions simulated using the vehicle model in (2.2)-(2.15) with the optimal acceleration from the two EC-MPC controllers are shown in Fig. 4.1 and 4.2 for different prediction horizons. For the lead vehicle, the federal test procedure for light duty vehicles is selected as the desired speed trajectory. Also, the plotted accumulative mass of fuel and tailpipe NOx are normalized with the corresponding values when the vehicle is driven with the nominal

FTP speed trajectory. In other words, we are comparing the scenario when the follower vehicle is driving the optimized trajectory with the nominal case when the follower vehicle is driving the leader's drive cycle exactly without any speed planning. The plots in Fig. 4.1 indicate that both EC-MPC$_f$ and EC-MPC$_a$ can effectively reduce fuel consumption, but at the same time, both of the controllers increase tailpipe NOx emissions compared with the nominal trajectory due to the drop in SCR efficiency despite that engine emitted NOx is reduced in most cases (Fig. 4.2). It is also shown that although EC-MPC$_f$ performs better in reducing fuel consumption, it generates more engine and tailpipe NOx emissions compared with EC-MPC$_a$.

With longer prediction horizon in EC-MPC controllers, acceleration level is reduced and, at the same time, cycle-averaged turbine temperature and SCR efficiency are also reduced as shown in Fig. 4.2. Due to the lower SCR efficiency, the resulting tailpipe NOx (in Fig. 4.1) does not drop even though the trip acceleration level is reduced.

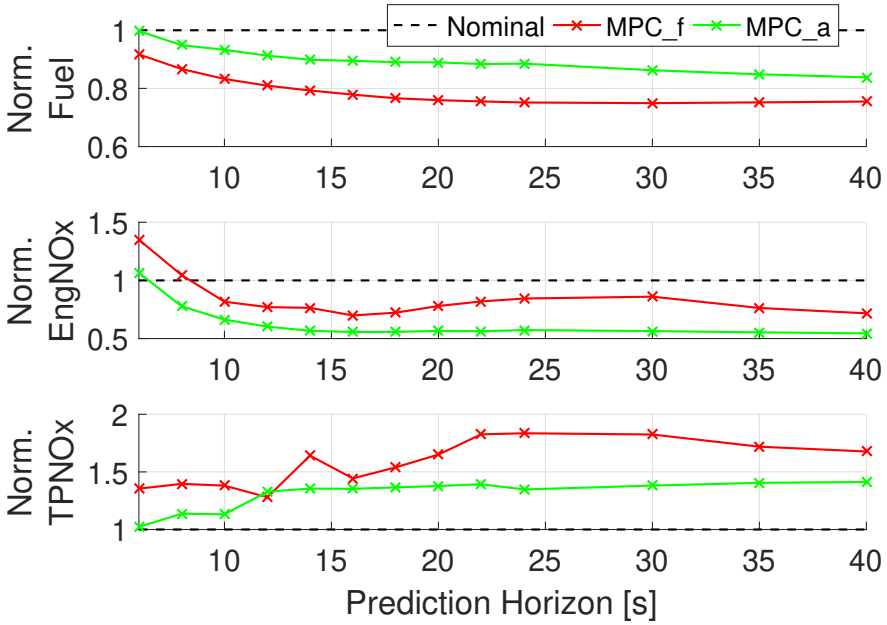

Figure 4.1: Normalized comparison of the optimal solutions of EC-MPC controllers with different prediction horizons. Fuel consumption, engine out and tailpipe emissions performances are shown in subplots from top to bottom, respectively.

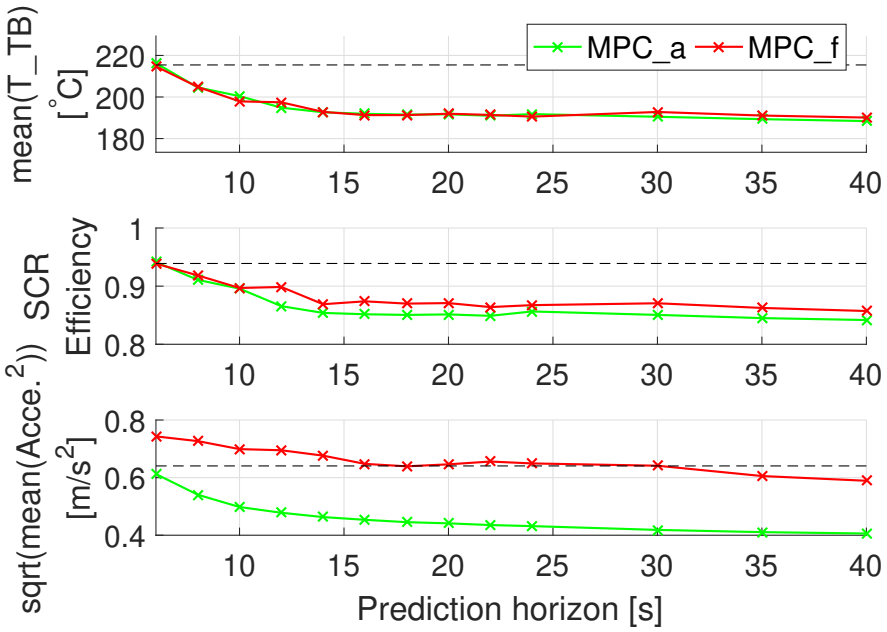

Figure 4.2: Correlation between cycle-averaged turbine temperature $\overline{T_{\text{TB}}}$, SCR efficiency and vehicle acceleration $\overline{|a|}$, of the optimal trajectories when follower vehicle is using the EC-MPC controllers. Lower acceleration level yields lower turbine temperature and lower SCR efficiency.

4.3 Energy and Emissions Conscious Model Predictive Controller (E^{2}C-MPC)

The conventional ego speed controllers described in the previous section indicate degraded tailpipe emissions performance despite better fuel economy when the formulation is only energy conscious and emissions are ignored. To avoid this problem, an intuitive solution would be to add an additional constraint to the OCP to limit the follower vehicle's total tailpipe NOx emissions:

$$\sum_{k=0}^{N_{\text{total}}} \{\dot{m}_{\text{NOx.TP}}(k)\}_{\text{MPC}} \cdot dt \leq \sum_{k=0}^{N_{\text{total}}} \{\dot{m}_{\text{NOx.TP}}(k)\}_{\text{Nom}} \cdot dt, \tag{4.6}$$

where the subscript "MPC" refers to the driving scenario in which the follower vehicle drives the optimized trajectory, and "Nom" refers to the nominal driving scenario in which the ego follower drives the leader vehicle's drive cycle exactly. This way, the emissions performance could be included in the control loop. Dynamic programming method could be used to solve the OCP with the

additional constraint (4.6) by considering the accumulative NOx as an additional state. However, this solution strategy would be non-causal, since it requires knowledge of the whole drive cycle before starting to solve for the optimal solution. Furthermore, it would be very computationally costly. Thus, optimization problems with this terminal constraint are hard to solve using causal control strategies due to the fact that the summation is calculated over the whole trip. Hence, an alternative strategy is developed in this section that is practically implementable.

4.3.1 E^{2}C-MPC Design and Approximations

The emissions constraint in (4.6) is relaxed to be a soft constraint and embedded into the cost function by adding an additional term to the previous EC-MPC cost function defined in (4.5), which is the instantaneous emissions scaled by an equivalence factor. This forms the energy and emissions conscious cost:

$$\mathbf{J}_{\mathrm{E^2C\_NOx}}(t) = \sum_{k=0}^{N_\mathrm{P}-1} \big(\dot{m}_{\mathrm{fuel}}(k|t) + w \cdot \dot{m}_{\mathrm{NOx.TP}}(k|t)\big)dt. \tag{4.7}$$

With the cost function defined in (4.7), the OCP aims to reduce the predicted tailpipe NOx emissions in the prediction horizon in addition to reducing the predicted fuel consumption.

Note that the equivalence factor w should be pre-tuned offline. A method is proposed in [93] to calculate the equivalence factor online by calculating an approximation of the optimal cost-to-go function. This method, however, needs finding the dynamic programming solution with high computational burden and with a knowledge of the whole drive cycle. Therefore, an alternative approach is adopted in this chapter; namely, we focus on designing the energy and emissions conscious MPC, and identify a range for w that works for most of the well known drive cycles.

The OCP satisfies the same constraint as in (4.2) with the system dynamics $f(x, u)$ for the state vector $x = \Big[p_{\mathrm{veh}}, v_{\mathrm{veh}}, T_{\mathrm{b.rSCR}}\Big]^T$, and $T_{\mathrm{b.rSCR}}$ is the state for SCR brick temperature simulated with the reduced-order model presented in Section 2.3.2, where the aftertreatment system including SCR is assumed to be lumped into one thermal mass. The vehicle longitudinal dynamics and the

powertrain model from (2.1)-(2.7) remain the same. Note that this reduced SCR model is only used in the MPC and the plant is still simulated with the full thermal model; i.e., the full thermal model is used for evaluating the optimal trajectory and update the initial conditions at each MPC run.

Two considerations are worth highlighting here: (1) The results in Fig. 4.2 show that as acceleration increases, fuel consumption increases, but, at the same time, turbine temperature increases as well, which leads to higher SCR temperature and SCR efficiency, and consequently, lower tailpipe NOx. (2) Since the prediction horizon will be limited, we would expect an MPC with a faster dynamics to perform more consistently than that with slower dynamics. From the above observations, increase in turbine temperature could potentially be used as an indication of reduced tailpipe NOx emissions with MPC_a.

Based on these considerations, a second E^2C-MPC formulation is developed as follows in an effort to seek a simpler OCP. In particular, a new cost function $\mathbf{J}_{\text{E}^2\text{C\_TB}}(t)$ is introduced, which is obtained by replacing the $\dot{m}_{\text{fuel}}$ term in (4.7) with acceleration, and replacing the $m_{\text{NOx.TP}}(k|t)$ term with turbine temperature as follows.

$$\begin{aligned}\mathbf{J}_{\text{E}^2\text{C\_TB}}(t) &= \sum_{k=0}^{N_\text{P}-1} \Big(a(k|t)^2 + w(T_{\text{TB}}(k|t) - T_{\text{thr}})^2 \cdot I_{\text{TB}}(k) \Big), \quad \text{with} \\ I_{\text{TB}}(k) &= \begin{cases} 1, & \text{if } T_{\text{TB}}(k|t) < T_{\text{thr}} \\ 0, & \text{if } T_{\text{TB}}(k|t) \geq T_{\text{thr}} \end{cases},\end{aligned} \tag{4.8}$$

where T_{thr} is a pre-tuned parameter, which represents the lower desired threshold for the turbine temperature. The OCP satisfies the same constraint as in (4.2) with the system dynamics $f(x,u)$ for the state vector $x = \begin{bmatrix} p_{\text{veh}}, v_{\text{veh}}, T_{\text{TB}} \end{bmatrix}^T$ including (2.1)-(2.8). Thus, this formulation, called $\text{E}^2\text{C-MPC}_{\text{TB}}$, aims to reduce acceleration while maintaining turbine temperature. As shown in the next section, this formulation is able to balance fuel consumption and NOx emissions, and it can do so with simpler dynamics that makes solving the OCP numerically easier.

4.3.2 E^{2}C-MPC Performance Evaluation over FTP Drive Cycle

4.3.2.1 Selection of E^{2}C-MPC Optimization Criterion

The two E^{2}C-MPC controllers are evaluated over the FTP drive cycle with different length of prediction horizons with results shown in Fig. 4.3. The sampling time dt is increased to 1 s compared with 0.1 s as used in Section 4.3 to shorten the computation time. For each selected horizon, the equivalence factor w is swept from 0 to 1 to show the trade-off between emissions and fuel consumption. In other words, the multi-objective optimization problem is scalarized to build the Pareto-optimal curve. In each plot, the accumulative fuel and tailpipe NOx values are normalized by their respective nominal values.

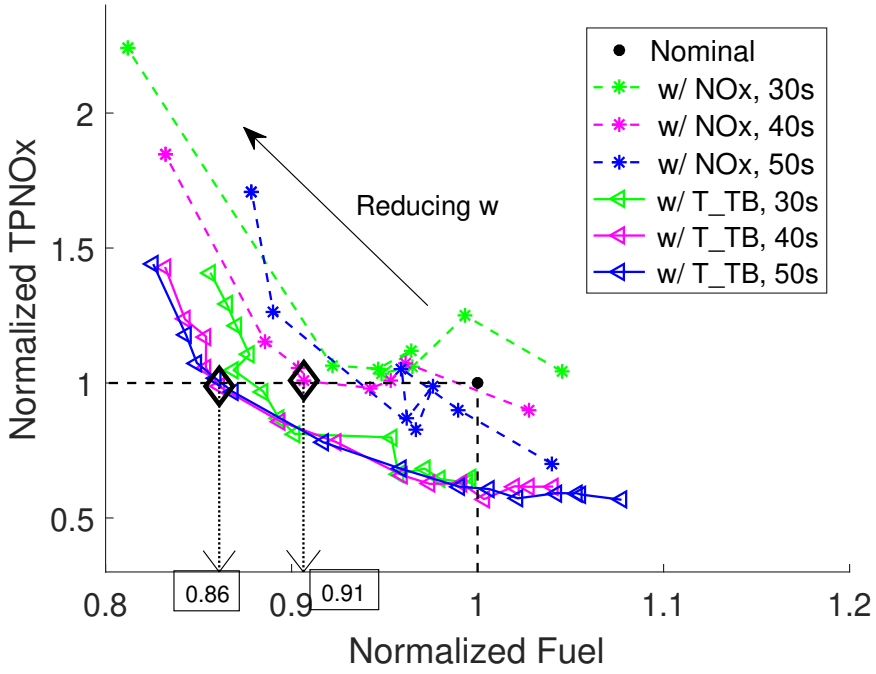

Figure 4.3: Fuel and emissions reduction effects using E^{2}C-MPC$_{\text{NOx}}$ (labeled with NOx), and E^{2}C-MPC$_{\text{TB}}$ (labeled with T_TB). Different data points on a same curve are due to monotonically varying w.

End of drive cycle results shown in Fig. 4.3 indicate E^{2}C-MPC$_{\text{TB}}$ outperforms E^{2}C-MPC$_{\text{NOx}}$ since (1) the emission-fuel consumption curve is smoother and more monotonic in both fuel and emissions performance, and (2) better fuel economy is obtained at the same level of NOx emis-

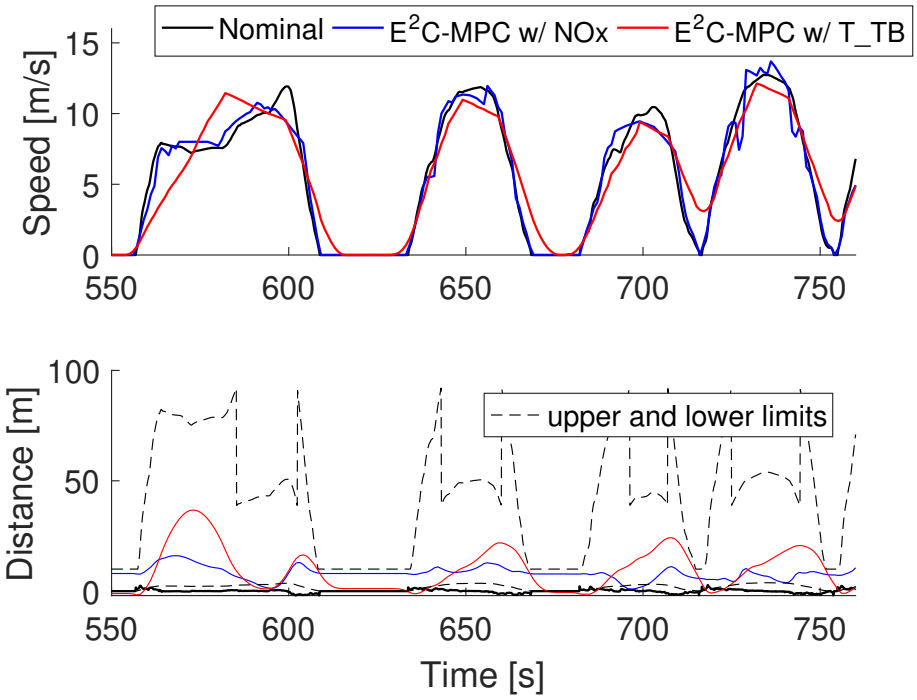

Figure 4.4: Optimal trajectories using $E^2C\text{-}MPC_{NOx}$ and $E^2C\text{-}MPC_{TB}$ with 40s prediction horizon. The two optimized trajectories (correspond to the diamond marked points on the left figure) are chosen such that they have the same tailpipe NOx emissions as the nominal FTP trace.

sions. One reason for $E^2C\text{-}MPC_{TB}$ being more effective than $E^2C\text{-}MPC_{NOx}$ is that the objective function $\mathbf{J}_{E^2C\_TB}(t)$ is numerically easier to optimize. The turbine thermal dynamics and the quadratic acceleration terms are less complicated, and have a larger gradient due to faster dynamics than that of the reduced SCR thermal dynamics and the fuel consumption terms. The smooth and predictable NOx and fuel consumption trade-off observed for $E^2C\text{-}MPC_{TB}$ offers convenience for calibrating the equivalence factor w for achieving the best fuel economy for a given tailpipe emissions.

Figure 4.4 shows the optimal speed traces and the distance between the two vehicles for the two optimization formulations, $E^2C\text{-}MPC_{TB}$ and $E^2C\text{-}MPC_{NOx}$, both with a 40 s prediction horizon. The selected points are marked with diamond markers in Fig. 4.3, and their equivalence factors are selected such that both MPC controllers generate the same tailpipe NOx emissions as the nominal FTP trace. However, $E^2C\text{-}MPC_{TB}$ with 40 s horizon results in 14% better fuel economy, while

$E^2C\text{-}MPC_{NOx}$ improves the fuel economy by 9% compared to the nominal. This behavior is related to the fact that, as the distance trajectories in Fig. 4.4 show, with the $E^2C\text{-}MPC_{TB}$ utilized for the optimal speed planning, the advantage of having a flexible following distance is exploited more compared to the $E^2C\text{-}MPC_{NOx}$, in which the vehicle distance is almost constant. One reason for this performance difference is that with the more complicated reduced SCR thermal and emissions models involved in the $E^2C\text{-}MPC_{NOx}$, it is easier for the optimizer to get stuck at infeasible regions (7% of cases, as shown in Table 4.2) or not being able to satisfy the first-order optimality conditions before design step size tolerance is reached (87% of cases) compared to $E^2C\text{-}MPC_{TB}$ (0% and 1% of cases, respectively). With $E^2C\text{-}MPC_{TB}$, the chance of finding the point satisfying the first-order optimality conditions is much higher (99% of cases). Note that if the design step size tolerance is reached before the first-order optimality conditions are met, that means the current point satisfies the constraints and is possibly close to a local optimum, but the violation of the first-order optimality conditions is larger than that required by the optimality tolerance and reducing this violation would require a smaller design step size than the allowed minimum threshold. Also note that the formulation with NOx is using minimum step size as 0.001 m/s^2, while with TB the minimum step size is 0.01 m/s^2, 10 times of that for the NOx formulation. This means that the formulation with NOx has a more sensitive cost function, which explains the more consistent and better performance of $E^2C\text{-}MPC_{TB}$ in Fig. 4.3.

Exit reason	Not feasible	Reaches maximum number of iterations	First-order optimal	Design step size tolerance reached
w/NOx	7%	2%	4%	87%
w/T_{TB}	0%	0%	99%	1%

Table 4.2: Reasons for terminating optimization process when solving for optimal trajectories using $E^2C\text{-}MPC_{NOx}$ and using $E^2C\text{-}MPC_{TB}$ (trajectories are associated with Fig. 4.4), when the optimal control problem is solved with optimization command fmincon in Matlab.

The computation time required for calculating the optimal speed over the prediction horizon at each step with $E^2C\text{-}MPC_{TB}$ is expected to be reduced significantly due to simplified dynamics when it is compared with $E^2C\text{-}MPC_{NOx}$. Table 4.3 shows the statistical features of computation

MPC Type	w/ NOx				w/ T_{TB}			
Horizon [s]	20	30	40	50	20	30	40	50
Mean [s]	0.62	1.65	3.27	5.39	0.02	0.03	0.05	0.08
Std [s]	0.35	0.75	1.23	1.82	0.01	0.02	0.03	0.07
Max [s]	1.82	4.98	8.18	11.82	0.14	0.28	0.28	0.63

Table 4.3: Comparison of statistics calculated from computation time of all optimization steps for E^2C-MPC$_{\text{NOx}}$ and for E^2C-MPC$_{\text{TB}}$.

time for the two OCPs calculated with time step of 1 s. The simulations results are obtained on a desktop computer with an Intel Core i7-7700 CPU at 3.6GHz. The code is written and executed in the Matlab environment with the purpose of comparing the computation time of these two OCPs. It is expected that less computation time can be achieved by re-writing and optimizing the code in a compiled language if run on the same hardware. As shown, with the same prediction horizon, the E^2C-MPC$_{\text{TB}}$ with T_{TB} dynamics runs almost 10 times faster than the E^2C-MPC$_{\text{NOx}}$ where SCR and NOx models with reduced order thermal dynamics for the aftertreatment system are used.

4.3.2.2 Selection of Prediction Horizon

The length of the prediction horizon is a design parameter for MPC. Thus, its impact on the E^2C-MPC$_{\text{TB}}$ controller is studied and shown in Fig. 4.5 for prediction horizons from 10 s to 70 s. As shown, when the prediction horizon increases from 10 s to 40 s, the normalized Fuel - NOx curve moves towards the left-lower direction, which means less fuel consumption and tailpipe NOx emissions. However, as also shown, increasing the prediction horizon beyond 40 s does not help in saving more fuel or tailpipe NOx, but increases the computational load due to the increased number of optimization variables. Thus, it is concluded that E^2C-MPC$_{\text{TB}}$ with a 40 s prediction horizon is an acceptable design to reduce fuel consumption while maintaining emissions performance of the ego follower.

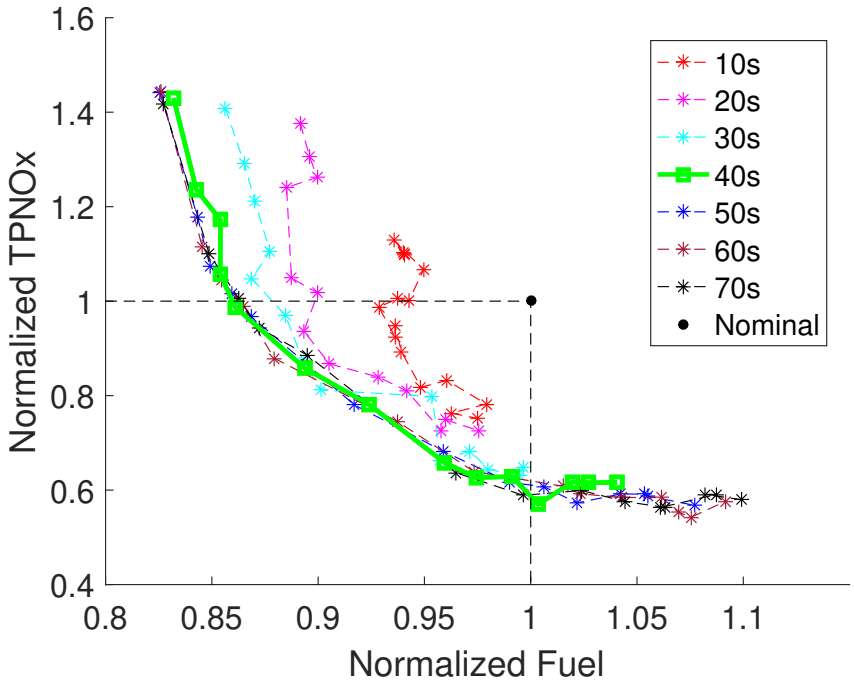

Figure 4.5: Normalized fuel consumption vs. TPNOx for optimal trajectories with E^{2}C-MPC$_{\text{TB}}$ evaluated over FTP with different selections of w and prediction horizon N_{P}.

4.3.2.3 Effect of the Equivalence Factor w

Optimized ego speed, acceleration trajectories, and histogram of acceleration for two equivalence factors, both with a 40 s prediction horizon, are shown in Fig. 4.6 and 4.7. With larger w, the controller penalizes the acceleration relatively less, and thus results in trajectories with larger accelerations. This is seen more clearly in Fig. 4.7, since the acceleration distribution for smaller w is located mostly in the range of $[-1, 1]$ m/s^2, while for larger w, this range grows into $[-1.5, 1.5]$ m/s^2. On the one hand, the resulting average turbine temperature grows with w as shown in Fig. 4.8(b) as well as the time resolved plot Fig. 4.9(a), as there is higher cost for dropping turbine temperature for larger ws. On the other hand, since the relative penalty on a large acceleration is decreased, a more oscillatory trajectory ensues with larger w and that leads to higher fuel consumption as shown in Fig. 4.8(a). As the result of higher turbine temperature, SCR temperature is also increased as shown in Fig. 4.9(b), which avoids the large SCR temperature drop to around 160°C as happens with $w = 0$ and could maintain the SCR temperature to stay above 200°C with larger w

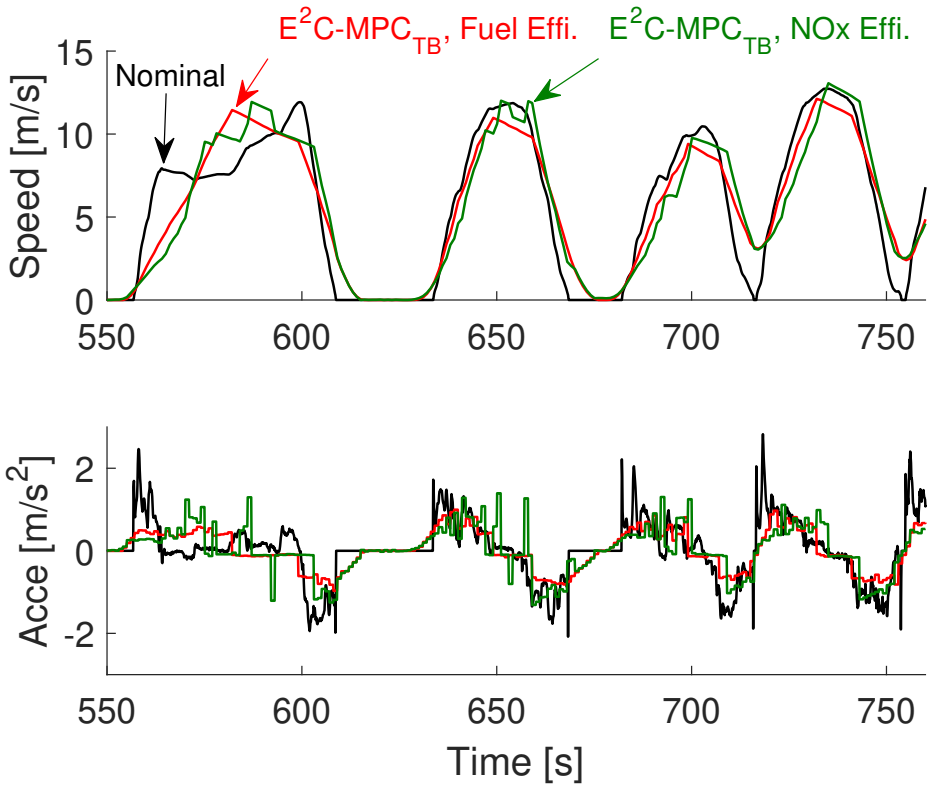

Figure 4.6: Optimized ego speed and acceleration traces using E^{2}C-MPC$_{\text{TB}}$ controllers with two different equivalence factors corresponding to a more fuel-efficient trajectory ($w = 0.1$) and a more NOx-efficient trajectory ($w = 0.6$). The fuel-efficient trajectory has the same tailpipe NOx emissions as the nominal trajectory, and the NOx-efficient trajectory has the same fuel consumption as the nominal trajectory.

(Fig. 4.8(c)). This results in a higher average SCR efficiency, as shown in Fig. 4.8(d). Hence, it is inferred that the reason for why increasing w reduces tailpipe NOx emissions as seen in Fig. 4.8(d) is that average SCR efficiency (which is also the average NOx conversion efficiency) increases with the equivalence factor.

4.3.3 Robustness of E^{2}C-MPC: Performance Evaluation over Different Drive Cycles

The robustness of the proposed E^{2}C-MPC controller with the surrogate cost (i.e., E^{2}C-MPC$_{\text{TB}}$) to variations in the drive cycle is evaluated by testing the controller over five additional drive cycles including Heavy Duty FTP (FTPHD), the Supplemental Federal Test Procedure (SC03), Worldwide

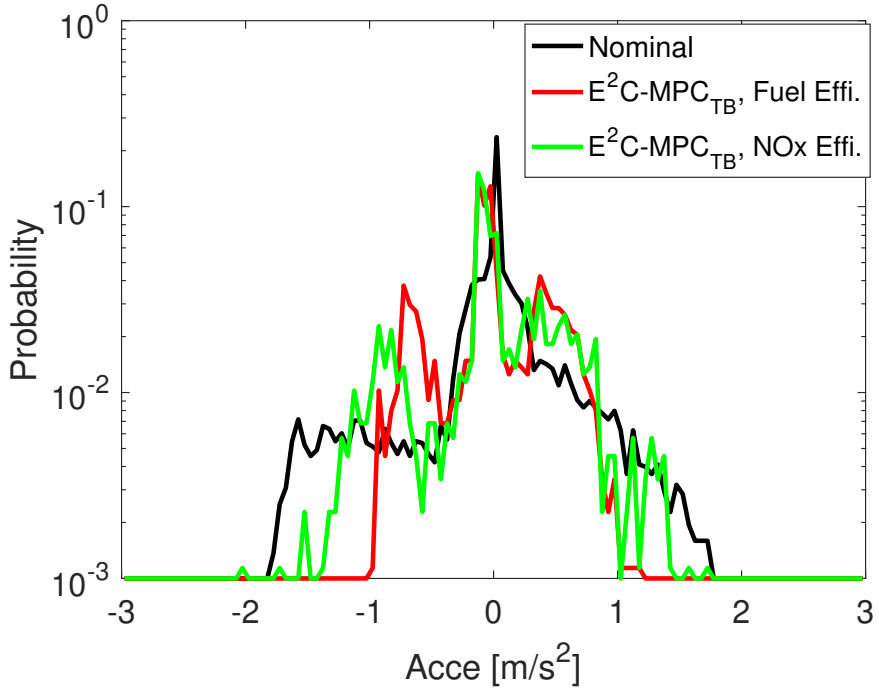

Figure 4.7: Histograms of optimized ego acceleration with the two different equivalence factors chosen as in Fig. 4.6.

Harmonised Light Vehicle Test Procedure (WLTP), World Harmonized Vehicle Cycle (WHVC), and New European Driving Cycle (NEDC). Fig. 4.10 shows the vehicle speed and acceleration visitation points of these six selected drive cycles when the E^{2}C-MPC with 40 s prediction horizon is used to optimize the velocity trajectory. As shown, these six drive cycles span a wide range of vehicle operating conditions.

The temperature of the aftertreatment system at the end of the FTP Bag 1 is selected as the initial condition for all the other cycles for consistent evaluation and comparison to the FTP Bag 2 results presented in the previous sections. Similar to the FTP simulations, it is assumed that a leader vehicle is driving one of the five drive cycles mentioned above, and the follower vehicle is using the E^{2}C-MPC$_{\text{TB}}$ controller design to optimize its speed trajectory. The equivalence factor w is swept for each test to generate the normalized Fuel - NOx curves for these trajectories, as shown in Fig. 4.11. The fuel consumption and tailpipe NOx values for different tests are normalized by their respective values corresponding to each test's nominal driving scenario.

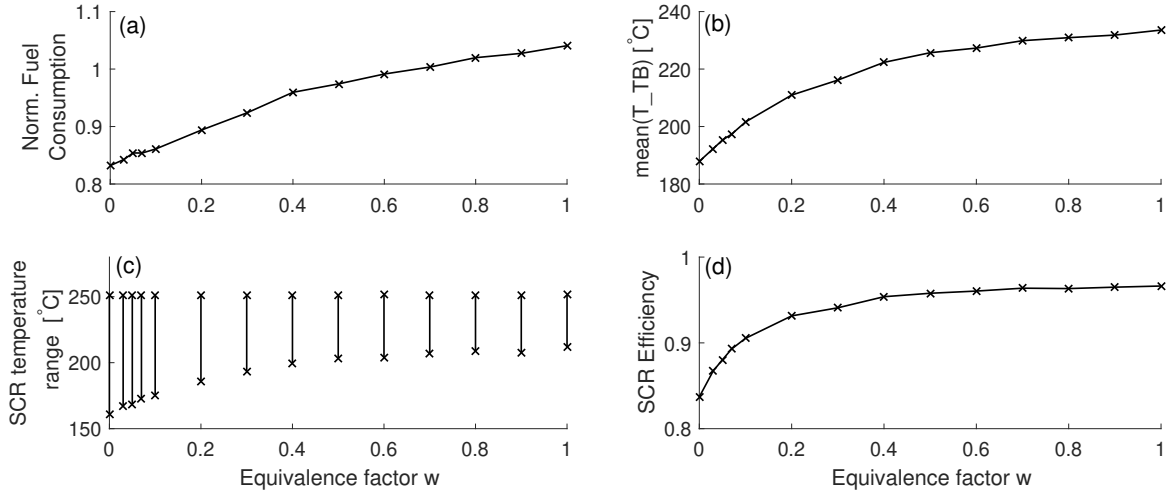

Figure 4.8: Effect of w on normalized fuel consumption, turbine temperature, SCR temperature range (maximum and minimum SCR temperature) and average SCR efficiency when the controller is applied to the FTP drive cycle.

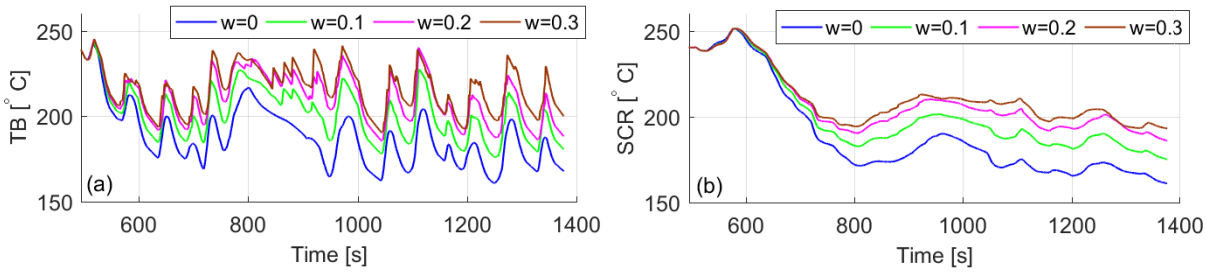

Figure 4.9: Effect of equivalence factor w on turbine temperature and SCR temperature, shown as time resolved results.

For all the tested drive cycles, there exists a range of w such that the optimal trajectories have lower fuel consumption and lower tailpipe NOx emissions than the nominal (Fig. 4.11). To visualize this range, the resulting normalized fuel consumption and tailpipe NOx are separately shown at each w in Fig. 4.12. As observed, the trend is the same for all trajectories; with increasing equivalence factor, fuel consumption increases and tailpipe NOx emissions decrease. The green dashed box in Fig. 4.12 shows the range of the equivalence factor w in the proposed E^{2}C-MPC$_{\text{TB}}$ controller when a selected w is acceptable for all drive cycles; i.e., the E^{2}C-MPC$_{\text{TB}}$ controller with that w will yield an optimal trajectory that is both more fuel-efficient and NOx-efficient than its leader vehicle's drive cycle. Note that a priori knowledge of the drive cycle would allow for im-

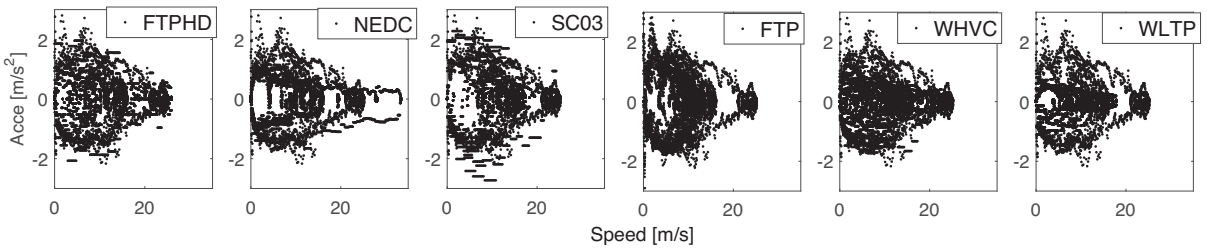

Figure 4.10: Visitation points of the vehicle speed and acceleration for six different drive cycles commonly used for vehicle certification.

proving the selection of w by performing offline computations to make the optimal trajectory more fuel/emissions-efficient. However, if the drive cycle is not known beforehand, choosing the smallest acceptable w will yield a causal controller, which results in 5-15% improvement in the fuel economy with a corresponding 0-25% NOx emissions reduction for these tested cycles. Fig. 4.12 also shows that with $w = 0$, the E^{2}C-MPC$_{\text{TB}}$ controller simplifies into the conventional EC-MPC$_{\text{a}}$ and optimized traces for 5 of the 6 tested drive cycles result in more tailpipe NOx emissions than their corresponding leading cycles. This observation confirms that the E^{2}C-MPC$_{\text{TB}}$ controller has better performance in maintaining low emissions than the EC-MPC$_{\text{a}}$ controller.

4.4 Summary

This chapter contributes a noval model predictive control formulation, namely E^{2}C-MPC, to balance fuel consumption and tailpipe NOx emissions in vehicle-following scenarios for diesel vehicles that are equipped with SCR-exhaust aftertreatment systems, by planning an optimal speed trajectory based on predictive information of leader drive cycle and a flexible following distance between the two vehicles. Simulation results with a validated medium duty diesel truck model confirm that the new formulation can achieve 5-15% improvement in the fuel economy with a corresponding 0-25% NOx emissions reduction in all the drive cycles tested including FTP, NEDC, WHVC etc. The new formulation's design parameters, namely, the prediction horizon and the equivalence factor, are studied to understand their impact on the controller's performance, and it is found that a good performance can be achieved with the same design parameters across all the

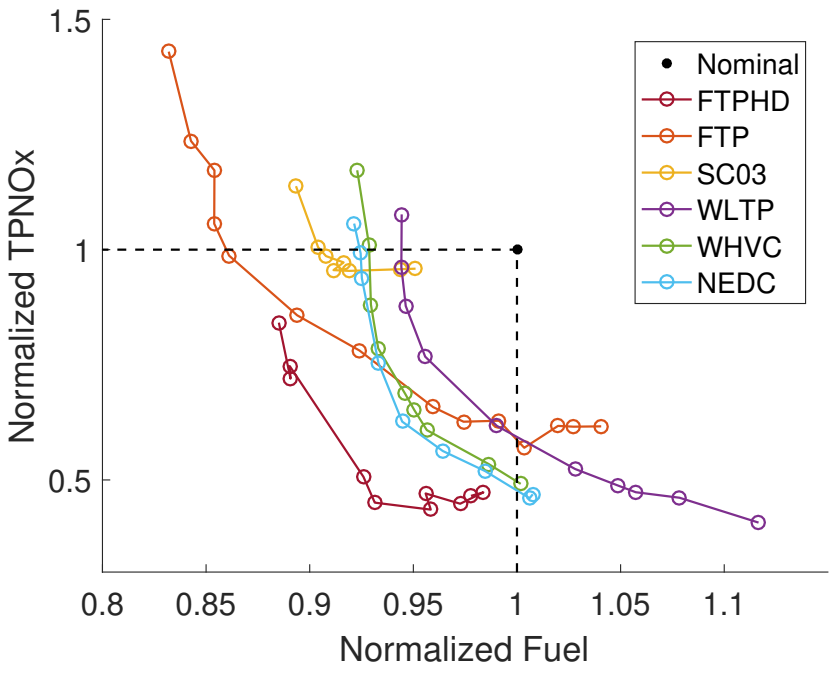

Figure 4.11: Pareto-shaped fronts observed for normalized fuel consumption versus NOx when testing different drive cycles with E^2C-MPC_{TB} controller design.

drive cycles tested, where a good performance means improved fuel economy without a reduction, and in fact often an improvement, in NOx emissions performance.

The analysis of the computational performance of the new controller reveals that an online implementation could be feasible. Hence, the results encourage further development and experimental testing of this controller. Furthermore, it is important to note that the exact numbers for fuel consumption and tailpipe emissions are heavily relied on the accuracy of the engine and aftertreatment model. Unfortunately, "all models are wrong", and in fact, modeling the engine behaviors during transient conditions as well as de-NOx performance of the SCR-aftertreatment system is a very complex matter and there is still ongoing research in order to understand the exact phenomenon occurring inside the system. Coming up with a comprehensive model is not part of the goal of this thesis, so in the next chapter, an experimental validation is performed via hardware-in-the-loop test setup to provide detailed and realistic evaluation of this algorithm.

There are two important challenges for the proposed method so far. First, accurate information

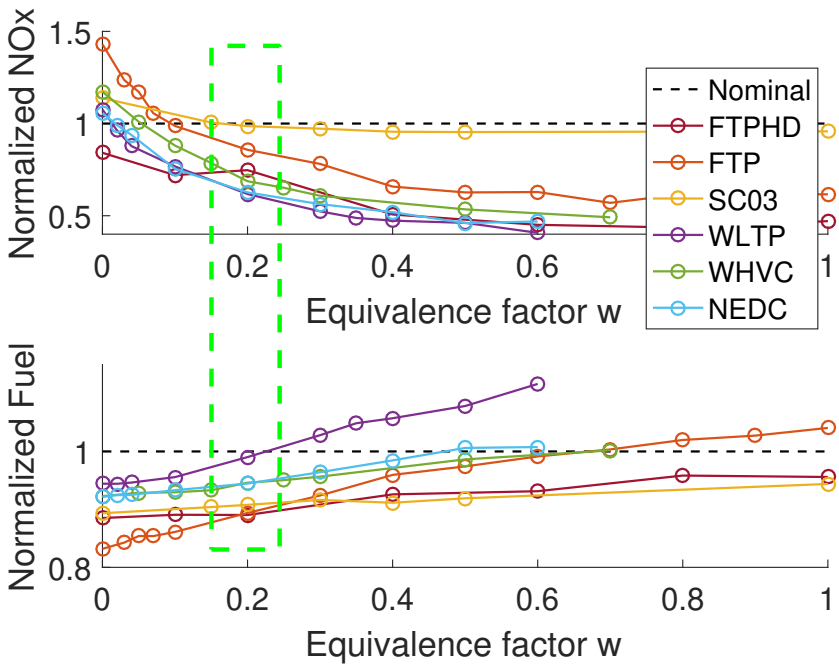

Figure 4.12: Effect of equivalence factor w on normalized fuel consumption and tailpipe NOx emissions of different drive cycles.

of the lead vehicle speed within the future 40 s is required to use the predictive controller for speed planning, and second, there are some traffic rules that are not captured by requiring the controlled vehicle to follow the leader vehicle. In terms of the speed prediction, in practice, speed prediction within the future 40 s is not a trivial task in real driving conditions. In this thesis, we propose a modified formulation to tackle the challenge caused by inaccurate prediction. Analyzing the effect of inaccurate predictions on E^{2}C-MPC performance and developing remedies to minimize the expected deterioration in performance and to honor the designed constraints are crucial for understanding the actual performance of the algorithm if used in real world, and are studied in Chapter 6.

CHAPTER 5

Hardware-In-the-Loop Experiment

As mentioned at the end of the previous chapter, there are some inevitable limitations for predicting the engine feedgas NOx and tailpipe NOx emissions when engine feedgas NOx emissions and SCR de-NOx efficiency are modeled as look-up tables, which will affect the accuracy of the simulation results. An accurate model of the engine NOx emissions especially in transient drive cycles typically requires a full-order physics-based air path model that includes, e.g., the effect from EGR flow rate and intake manifold pressure, and an example can be seen in [20]. In terms of the model for SCR reduction ratio in urea SCR catalyst, de-NOx efficiency depends on exhaust gas composition, exhaust mass flow rate, concentration of the ammonia, and the SCR temperature. This also drives a need for a detailed model for chemical reactions [17, 43, 88, 42, 12, 83]. Moreover, the lumped SCR temperature model introduces errors into the system, and temperature model for SCR catalytic converters with a honeycomb structure of various complexities can be found in [64, 85, 51, 83, 25].

Although it is possible to create more accurate models, this will introduce high simulation complexity and will need huge effort in model identification. Thus in this section, we instead utilize experiments with hardware-in-the-loop to study the performance of the E^2C speed planner as well as the trade-off between fuel consumption and tailpipe emissions in vehicle-following scenarios. A networked, real-time hardware-in-the-loop simulation architecture presented in [21] is extended with a speed planner to test this planning algorithm in a vehicle following scenario, and Fig. 5.1 in this chapter shows a schematic architecture. Model-in-the-loop as well as the hardware-in-the-loop

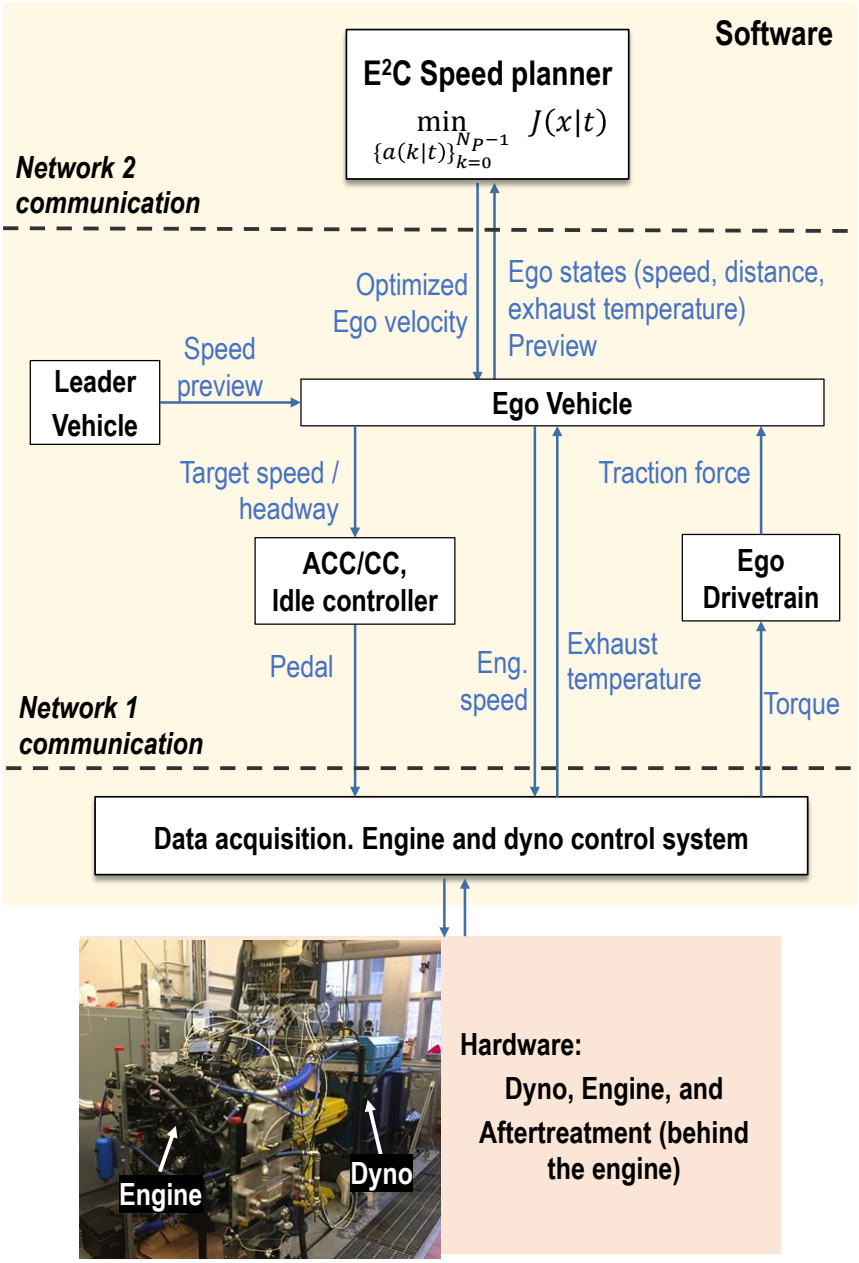

Figure 5.1: A schematic showing the architecture of the hardware-in-the-loop simulation framework.

results of a Ford 6.7L V8 Powerstroke diesel engine and a stock emissions aftertreatment system from a Ford F250 medium-duty truck are provided, allowing detailed and realistic evaluation of fuel economy and tailpipe NOx emissions.

With an emissions-centric calibration, tailpipe NOx emissions is reduced by 18% with 7% more fuel consumption and 10% higher average engine torque level than a standard fuel-centric

calibration. And for all the cases tested, the E^{2}C-MPC controller performs better in both fuel and tailpipe emissions than a simple PI-based ACC controller. Thus, the effectiveness of the E^{2}C-MPC is demonstrated experimentally.

The content of this chapter is included in a paper that is under preparation:

- Huang, C., Salehi, R., Stefanopoulou, A.G., Ersal, T., Hardware-in-the-loop exploration of energy vs. emissions trade-off in eco-following scenarios for connected automated vehicles, under preparation.

5.1 Real-time HIL Experiment Architecture

The ego vehicle considered in this work is a Ford F-250 medium-duty truck. A networked hardware-in-the-loop setup is created by following the principles described in [21, 22]. Three major components involved in the networked experimental setup are (1) the ego vehicle simulation with a physical 6.7-liter diesel engine, a physical SCR-based aftertreatment system, as well as the data acquisition, engine and dynamometer control systems in the loop, (2) the leader vehicle simulation, and (3) the speed planner. The leader vehicle and the speed planning algorithm (either the E^{2}C planner in Chapter 4 or an adaptive cruise controller), as well as the components of the follower vehicle except the engine and aftertreatment system (including idle controller, drivetrain, and the vehicle dynamics) are simulated in Matlab/Simulink. The leader and the ego vehicles are simulated in one Matlab/Simulink instance, and the E^{2}C planner is simulated in another separate Matlab/Simulink instance as an on-demand service, and responds to calls from the ego vehicle model only when needed. A third Matlab/Simulink instance is integrated with AVL EMCON, a real-time engine and dyno control and data acquisition system.

User Datagram Protocol (UDP) is used to achieve communication over the internet between each pair of Matlab/Simulink simulation instances. Two UDP sockets are created to allow communication between the two client-server pairs (Network1 and Network2 in Fig. 5.1). For the first pair (called Network1 in Fig. 5.1), the Matlab/Simulink instance with AVL EMCON integration

Table 5.1: Specifications of the simulated Ford F-250 vehicle.

Parameter	**Value and Unit**
Vehicle mass	4060 kg
Gear ratio	[3.97,2.31,1.51,1.14,0.85,0.67]
Transmissions efficiency	90%
Front area	4.3066 m^2
Air drag coefficient	0.4
Rolling resistance	0.0093
Simulation time step ΔT	0.02 s

acts as the client and the ego vehicle setup acts as the server, where engine and aftertreatment measurements are sent from client to server, and engine and dynamometer control demands are sent from server to client. The ego setup also acts as the client for the second pair (called Network2 in Fig. 5.1), and the Matlab/Simulink instance with E^2C speed planner acts as the server, where the ego states and leader preview information are sent from client to server, and E^2C planner sends the optimized ego velocity trajectory from server to client.

5.1.1 Model of the Ego Vehicle

The vehicle model used in this work is adopted from the modeling framework presented in [21]. The idle controller, drivetrain including torque converter, transmission and gear shift logic, as well as the vehicle dynamics are simulated for the ego vehicle similar to [21]. The gear strategy is simulated such that the target gear level is decided by vehicle speed and acceleration [38], and an off-delay operation exists to avoid chattering behaviors in gear shifting. The transmission loss is modelled with a constant transmission efficiency. The model of the ego vehicle is simulated with a step time $\Delta T = 0.02$ s. The specifications of the modelled vehicle are summarized in Table 5.1.

5.1.2 Driving Modes and Tracking Controllers

Two modes are simulated.

The first mode is E^{2}C speed planning mode [1] (referred to as E^{2}C mode), where the E^{2}C planning algorithm is used as a high-level planner to generate an optimal reference velocity and a low-level PI-based cruise controller (CC) is used to generate the desired pedal or brake command to track the reference speed.

The second mode is adaptive cruise control mode (referred to as ACC mode), where a PI controller is designed to track a pre-defined reference distance headway $d_{\text{ACC,ref}}$ defined as

$$d_{\text{ACC,ref}} = \tau_{\text{ACC}} v_f + d_{\text{ACC}}, \tag{5.1}$$

with τ_{ACC} being the desired time headway and d_{ACC} being a constant distance.

5.1.3 Description of the Hardware

Two major hardware components involved in this study are the engine, as well as the exhaust pipe and the aftertreatment system.

A 6.7-liter Powerstroke turbodiesel V8 engine from Ford Motor Co. is used for this study. The engine is controlled using speed-throttle mode, where speed and throttle demands come from the tracking controller (ACC or CC) inside the vehicle simulation, and is controlled using an AVL EMCON 400 testbed monitoring and control system. The engine speed and throttle are the only variables directly demanded to the engine. The engine control strategy for normal warmed-up conditions in the engine control unit (ECU) is active and is not modified for this study. Specifically, the EGR level and urea injection rate are controlled by the ECU strategy, and the strategy does not change with the selection of the driver model or the optimized speed trajectory.

A high-fidelity, AC electric dynamometer couples the physical engine with the simulation mod-

[1] We abuse the notation of E^{2}C in this chapter. Depending on the context, it can mean 1) the E^{2}C planning algorithm, 2) the Matlab/Simulink instance that implements the E^{2}C planning algorithm, or 3) the driving mode when E^{2}C planning algorithm is activated.

els in real time. The engine output torque is measured by the dynamometer and sent back to the Matlab/Simulink instance integrated with AVL EMCON.

The SCR-based aftertreatment system lies at the downstream of the exhaust pipe and includes a diesel oxidization catalyst (DOC), a urea injector, a urea mixer, and an SCR system, as shown in Fig. 5.2. The temperature at the exhaust pipe downstream (also at the DOC upstream) as shown in

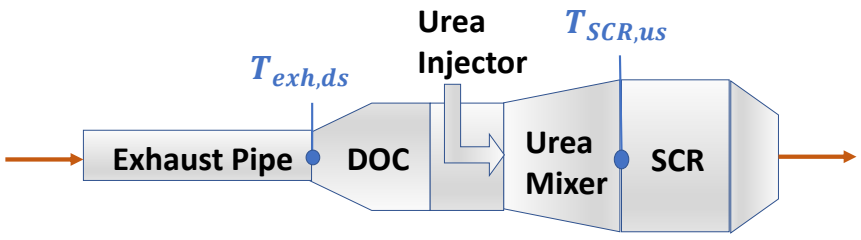

Figure 5.2: A schematic of the aftertreatment system and the locations of the thermal couples.

Fig. 5.2 is measured by a K-type thermal couple from Omega [65] and sent back to the EMCON computer. This temperature signal is involved in the control loop when E^{2}C speed planning mode is activated.

For other key performance measurements, fuel rate and engine NOx concentration signals are both from ECU sensors, tailpipe NOx is measured by AVL SESAM i60 FT SII, a Fourier-Transform InfraRed (FTIR) exhaust gas measurement system [9].

5.2 Implementation of the E^{2}C Algorithm

Due to the non-linearity in the turbine thermal dynamics, the optimization problem presented in (6.6) is a nonlinear optimization problem with a nonlinear objective function and linear constraints. It is solved using the Sequential Quadratic Programming (SQP) algorithm. With the optimal acceleration trace in the prediction horizon, the optimal speed trace is calculated using the system dynamics and the initial velocity. Details of the implementation of the speed planning algorithm is described in this section.

With the linear longitudinal dynamics presented in (2.1), if we define vectors V and P as

$$\begin{cases} V = \begin{bmatrix} v_{\mathrm{f}}(0|t) & v_{\mathrm{f}}(1|t) & \cdots & v_{\mathrm{f}}\big((N_{\mathrm{P}}-1)|t\big) \end{bmatrix}^T \\ P = \begin{bmatrix} p_{\mathrm{f}}(0|t) & p_{\mathrm{f}}(1|t) & \cdots & p_{\mathrm{f}}\big((N_{\mathrm{P}}-1)|t\big) \end{bmatrix}^T \end{cases} \tag{5.2}$$

to represent the follower velocity and position traces in the prediction horizon, respectively, then V and P are both affine functions of the decision variable U. This means all constraints on speed and position in (6.6b)-(6.6e) are linear constraints on U. Then, the optimization problem in (6.6) is abstracted as:

$$\min_{U} \quad \mathbf{J}(t) = f_{\mathrm{abs}}(U) \tag{5.3a}$$

$$\text{subject to} \quad A_{\mathrm{abs}}U \leq b_{\mathrm{abs}}, \tag{5.3b}$$

where f_{abs} is a nonlinear function, and all constraints on acceleration, speed and position are summarized with $A_{\mathrm{abs}}U \leq b_{\mathrm{abs}}$.

Problem (5.3) is solved using the SQP approach. A similar implementation of the SQP algorithm for a general nonlinear MPC problem with nonlinear system dynamics in a real-time iteration scheme has been presented in [26], but in this work, the decision variable is selected to be only the actuator value U to avoid nonlinear constraints, whereas the decision variable is selected to be the union of U and states in [26].

Problem (5.3) is approximated by a sequence of Quadratic Programming problems (QPs) with a guess U_{guess}:

$$\min_{\Delta U} \quad \frac{1}{2}\Delta U^T \mathbf{H} f_{\mathrm{abs}}\Big|_{U_{\mathrm{guess}}} \Delta U + \nabla f_{\mathrm{abs}}^T\Big|_{U_{\mathrm{guess}}} \Delta U \tag{5.4a}$$

$$\text{subject to} \quad A_{\mathrm{abs}}(\Delta U + U_{\mathrm{guess}}) \leq b_{\mathrm{abs}}, \tag{5.4b}$$

where $\mathbf{H} f_{\mathrm{abs}}$ and ∇f_{abs} represent the Hessian matrix and the gradient of f_{abs}. The QP problems are

solved with mpcQPsolver block in Simulink. Then, a step size $\alpha \in [0, 1]$ is computed following a line search procedure to guarantee descent [26] and U_{guess} is updated with $U_{\text{guess}} \leftarrow U_{\text{guess}} + \alpha \Delta U$. The SQP optimization process is triggered every $\Delta T_{\text{E}^2\text{C}} = 1$ s, which is the updating timestep for the E^{2}C speed planner. This iteration for updating U_{guess} terminates if the step size or the difference of objective function between two iterations is small enough, or if the problem is taking longer than $\Delta T_{\text{SQP}} = 0.7$ s to solve. We also note that this variable ΔT_{SQP} is calculated based on wall-clock time of the ego vehicle system to avoid the inaccuracy caused by discrepancy between the simulation time and wall clock time, if delay happens in the optimization process.

5.3 Experiment Design and Results

The performance of the E^{2}C speed planner is investigated assuming the leader vehicle is driving the speed profile shown in Fig. 5.3, which is comprised of an initialization part and a testing part. The initialization part contains the second bag of the FTP cycle, 60 s idle and then the first bag of the FTP cycle. During the initialization part of the cycle, the ego vehicle uses the ACC controller to follow, regardless of what mode it uses in the testing part. The purpose of running a long initialization part is to make sure that the engine and the aftertreatment system have the same warmed-up initial condition before entering the testing part. The testing part is the second bag of the FTP cycle (also called the stabilized phase) which lasts for approximately 15 minutes. Either the E^{2}C speed planner or the ACC controller is applied to decide the speed of the ego vehicle during the testing part of the cycle depending on the mode selection.

Three different weight factors ($w \in \{0.0, 0.2, 0.4\}$) are tested to study the performance of the E^{2}C speed planner as it becomes more fuel-centric ($w = 0.0$) or emissions-centric ($w = 0.4$). The ACC mode is also tested for comparison with the E^{2}C speed planning mode. The tests and their respective descriptions are summarized in Table 5.2, and related parameters for the ACC and the E^{2}C planner are summarized in Table 5.3.

An example result for computation and communication delay time is obtained in mode E^{2}C

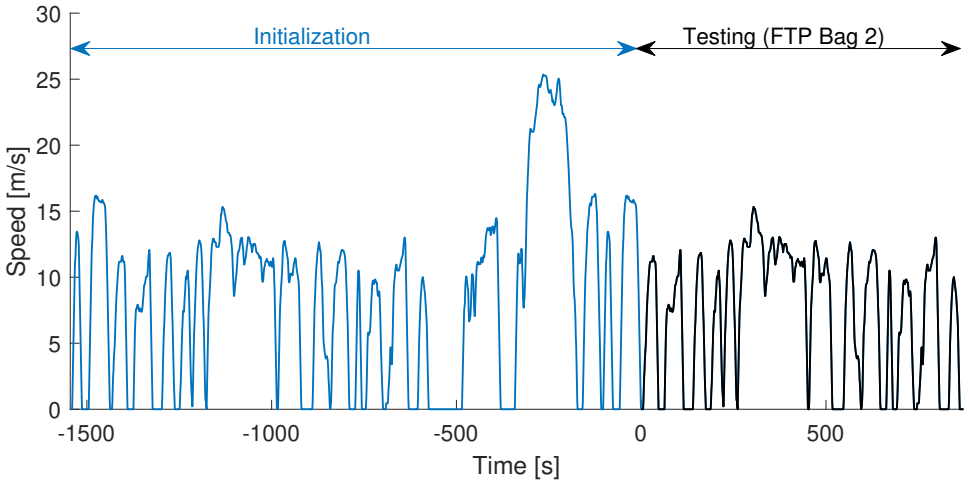

Figure 5.3: The speed profile of the tested cycle.

Table 5.2: Test cases and their respective descriptions.

i	**Ego mode**	**Description**
1	E^{2}C (0.0)	E^{2}C speed planner, fuel-centric
2	E^{2}C (0.2)	E^{2}C speed planner, weight factor $w = 0.2$
3	E^{2}C (0.4)	E^{2}C speed planner, emissions-centric
4	ACC	ACC controller

(0.2) and is shown in Fig. 5.4. The total time delay for the ego vehicle from sending the demand to receiving the optimized velocity trace corresponds to the sum of computation delay and communication delay, and is always less than 1 s, which is the updating time of the reference velocity trace optimized by E^{2}C. This is important, because we want to make sure the optimized reference speed is updated before the optimization demand at the next time step is sent. It is also observed that most of the communication delay is less than 0.06 s, and with a simulation time of 0.02 s, this means that in most cases, the speed planner (as shown in Fig. 5.1) needs no more than 3 times before it successfully sends the packet back to the ego vehicle. Regarding the computation time in the speed planner, unless it finds the local optimal solution, the optimization process terminates only after it receives the terminating demand from the vehicle after $\Delta T_{SQP} = 0.7$ s, the actual time used for computing the optimal solution is almost always smaller than 0.8 s. ΔT_{SQP} value is set

Table 5.3: Controller parameters for ACC mode and E^{2}C planning mode.

Mode	Category	Parameter(s)
E^{2}C	Horizon	$N_{\mathrm{P}} = 40$ s
	Sampling time	$\Delta T_{\mathrm{E^2C}} = 1$ s
	Headway	$\tau_1 = 1$ s, $d_1 = 0$ m $\tau_2 = 3$ s, $d_2 = 10$ m
	Speed	$\underline{v} = 0$ m/s, $\overline{v} = 30$ m/s
	Acceleration	$\underline{a_f} = -6$ m/s^2, $\overline{a_f} = 6$ m/s^2
	Temperature	$T_{\mathrm{thr}} = 230\ ^\circ\mathrm{C}$
ACC	Headway	$\tau_{\mathrm{ACC}} = 1.6$ s, $d_{\mathrm{ACC}} = 5$ m

such that the sum of computation delay and communication delay is less than $\Delta T_{\mathrm{E^2C}}$.

In the following subsections, model-in-the-loop (MIL) and hardware-in-the-loop (HIL) results are presented and compared.

5.3.1 Model-In-the-Loop Results

To test the performance of the speed planner with model-in-the-loop test, we in addition provide a model for the engine output torque and a model for the exhaust downstream temperature.

The engine output torque dynamics is modelled using a discrete first-order system with a left half plane pole and a right half plan zero. The transfer function is

$$TF_{\text{torque}}(z) = \frac{k_1 z + k_2}{z - k_3}, \tag{5.5}$$

and the parameter values are shown in Table 5.4.

To simulate the exhaust downstream temperature, the model of the turbine thermal dynamics from (2.8) is discretized and presented here

$$T_{\text{exh,ds}}(k+1) = T_{\text{exh,ds}}(k) + \frac{\Delta T}{\tau}(T_{\text{exh.ss}}(k) - T_{\text{exh,ds}}(k)), \tag{5.6}$$

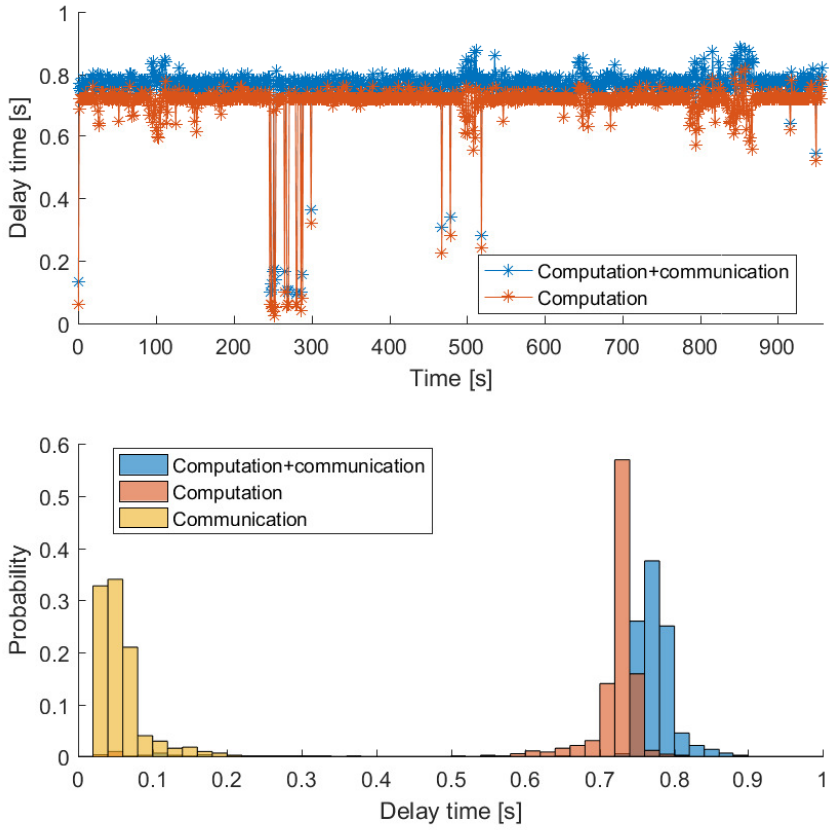

Figure 5.4: Delay performance of the implemented E^{2}C method.

where $T_{\text{exh.ss}}$ is the exhaust temperature measured at steady state, and $\tau = \frac{c_{\text{exh}}}{m_{\text{exh}}}$ is the time constant. Value of c_{exh} is shown in Table 5.4. Both $T_{\text{exh.ss}}$ and m_{exh} are simulated using look-up tables and are functions of the engine operation condition.

Figure 5.5 plots the simulated engine torque and the actual engine torque measured when running the testing cycle, and Fig. 5.6 shows the histogram of the torque difference. Quantitatively, the root mean squared error is 75.5 Nm, except for the parts with high throttle demand, the simulated torque captures the dynamics in the measured engine torque. The torque is not captured accurately when the throttle demand is high or low. Due to aging, the engine controller (stock ECU) has applied a derating mechanism to limit the high torques and avoid further damaging. Due to the time limitation of the project, the engine could not get fully reconditioned and the decision was made to proceed with the experiments. Modeling error for engine friction is causing the torque mismatch

Table 5.4: Parameters for modeling the hardware.

Model	Parameter	Value
Torque	k_1	-0.2512
	k_2	0.3002
	k_3	0.951
Temperature	c_{exh}	10^4 [g]

happens at low throttle level.

The models of engine outputs and the aftertreatment system from Chapter 2 are adopted to simulate the NOx cleaning rate inside SCR catalyst, labelled as ACC MIL and E^{2}C MIL. Simulated performances of fuel consumption and emissions, as well as some other key engine outputs when using the ACC or E^{2}C mode are shown in Fig. 5.7-(a) and Table 5.5.

Table 5.5: Effect of controller selection and calibration on major vehicle performance outputs for MIL test.

Mode	**Fuel**	**TPNOx**	**Ave.** a^2	**Ave. eng. torque**	**EngNOx**	**SCR efficiency**
	[g]	[g]	[m^2/s^4]	[Nm]	[g]	[%]
E^{2}C (0.0)	802	0.434	0.230	61.8	6.09	92.9
E^{2}C (0.2)	810	0.429	0.230	61.4	5.91	92.8
E^{2}C (0.4)	872	0.391	0.278	69.5	6.79	94.2
ACC	867	0.523	0.363	67.0	9.87	94.7

It is observed that the E^{2}C planner can generate fuel-centric, and smoother trajectories or emissions-centric, but more aggressive trajectories by tuning a single weight factor. Choosing an emissions-centric calibration ($w = 0.4$) generates 9.8% less total tailpipe NOx emissions at the cost of a 12.4% increase in average engine torque, as well as an additional 8.8% total fuel consumption compared with the fuel-centric calibration ($w = 0$), leading to a more aggressive driving style (measured by averaged squared acceleration as shown in the fourth column in Table 5.5) and worse driving comfort.

The simulated ego speed profiles, throttle position and fuel rate optimized by the various plan-

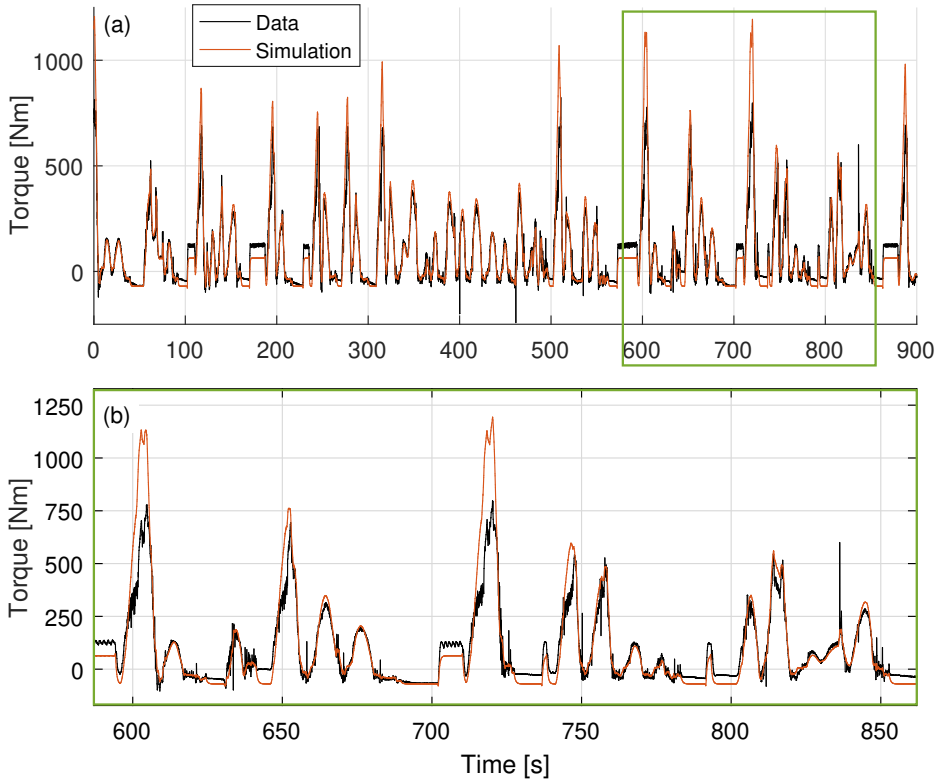

Figure 5.5: Engine torque model result compared with data.

ners are shown in Fig. 5.8. It is obvious that as the weight factor increases, the speed trajectory becomes less smooth and has higher acceleration level as well as higher fuel consumption rate. This leads to the higher temperature at exhaust downstream as well as a $13^{\circ}\mathrm{C}$ increase in SCR upstream temperature measured at the end of the trajectory, as presented in Fig. 5.9, which, in turn, reduces the total tailpipe NOx emissions.

5.3.2 Hardware-In-the-Loop Results

Figure 5.7-(b) shows the cumulative values for fuel consumption, tailpipe NOx emissions, and Table 5.6 summarizes some key vehicle performance outputs for the HIL test. From Fig. 5.7-(a,b), the same trade-off between fuel consumption and tailpipe NOx emissions is observed in HIL tests as in MIL tests. This result validates the effectiveness of the E^2C planner in studying the trade-off

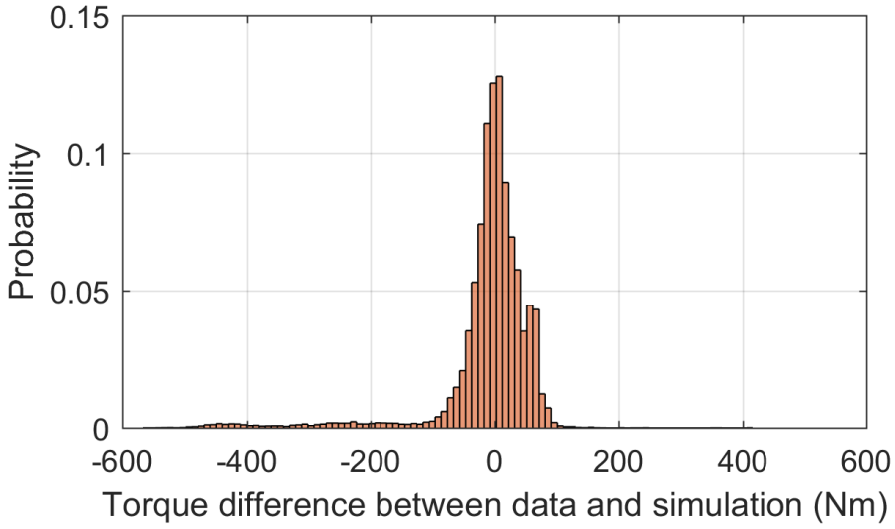

Figure 5.6: The histogram of engine torque difference between data and simulation.

between fuel consumption and tailpipe emissions.

Table 5.6: Effect of controller selection and calibration on major vehicle performance outputs for HIL test.

Mode	**Fuel**	**TPNOx**	**Ave.** a^2	**Ave. eng. torque**	**EngNOx**	**SCR efficiency**
	[g]	[g]	[m^2/s^4]	[Nm]	[g]	[%]
E^2C (0.0)	951	2.47	0.274	79.2	5.61	56.0
E^2C (0.2)	974	2.35	0.276	78.9	5.94	60.4
E^2C (0.4)	1021	2.03	0.322	87.3	6.34	68.0
ACC	1106	6.77	0.467	92.4	10.63	36.1

The optimized speed profile and inter-vehicular distance for the ego vehicle when using a fuel-centric speed planner ($w = 0.0$) are shown in Fig. 5.10-(a,b), and Fig. 5.10-(c,d) show a close-up of a violation of maximum distance constraint and one of a violation of a minimum distance constraint. A discrepancy between the demanded ego speed and the actual ego speed is observed. This is because the full vehicle model is not captured by the model used in the E^2C speed planner, and that the cruise controller has a feedback architecture. It also leads to slight violations of the headway constraints, e.g., as shown in Fig. 5.10-(c,d) at 150 s and 690 s. We note that this discrepancy could affect the overall performance of the speed planner, and a low-level

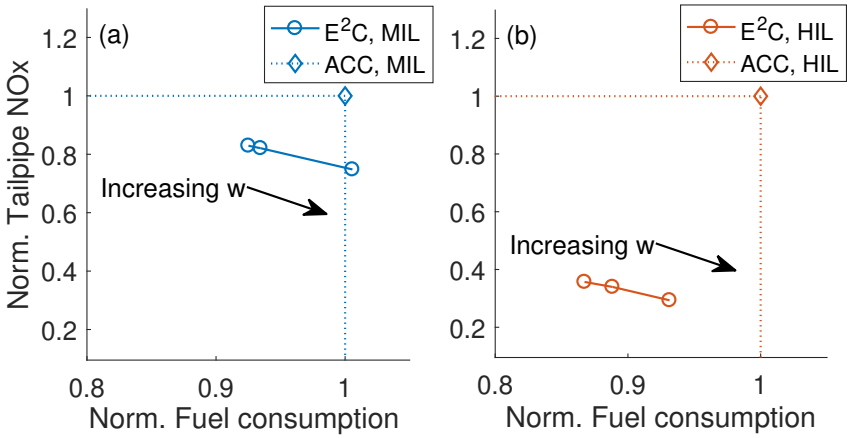

Figure 5.7: Comparison of ACC controller vs. E^{2}C speed planner (a) with model-in-the-loop test and (b) hardware-in-the-loop test. The plotted accumulative mass of fuel consumption and tailpipe emissions are normalized with the corresponding values when ACC controller is used in their respective modes. Both ACC, MIL and ACC, HIL in the plots correspond to the $[1, 1]$ point as they are normalized with respect to themselves.

cruise controller that has better tracking performance has the potential to improve the performance of the whole system.

Comparison between the ACC controller and different calibrations of the E^{2}C planner in the HIL test is presented in Fig. 5.11-5.12 and Table 5.6. Similar to what is observed in the MIL test, as the weight factor increases, the speed trace shown in Fig. 5.11-(a) becomes less smooth (which means worse driving comfort) and demands higher acceleration level and more speed variation when following the leader vehicle. To generate enough acceleration to follow the varying speed profile, a higher throttle is more frequently demanded, as we compare the case $w = 0.4$ (orange) to the case $w = 0.0$ (cyan) at times, e.g., 500-510 s (Fig. 5.11-(c)). As a result, higher instantaneous fuel rate and engine NOx emissions rate is observed, as shown in Fig. 5.11-(d) and 5.12-(d), and the cycle total fuel consumption is increased by 7.5% from 951 g to 1021 g, averaged torque level increases by 10% from 79 Nm to 87 Nm, when the cycle total engine NOx emissions is increased by 13% from 5.61 g to 6.34 g.

Despite the higher engine NOx emissions with $w = 0.4$ shown in Table 5.6, the cycle total tailpipe NOx emissions are lower, which drop by 17.8% from 2.47 g to 2.03 g. This is because of a

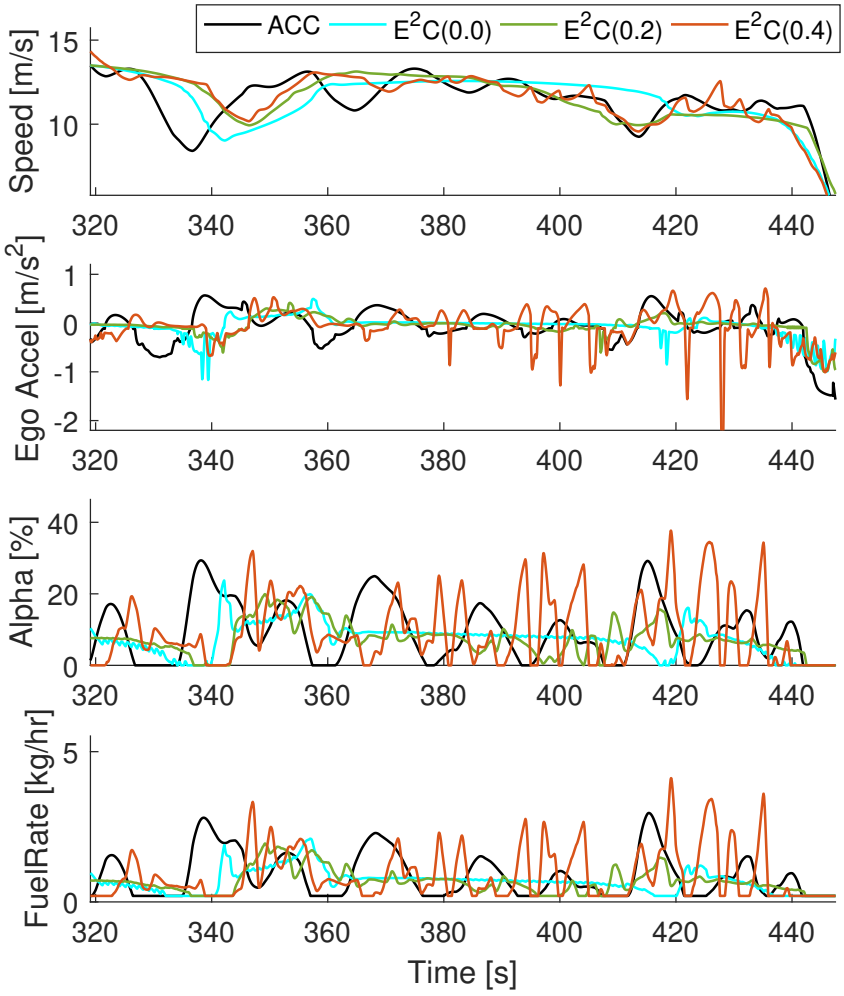

Figure 5.8: Speed, acceleration, throttle position and fuel rate performances with MIL test when using ACC controller or E^{2}C planner as the weight varies from fuel-centric to emissions-centric.

higher de-NOx efficiency, also shown in Table 5.6, resulting from a higher engine torque level and SCR temperature. The SCR upstream temperature traces during the test cycle with the different speed planner calibrations are shown in Fig. 5.12-(a). A 10°C increase is observed at the end of the test cycle when an emissions-centric planner is used as opposed to a fuel-centric, leading to a 12% absolute increase in average SCR efficiency.

Comparing the performance of E^{2}C speed planner to the ACC controller, Fig. 5.7-(b) and Table 5.6 shows a consistently lower torque level, less fuel consumption and tailpipe emissions.

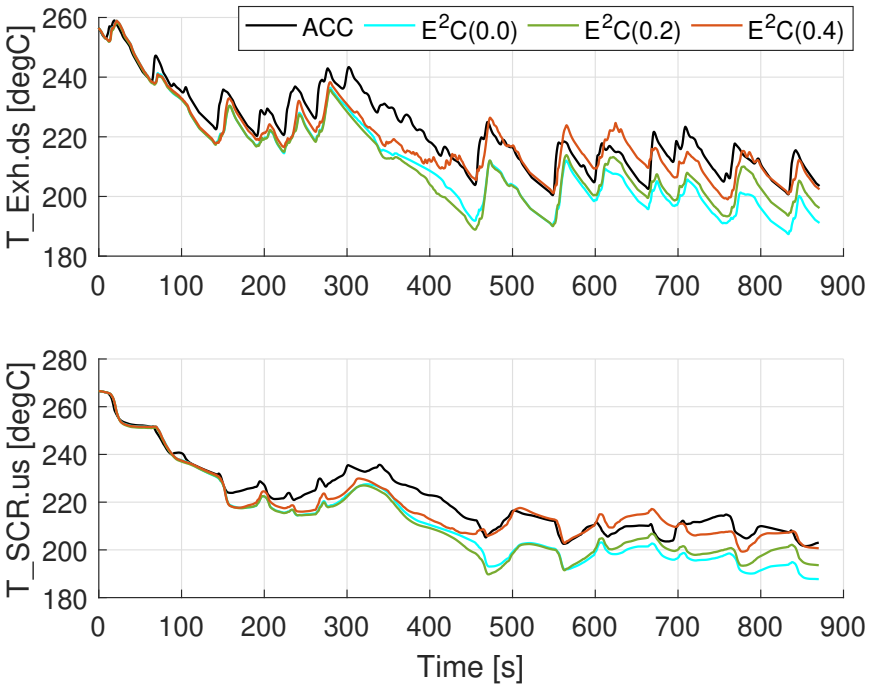

Figure 5.9: Temperature performances with MIL test when using the different speed planners.

As shown in Fig. 5.11 and 5.12-(b,c), with the ACC controller, a large throttle is usually demanded for the ego vehicle to generate a high acceleration and track the leader when the leader vehicle starts from stop. The high throttle causes a high fuel rate and high engine emissions. Tailpipe emissions also show peaks at these high pedal locations, and despite the warmer SCR temperature compared with when the speed planner is used (Fig. 5.12-(a)), a lower SCR efficiency is observed on average in the ACC test cycle compared with the cycles with the speed planner. This is because in practice, SCR cleaning efficiency is affected by not only the SCR temperature, but also the flow rate and inlet NOx concentration, and a peak in inlet NOx emissions can be very challenging for the SCR catalyst. In the MIL test, where the SCR efficiency is modelled as a pure function of temperature, tailpipe NOx emissions are underestimated when throttle demand is high. Furthermore, since the trajectory with ACC planner more frequently demands a higher throttle than those from the E^2C planner, it is expected that the benefit of the E^2C planner over ACC in tailpipe NOx emissions is underestimated in simulation. This expectation matches with the observation, as the actual benefit of E^2C over ACC with HIL tests (60% drop in emissions) is larger than that simulated with MIL

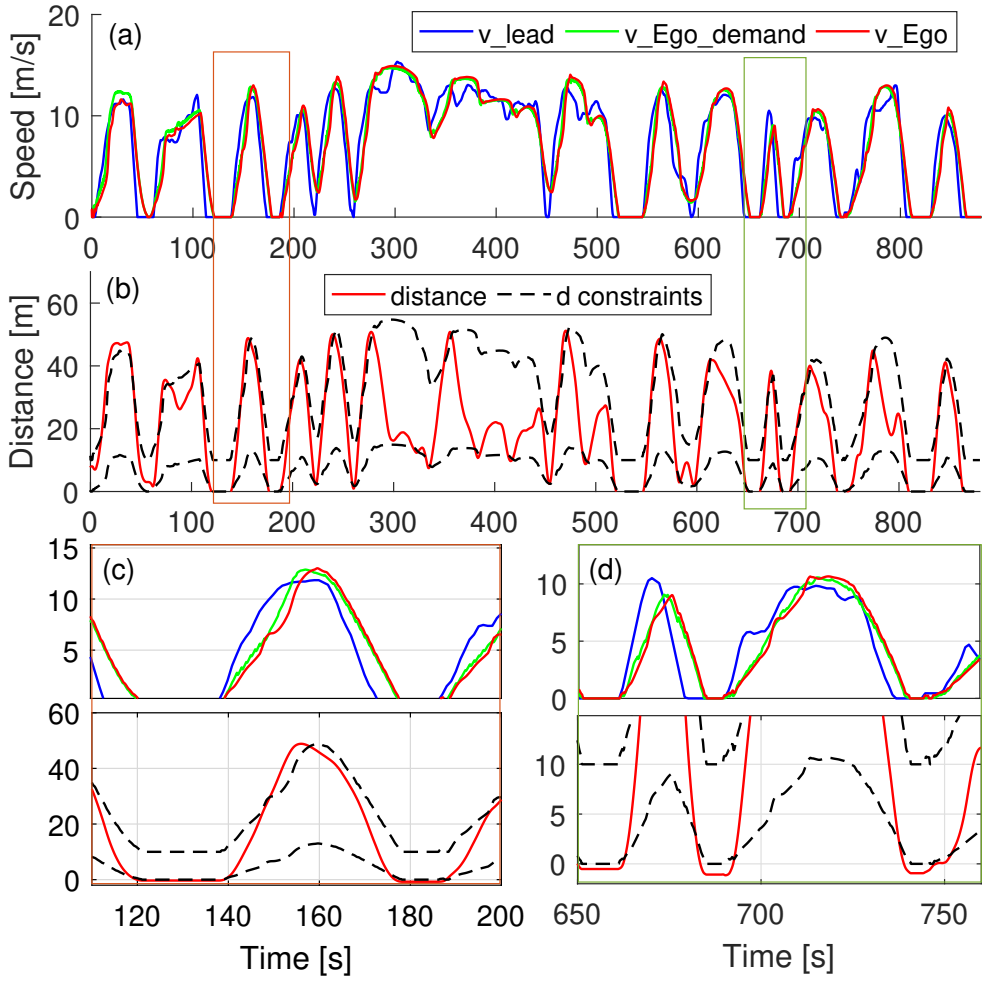

Figure 5.10: Speed and inter-vehicular distance with HIL test, when E^{2}C planning is used with fuel-centric calibration ($w = 0.0$).

tests (20% drop in emissions).

5.4 Summary

In this chapter, a hardware-in-the-loop test framework is extended with a real-time implementation of the E^{2}C-MPC strategy, and is used to explore experimentally the performance trade-off of the planning strategy in reducing fuel consumption, improving driving comfort and reducing tailpipe emissions for diesel-powered vehicles. The speed planning strategy is used as a upper-level controller that produces an optimized velocity trajectory, and a PI-based feedback cruise controller is

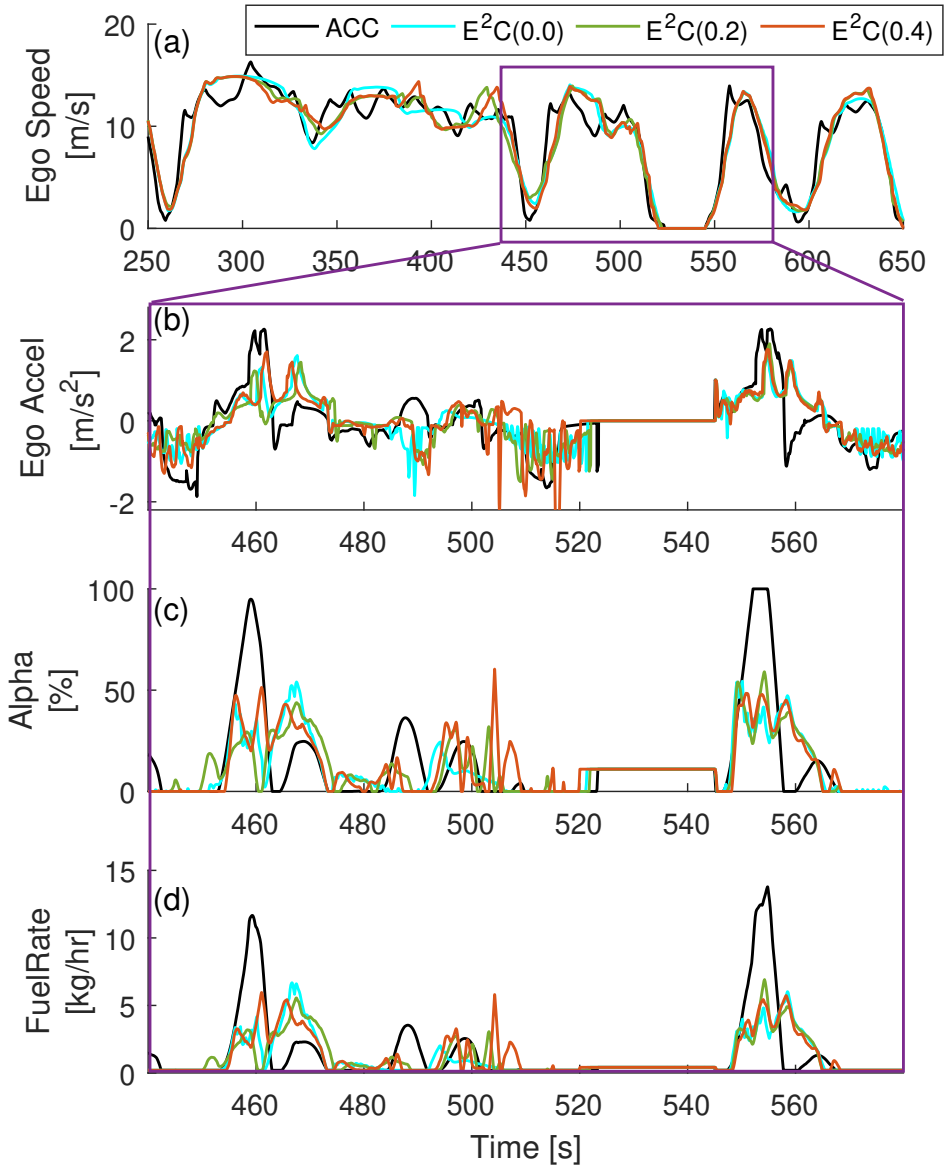

Figure 5.11: Speed, acceleration, throttle position and fuel rate performances when using the different speed planners in the HIL test.

used at lower-level to generate pedal control input to track the optimized velocity. Experiments are performed with a 6.7-liter Ford Powerstroke diesel engine, a urea-SCR based NOx aftertreatment system and a full model of a Ford F250 medium-duty truck in the loop, to provide a realistic assessment of fuel consumption, tailpipe emissions and driving style performances. Results show

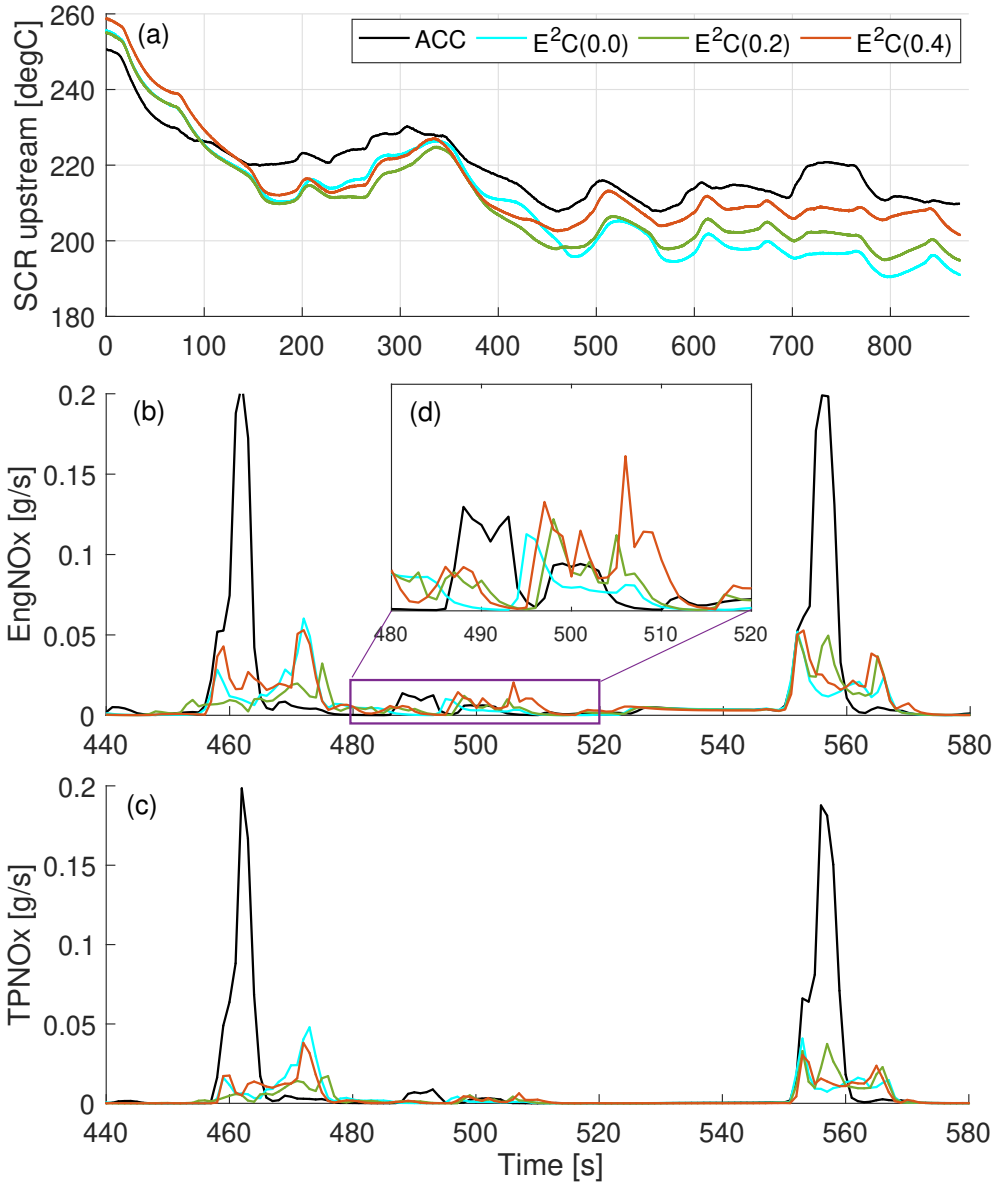

Figure 5.12: SCR temperature, engine feedgas and tailpipe NOx emissions performances when using the different speed planners in the HIL test.

that with an emissions-centric calibration, tailpipe NOx emissions is reduced by 18% with 7% more fuel consumption and 10% higher average engine torque level than a standard fuel-centric calibration. A comparative study between the speed following strategy and a PI-based adaptive cruise controller is also presented. The various calibrations of the following algorithm yield a 8-13% decrease in total fuel consumption, 6-14% decrease in average engine torque, and a 64-70%

decrease in tailpipe emissions.

As a limitation of this implementation, a non-negligible discrepancy between the desired velocity and the actual velocity is observed. While this discrepancy can hardly be avoided, we argue that instead of pairing a PI-based feedback controller with the speed planning algorithm and calculating demanded pedal, a faster low-level cruise controller with a better model that matches the derated engine can lead to better overall performance. For example in [55], a two-level control architecture is applied, where the high-level MPC controller is used to calculate reference. A low-level MPC controller coordinates multiple actuators and accounts for disturbances in the system. Since the speed planner outputs a reference velocity trajectory, the same architecture can be applied here, and the low-level PI-controller could be replaced by a model predictive controller to achieve a better tracking performance.

CHAPTER 6

Online Optimal Speed Planner with Inaccurate Preview

As mentioned at the end of Chapter 4, we have assumed that the predictive information within each prediction horizon is accurate. Unfortunately, this is never the case in the real world and the prediction error may impose a huge challenge on almost all the benefits achieved by autonomy - safety, energy efficiency and emissions. In terms of safety, inter-vehicular constraints are shown to be violated several times in a simulated cycle when a baseline formulation of MPC-based speed planner is used [61]. For fuel consumption performance, [33] shows that for an MPC-based connected cruise controller with 20 s prediction horizon, there is around 5% drop in fuel economy performance if the preview information is accurate, while it has 40% improvement in fuel economy with accurate prediction. This is even much worse than a feedback-based connected cruise controller, which is shown to have 20% improvement without using any preview information. Changes in emissions performances with preview inaccuracy have not been reported before the work in this thesis.

Due to the above reasons, it is crucial to design the speed planner such that it preserves the performance in safety, and to verify that it performs better in fuel efficiency and emissions than following an non-optimal speed trajectory.

Some researches have recognized this challenge. Authors of [61] developed a chance constrained model predictive controller (MPC) and a randomized MPC to reduce the risk of constraint violation and the fuel consumption at the same time. However, constraint violations still exist.

To resolve the constraint violation problem, provably-correct controllers have been designed when uncertainties exist in the speed preview. Controllers presented in [63, 31] generate car-following trajectories and satisfy minimum headway specifications, and controllers in [49, 59, 44] aim at avoiding collision with front vehicle. The main method used in the literature to synthesize the correct control variables is the calculation of a robust control invariant set. However, efforts typically focus only on the constraint satisfaction and only consider the vehicle kinematic performance. The only exception known to us is the work reported in [44], where the authors report 12% energy saving using their robust adaptive cruise controller compared with the non-optimized leader. However, to the best of our knowledge, there does not yet exist a fuel and emissions efficient controller that is robust to errors in preview information.

In this chapter, we design and study an modified formulation of the previously presented E^2C-MPC algorithm that is robust to inaccuracies in leader vehicle velocity and is capable of concurrently optimizing fuel consumption and emissions. The new formulation is presented, and the effect of preview error on the performance of the controller is analyzed when disturbances are applied to preview information. Different levels of preview error are generated to understand the performance of the new formulation under inaccurate preview, and an additional simulation is performed with a realistic speed predictor based on Gaussian mixture regression, such that the speed preview is generated only using history velocity information. Results show effectiveness of the controller in reducing fuel and NOx compared with the non-optimal counterpart in real-world driving scenarios.

The content of this chapter is partially based on the following papers [94, 40]:

- Zhang, X., Huang, C., Liu, M., Stefanopoulou, A. and Ersal, T., 2019. Predictive cruise control with private vehicle-to-vehicle communication for improving fuel consumption and emissions. IEEE Communications Magazine, 57(10), pp.91-97.

- Huang, C., Zhang, X., Salehi, R., Ersal, T. and Stefanopoulou, A.G., 2020, July. A Robust Energy and Emissions Conscious Cruise Controller for Connected Vehicles with Privacy Considerations. In 2020 American Control Conference (ACC) (pp. 4881-4886). IEEE.

6.1 Predictive Speed Controller Design

As described in previous chapters, the MPC-based speed controller is taking an iterative approach, deciding at every time step the optimal speed trajectory for the next horizon while satisfying predefined state and input constraints. In this chapter, we consider the following constraints on maximum/minimum acceleration and velocity:

$$a_{\mathrm{f}} \in \mathcal{U} = [-\underline{a_{\mathrm{f}}}, \overline{a_{\mathrm{f}}}], \tag{6.1}$$

$$\underline{v} \leq v_{\mathrm{f}}(k+1|t) \leq \overline{v}, \tag{6.2}$$

and following distance constraints based on a minimum and maximum time headway (τ_1, τ_2) policy [78] with (d_{c1}, d_{c2}) as the standstill distances:

$$p_{\mathrm{l}}(k+t+1) - p_{\mathrm{f}}(k+1|t) \geq \tau_1 v_{\mathrm{f}}(k+1|t) + d_{c1}, \tag{6.3a}$$

$$p_{\mathrm{l}}(k+t+1) - p_{\mathrm{f}}(k+1|t) \leq \tau_2 v_{\mathrm{f}}(k+1|t) + d_{c2}, \tag{6.3b}$$

where p_{l} and p_{f} denote the positions of the leader vehicle and the follower vehicle.

In later sections of this chapter, a robust formulation of the predictive speed controller is presented, which is designed based on the assumptions that the velocity, acceleration and deceleration of the leader vehicle are bounded, represented as

$$\underline{a_{\mathrm{l}}} \leq a_{\mathrm{l}} \leq \overline{a_{\mathrm{l}}}, \tag{6.4}$$

$$\underline{v_l} \leq v_{\mathrm{l}}(k+1|t) \leq \overline{v_l}. \tag{6.5}$$

The limits of the leader velocity are dependent on the driving scenario (e.g., speed limit of the drive cycle), and the limits of the leader acceleration and deceleration are decided by the driving pattern, which can be estimated by looking at history data of the considered drive cycle. Since the leader velocity in the prediction horizon may be inaccurate due to perturbation or prediction

inaccuracy, depending on the perturbation method and the prediction algorithm, the assumption in (6.4) and (6.5) may not be satisfied. To perform a fair comparison between the original and the robust formulation of the speed controller, in the following sections, speed preview computed through all perturbation or prediction method will undergo a filtering process before fed into the speed planning algorithm to ensure that speed and acceleration constraints in (6.4) and (6.5) are satisfied.

6.1.1 Original MPC

We consider the following optimal control problem as the original MPC, which is adopted from a similar formulation in Chapter 4:

$$\min_{U,\epsilon} \quad \mathbf{J}(t) + c_\epsilon \epsilon, \tag{6.6a}$$

$$\text{subject to} \quad a_{\text{f}}(k|t) \in \mathcal{U} \tag{6.6b}$$

$$\underline{v} \leq v_{\text{f}}(k+1|t) \leq \overline{v} \tag{6.6c}$$

$$\hat{p}_{\text{l}}(k+t+1) - p_{\text{f}}(k+1|t) \geq \tau_1 v_{\text{f}}(k+1|t) + d_{c1} - \epsilon \tag{6.6d}$$

$$\hat{p}_{\text{l}}(k+t+1) - p_{\text{f}}(k+1|t) \leq \tau_2 v_{\text{f}}(k+1|t) + d_{c2} + \epsilon \tag{6.6e}$$

$$\epsilon \geq 0 \tag{6.6f}$$

$$a_{\text{f}}(0|t) \in \mathcal{U} \tag{6.6g}$$

$$\text{System dynamics}, \tag{6.6h}$$

$$\text{for } k = 0, 1, ..., N_{\text{P}} - 1. \tag{6.6i}$$

$\mathbf{J}(t) = \sum_{k=0}^{N_{\text{P}}-1} \Big(a(k|t)^2 + w(T_{\text{TB}}(k|t) - T_{\text{thr}})^2 \cdot I_{\text{TB}}(k) \Big)$ as previously defined in (4.8), $U = \begin{bmatrix} a_{\text{f}}(0|t) & a_{\text{f}}(1|t) & \cdots & a_{\text{f}}\big((N_{\text{P}}-1)|t\big) \end{bmatrix}^T$ and ϵ are the decision variables of the optimal control problem. $\hat{p}_{\text{l}}$ is the prediction of the position of the leader (p_{l}) calculated using the speed preview, and we assume the leader follows the same dynamics as the follower. (6.6b)-(6.6e) are essentially the constraints (6.1)-(6.3b) when the prediction of position instead of the actual position

is available.

Different from Chapter 4, a slack variable ϵ is used here to change a hard (distance) constraint into a soft one and penalize the constraint violation in the cost function with a scaling factor c_ϵ. A large value for c_ϵ is chosen. Introducing ϵ avoids feasibility problems that may happen when hard constraints are used. Note that a feasible solution to this optimal control problem can always be found, but feasibility does not guarantee the satisfaction of the constraints (6.3a)-(6.3b) as $\hat{p}_\mathrm{l}$ may not be equal to p_l.

After solving for the optimal U, only $U(1) = a_\mathrm{f}(0|t)$ is applied to the follower vehicle, and then the MPC is solved again with updated states. For the original MPC, we do not impose any additional constraint on $a_\mathrm{f}(0|t)$ except the pre-defined constraint (6.1).

6.1.2 Robust MPC

Because of the inaccurate speed preview, using the original MPC formulation above may lead to violation of the speed or position constraints, or even worse, collisions. To avoid possible violation of the distance constraints in the executed follower vehicle profile, we first use a feedback controller to compute the safe action set $\mathcal{U}^*(t)$ at time t:

$$\mathcal{U}^*(t) = \mathcal{U}^*(d(t), v_\mathrm{f}(t), v_\mathrm{l}(t)). \tag{6.7}$$

The set $\mathcal{U}^*(t)$ denotes the set of all admissible accelerations $a_\mathrm{f}(0|t)$ at time t that ensure existence of a trajectory for the follower vehicle, which always satisfies velocity and headway constraints (6.2), (6.3a) and (6.3b) for an uncertain (but bounded) leader vehicle acceleration trajectory. More details are provided later in this section.

After obtaining $\mathcal{U}^*(t)$ from the feedback controller, we add this new constraint on $a_\mathrm{f}(0|t)$ to the

original MPC (6.6).

$$\min_{U,\epsilon} \quad \mathbf{J}(t)+c_\epsilon\epsilon, \tag{6.8a}$$

$$\text{subject to} \quad \text{Eqns. (6.6b) - (6.6f)} \tag{6.8b}$$

$$a_{\mathrm{f}}(0|t) \in \mathcal{U}^*(d(0|t), v_{\mathrm{f}}(0|t), v_{\mathrm{l}}(0|t)) \tag{6.8c}$$

$$\text{System dynamics.} \tag{6.8d}$$

The new MPC formulation in (6.8) has the following features: 1) Keeping ϵ as in the original MPC formulation ensures persistent feasibility. 2) Using (6.8c) ensures that the speed profile of the follower at time t is robust to uncertainty in the leader speed preview, as guaranteed by the definition in (6.14) as presented next. 3) Satisfaction of the distance constraints (6.6d) and (6.6e) with $\epsilon = 0$ is not guaranteed throughout the whole horizon, but is guaranteed in the executed profile.

6.1.3 Calculation of the Safe Action Set $\mathcal{U}^*$

In this section, the steps to calculate $\mathcal{U}^*$, the safe action set, is presented. The calculation is performed by first calculating a robust control invariant set inside an admissible set $\mathcal{X}$. As a first step, the definition of an invariant set is introduced.

Consider the leader-follower system with states $x = \begin{bmatrix} d & v_{\mathrm{f}} & v_{\mathrm{l}} \end{bmatrix}^T$, and system dynamics represented as:

$$\begin{aligned} &x(k+1) = Ax(k) + Ba_{\mathrm{f}}(k) + Ga_{\mathrm{l}}(k), \\ &A = \begin{bmatrix} 1 & -T_s & T_s \\ 0 & 1 & 0 \\ 0 & 0 & 1 \end{bmatrix}, B = \begin{bmatrix} -T_s^2/2 \\ T_s \\ 0 \end{bmatrix}, G = \begin{bmatrix} T_s^2/2 \\ 0 \\ T_s \end{bmatrix}, \end{aligned} \tag{6.9}$$

since it is assumed that the leader follows the same dynamics as the follower vehicle. In the

above equations, v_{l} and a_{l} represent the velocity and acceleration of the leader vehicle. The set of admissible states is defined as:

$$\mathcal{X} = \{x \in \mathbb{R}^3 : d_{c_1} + \tau_1 v_{\mathrm{f}} \leq d \leq d_{c_2} + \tau_2 v_{\mathrm{f}}, \underline{v} \leq v_{\mathrm{f}} \leq \overline{v}, \underline{v_l} \leq v_{\mathrm{l}} \leq \overline{v_l}\}. \tag{6.10}$$

The set Ω^* is a robust control invariant set of $\mathcal{X}$ if:

$$\forall x(k) \in \Omega^*, \exists a_{\mathrm{f}}(k) \in \mathcal{U}, s.t.\ x(k+1) \in \Omega^*, \forall a_{\mathrm{l}}(k) \in \mathcal{W}\big(x(k)\big), \tag{6.11}$$

where $\mathcal{W}$ is the set of possible disturbances (leader accelerations) defined as:

$$\mathcal{W}\big(x(k)\big) \stackrel{\text{def}}{=} \{a_{\mathrm{l}}(k) \in \mathbb{R}^1 : \underline{a_{\mathrm{l}}} \leq a_{\mathrm{l}}(k) \leq \overline{a_{\mathrm{l}}}, x(k+1) \in \mathcal{X}\}. \tag{6.12}$$

To find Ω^*, we introduce the $Pre(\mathcal{X})$ operator, which gives the one-step (backward) robustly controllable set of set $\mathcal{X}$:

$$\begin{aligned} Pre(\mathcal{X}) \stackrel{\text{def}}{=} \{&x(k) \in \mathbb{R}^3 : \exists a_{\mathrm{f}}(k) \in \mathcal{U}, s.t. \\ &x(k+1) \in \mathcal{X}, \forall a_{\mathrm{l}}(k) \in \mathcal{W}\big(x(k)\big)\}. \end{aligned} \tag{6.13}$$

Calculation of Ω^* relies on finding the fixed point of the $Pre(\mathcal{X})$ operator using the following iterative algorithm:

Algorithm 1 Calculation of Ω^*

Initialize $\Omega_0 = \mathcal{X}$
While $\Omega_k \not\subseteq \Omega_{k+1}$
    $\Omega_{k+1} = \mathcal{X} \cap Pre(\Omega_k)$
End
Return $\Omega^* = \Omega_{k+1}$

Calculation of $Pre(\Omega_k)$ from Ω_k is done using the Multi-Parametric Toolbox[34] in Matlab and following the steps proposed in [71].

The range of input that allows the state to remain inside Ω^*, $\mathcal{U}^*(x)$, is calculated by:

$$\mathcal{U}^*(x) \stackrel{\text{def}}{=} \{a_\text{f} \in \mathcal{U} : Ax + Ba_\text{f} + Ga_\text{l} \in \Omega^*, \forall a_\text{l} \in \mathcal{W}(x)\}, \tag{6.14}$$

with current states $x = \begin{bmatrix} d & v_\text{f} & v_\text{l} \end{bmatrix}^T \in \Omega^*$. Ω^* is represented as a union of polyhedra, the above set $\mathcal{U}^*(x)$ of a_f is a union of intervals, and the end points of $\mathcal{U}^*(x)$ can be solved using linear programming to find the maximum/minimum a_f that satisfies (6.14).

6.1.4 Numerical Problems in Calculation of Robust Control Invariant Set

All the sets above are convex polyhedra represented by linear inequalities, or non-convex polyhedra represented by unions of convex polyhedra. Although this algorithm works for a variety of systems in theory, the algorithm may not terminate due to numerical issues in practice, and manual termination may lead to an over-approximation, which means the calculated set is no more robust control invariant [63]. A way to avoid this issue and to always produce a robust control invariant set is to use the Inside-out algorithm [19, 63]. The key is to first find a "small" robust control invariant set $\tilde{\Omega}$ contained in $\mathcal{X}$, and then expand into a larger invariant set Ω^* by calculating its one-step robustly controllable set. The union of a small robust control invariant set and its one-step robustly controllable set is still robustly control invariant, as there exists a control input that will bring any point in this union back into the small robust control invariant set.

6.1.5 Numerical Example

As a numerical example, we consider the speed and acceleration constraints in (6.6) to have the parameters in Table 6.1. The range of the velocity and leader acceleration are determined by the drive style of the leader vehicle, and thus in this work, are determined by the velocity and acceleration ranges of the FTP drive cycle as shown in Fig. 6.1 and 6.2. The range of acceleration and deceleration of the follower vehicle is affected by the engine torque and brake capacity, vehicle and transmission properties, e.g., mass, wheel radius and drive ratio, as well as the gear shift logic.

Table 6.1: Parameters for the example in Section 6.1.5

Parameter	Description	Range
$\underline{v}, \overline{v}$	min,max ego speed	$0, 25$ [m/s]
$\underline{v_l}, \overline{v_l}$	min,max leader speed	$0, 25$ [m/s]
$\underline{a_{\mathrm{f}}}, \overline{a_{\mathrm{f}}}$	min,max follower acceleration	$-6, 2$ [m/s^2]
$\underline{a_{\mathrm{l}}}, \overline{a_{\mathrm{l}}}$	min,max leader acceleration	$-3, 3$ [m/s^2]
τ_1, τ_2	min,max time headway	$1, 1$ [s]
d_{c_1}, d_{c_2}	min,max standstill distance	$0, 150$ [m]
T_s	sampling time	1 [s]

Figure 2.2 in Section 2.2.1 shows the feasible acceleration range at each speed for the considered vehicle. With the vehicle speed in $[0, 25]$ m/s, the maximum achievable acceleration is 2 m/s^2, and the maximum brake is -6 m/s^2. It should be noted that by choosing the 2 m/s^2 maximum acceleration for all speed in the $[0, 25]$ m/s range, we are conservative about the follower vehicle's capability (as higher acceleration is achievable if speed is relatively low), and doing so might lead to degradation of the controller performance. However, although it is theoretically possible to calculate the invariant set Ω^* with a less conservative, speed-dependent follower acceleration range, doing so will involve much larger computation complexity. And thus in the following content of this thesis, the maximum allowed acceleration of the follower vehicle is set to be 2 m/s^2.

With the parameters in Table 6.1, the set of admissible states (6.10) is set up to be:

$$\mathcal{X} = \{x \in \mathbb{R}^3 : v_{\mathrm{f}} \leq d \leq 150 + v_{\mathrm{f}}, 0 \leq v_{\mathrm{f}}, v_{\mathrm{l}} \leq 25\}. \tag{6.15}$$

After performing the Inside-out algorithm, Ω^* used in this chapter is a union of polyhedra shown in Fig. 6.3. As can be seen, Ω^* is a subset of $\mathcal{X}$, meaning that the follower vehicle states is satisfying a stricter constraint as defined by Ω^* in order to ensure satisfaction of constraints (6.15) when there is uncertainty in leader vehicle acceleration.

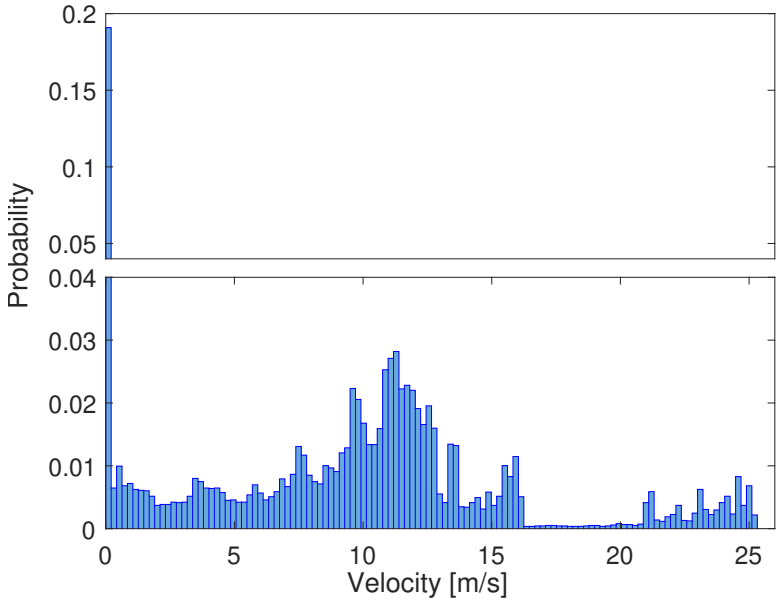

Figure 6.1: Histogram of the vehicle velocity in the FTP drive cycle.

6.2 Simulation with Perturbed Speed Preview

The performance of the proposed controller is first tested under the assumption of Gaussian system error distribution. A zero-mean Gaussian noise is added to the actual speed data, and this perturbation is applied to study the collision avoidance performance of the proposed controller, as well as the trade-off between prediction error and fuel/NOx emissions performances.

6.2.1 Perturbation Method

In this section, four levels of the perturbation error is considered, with root mean squared errors (RMSEs) being $[2, 4, 6, 8]$ m/s, and five example trajectories are generated for each RMSE level. Figure 6.4 shows an example trajectory of the perturbed velocity when applying Gaussian noise with standard deviation being 8 m/s.

6.2.2 Simulation Results

Both the original MPC and the robust MPC controllers are tested when the leader vehicle is assumed to be driving the FTP drive cycle.

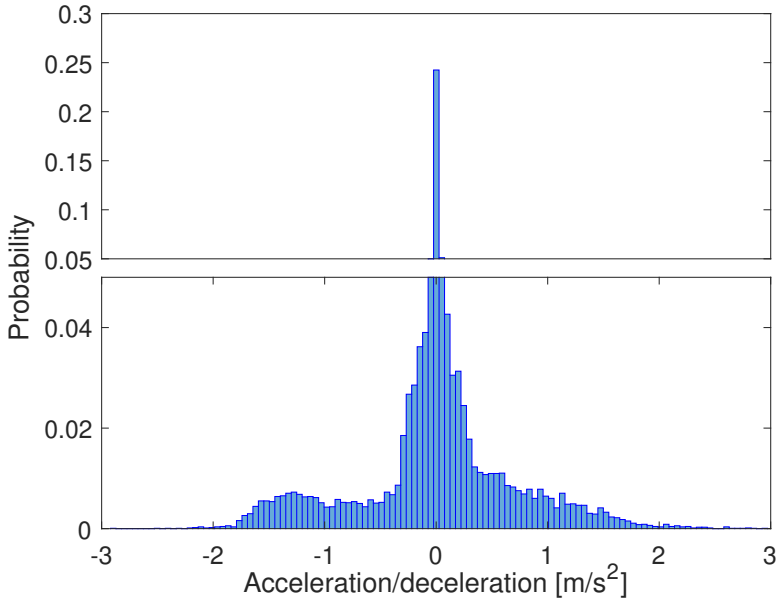

Figure 6.2: Histogram of the vehicle acceleration in the FTP drive cycle.

6.2.2.1 Robust Collision Avoidance

To evaluate the controller's performance on avoiding collision and constraint violations, the perturbation with 8 m/s standard deviation is applied to the leader velocity, and used as input to the MPC controller.

Figure 6.5 shows the total time that the minimum and maximum headway constraints are violated when using the original MPC and the robust MPC. Different prediction horizons and controller calibrations are examined for both controller formulations.

As shown, with the original MPC formulation the headway constraint violations happen with all the tested predictions and horizons, even when a longer prediction horizon is used, which generally yields less violation as the follower vehicle may know the information (although rough) of the leader vehicle much ahead of time. Thus, this observation further motivates the use of a provably robust speed controller to guarantee constraint satisfaction. The controller calibration does not seem to affect much especially with a long prediction horizon. On the other hand, using the robust MPC design, the controller can always satisfy both the pre-defined minimum and maximum headway constraints, regardless of the prediction horizon and controller calibration.

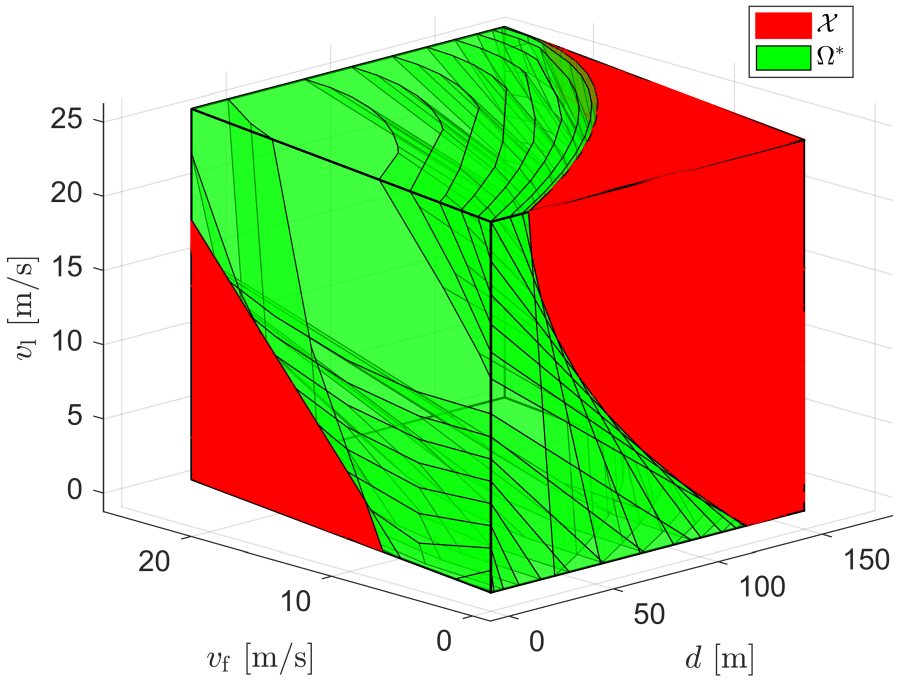

Figure 6.3: The set $\mathcal{X}$ of admissible states and the robust control invariant set Ω^* calculated through the Inside-out algorithm.

A comparison of the resulted traces from the two controller formulation is shown in Fig. 6.6. The following distance as well as the headway constraints for the whole trace are shown in Fig. 6.6-(a,b), and Fig. 6.6-(c,d) shows a close-up of a violation event that happens with original MPC but is avoided with robust MPC. With the original MPC, the follower vehicle first decreases its velocity at 1125 s (where the arrow in Fig. 6.6-(c) points at), which leads to a rapid increase in following distance. Once the distance becomes too large, it is too late for the follower vehicle to avoid violating the maximum headway constraint, even if it turns to apply the maximum possible acceleration. While for the case with robust MPC, the controller demands an earlier and also smoother acceleration, keeping the following distance between the pre-defined headway constraints.

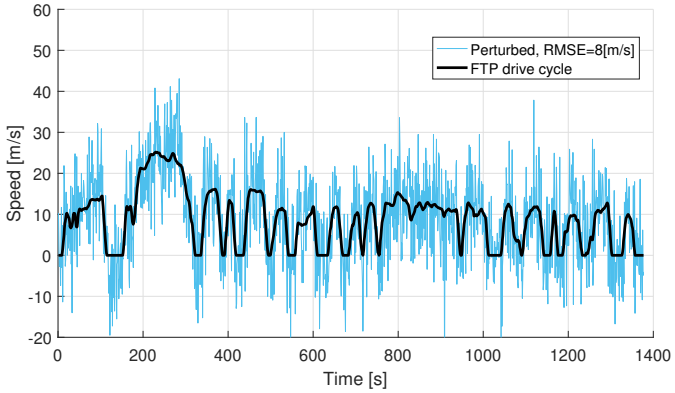

Figure 6.4: An example of a manually perturbed velocity trajectory when the leader vehicle is driving the FTP drive cycle. A zero-mean Gaussian noise with 8 m/s standard deviation is assumed.

6.2.2.2 Fuel Consumption and Tailpipe Emissions

The degradation of the controller performance due to increased uncertainty in the speed preview is shown in Fig. 6.7. The results show that generally, a monotonic increase is observed in the vehicle fuel consumption and tailpipe emissions when standard deviation of the preview error increases. Fig. 6.7 also shows how the fuel-NOx performance improves when the safe robust MPC is used, which reduces the absolute value of the input accelerations. With the original MPC, due to the large errors in the speed preview, the follower vehicle observes the leader as an aggressive driver; thus, it reacts aggressively to the leader vehicle maneuvers to keep the headway distance. This behavior results in a more energy-demanding trajectory and sacrifices the performance on fuel and emissions. This demonstrates the robustness of the presented controller formulation.

The effect of perturbation level on fuel and NOx performances of the robust speed controller is shown in Fig. 6.8. It is obvious that fuel consumption and tailpipe NOx emissions have different sensitivity levels to prediction inaccuracy. For fuel consumption, as perturbation level goes up from 2 m/s to 8 m/s, total fuel saving by using a fuel-centric calibration decreases from 20% to 10%. However, reduction of total tailpipe NOx emissions increases from 34% to 36% despite the higher level of perturbation. The intuition is that with the higher inaccuracy, the leader vehicle is considered a more aggressive driver, which causes the follower to also drive more aggressively and thus leads to a higher temperature and efficiency in the aftertreatment system. The higher SCR

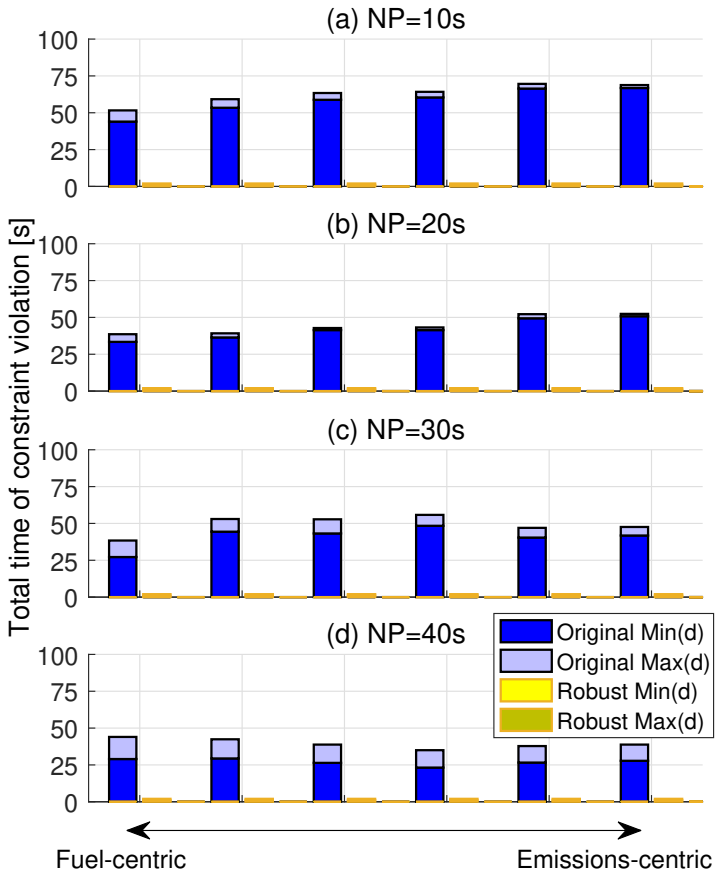

Figure 6.5: The total time of minimum and maximum distance constraint violations when using the original MPC controller and the robust MPC controller with various prediction horizons and controller calibrations. Bars labeled as Robust Min(d) and Robust Max(d) are hardly visible in all the subfigures, meaning that there is no violation with the robust MPC controller.

efficiency is the major reason for a lower tailpipe NOx emissions.

One caveat is that with $w = 0$, i.e., the fuel-centric calibration of the controller, total fuel consumption with accurate information is slightly higher than that resulting from a slightly perturbed information when $RMSE = 2$ [m/s]. In terms of solving the optimization problem, considering the actual cost directly minimized in the objective function shown in Fig. 6.9, a smaller cost is achieved with the accurate information than with the slightly perturbed speed preview. The smaller cost leads to a higher fuel consumption, because when the velocity is very smooth (when choosing $w = 0$ vs. $w = 0.1$), as shown in the comparative plot of engine visitation in Fig. 6.10, the engine

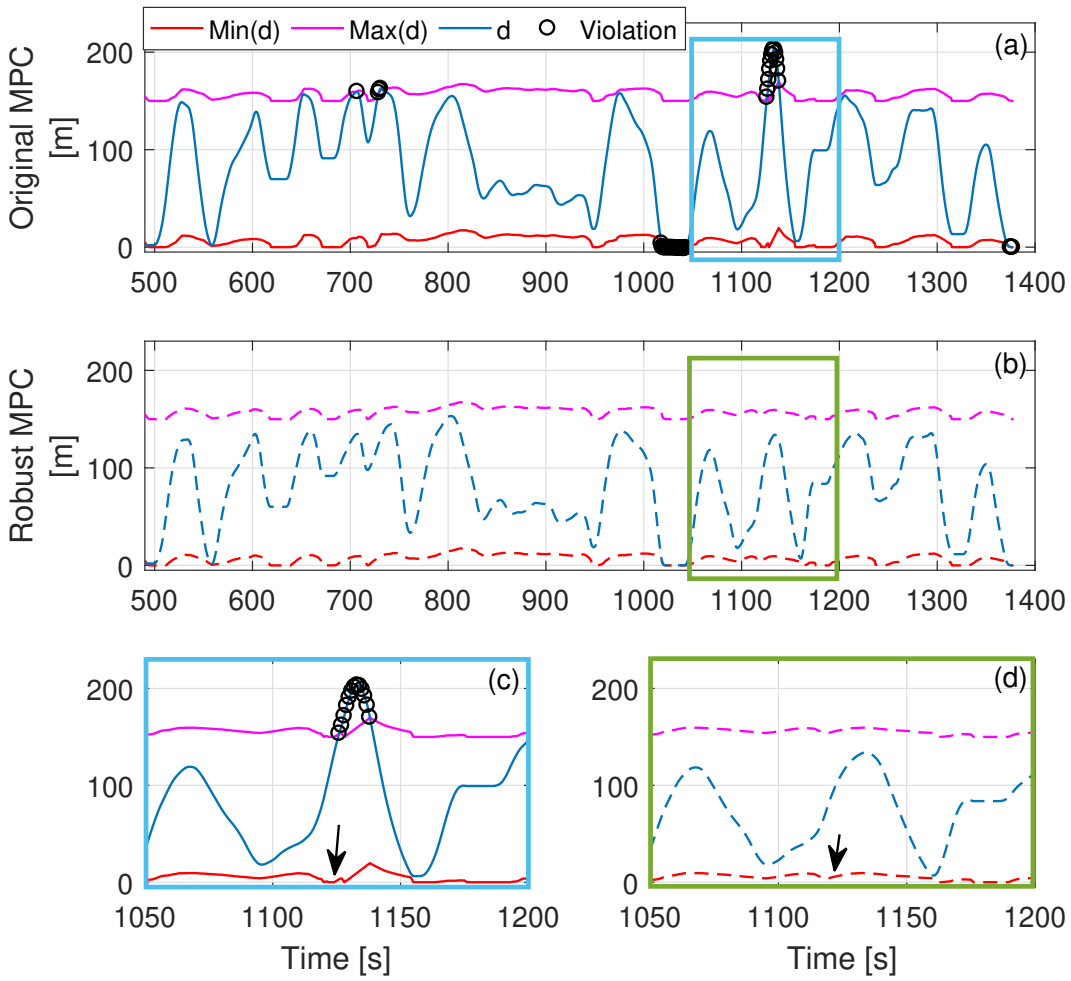

Figure 6.6: Traces of following distance and constraints with perturbation, RMSE $= 8$ m/s and equivalence factor $w = 0$. (a) with original MPC, (b) with robust MPC, (c) a close-up of a violation event with original MPC, and (d) a close-up of the same time period as in (c), but no violation happens with robust MPC.

runs more frequently at the low torque region. But since the BSFC value is higher at low torque regions, even with a slightly lower torque and power demand with $w = 0$, it causes a lower engine efficiency and a slightly higher fuel consumption value than $w = 0.1$.

6.3 Simulation with Causal Prediction

In the previous section, the robust collision avoidance property of the controller is tested, and it is observed that a larger perturbation in the prediction would lead to a worse overall performance

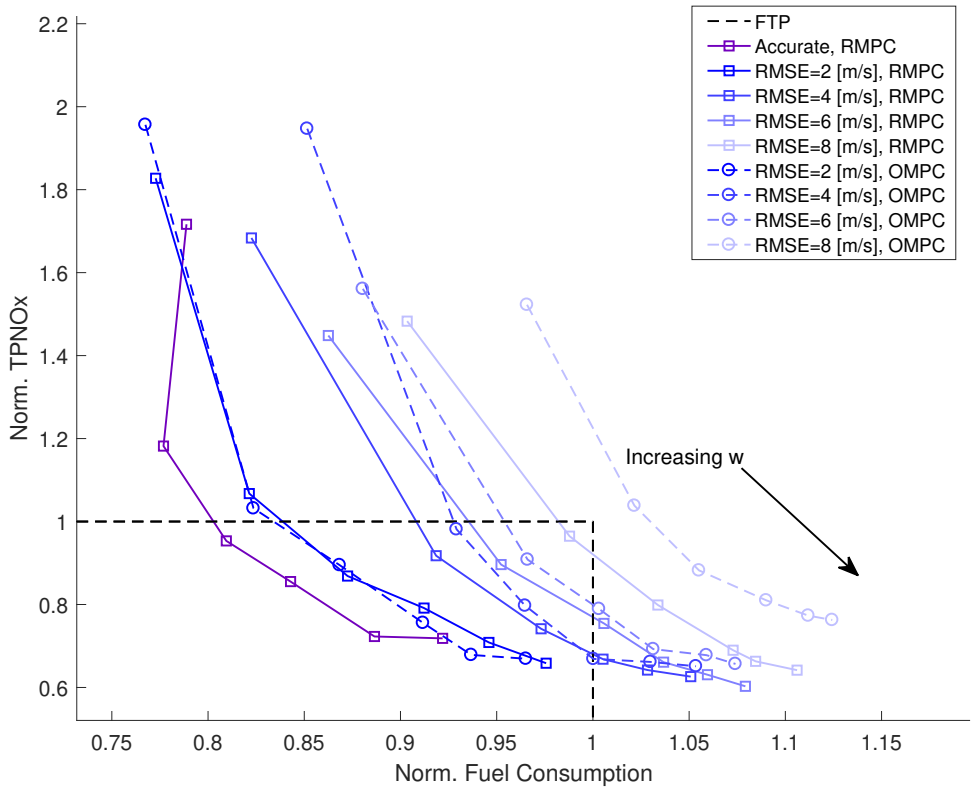

Figure 6.7: Comparison of original vs. robust speed controller with various levels of velocity perturbation. In this plot, the prediction horizon of the speed controller is 40 s. The plotted accumulative mass of fuel and tailpipe NOx are normalized with the corresponding values when the vehicle is driven with the nominal FTP speed trajectory, i.e., the same drive cycle as the leader.

on fuel consumption and tailpipe NOx emissions. However, the previous section is based on the assumption that prediction error of the leader vehicle velocity satisfies a zero-mean Gaussian distribution, which may not be true in practice. Thus, in this section, the focus is on testing the performance of the robust speed planner under a practical speed predictor based on Gaussian mixture model (GMM), which only relies the past information of the leader vehicle to generate a future prediction.

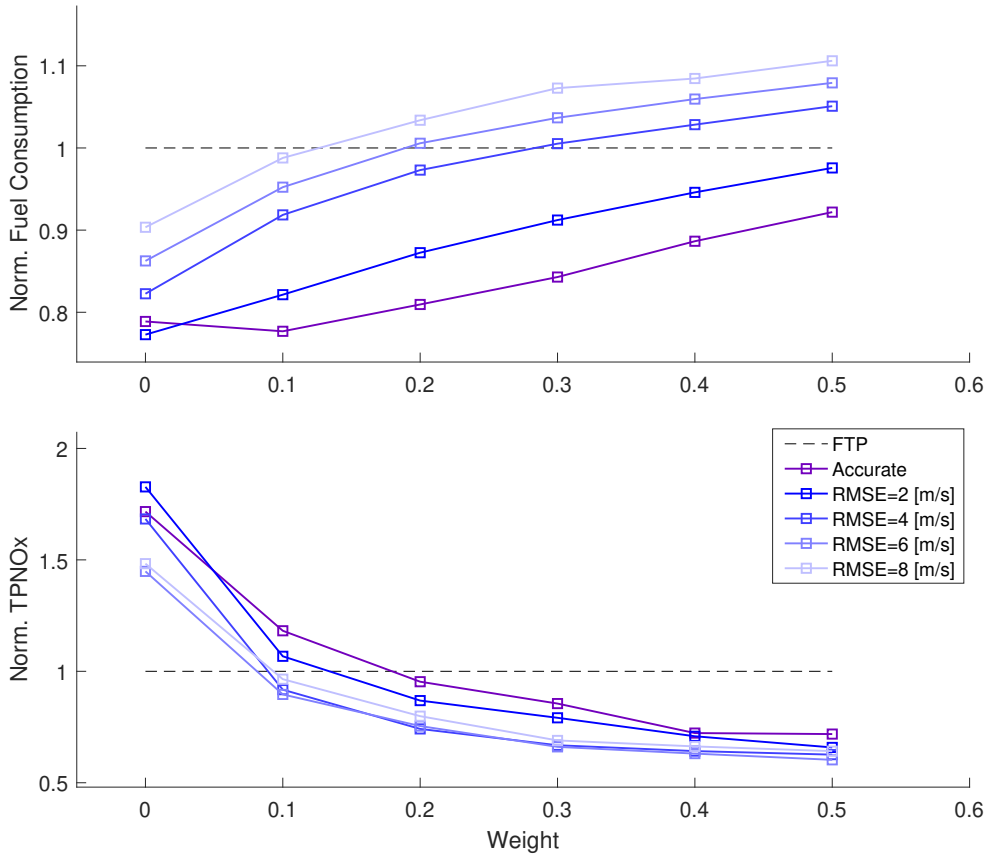

Figure 6.8: Normalized fuel consumption and tailpipe NOx emissions as a function of perturbation level and controller calibration. For this figure, 40 seconds prediction horizon and the robust controller formulation are used.

6.3.1 Velocity Prediction using Gaussian Mixture Model (GMM)

6.3.1.1 GMM for Speed Series

Gaussian mixture model models the joint probability density function of a data series as a linear combination of a finite number of Gaussian distribution components. Let

$$\mathbf{s} = \begin{bmatrix} v_l(i) & v_l(i+1) & \cdots & v_l(i+N-1) \end{bmatrix} \tag{6.16}$$

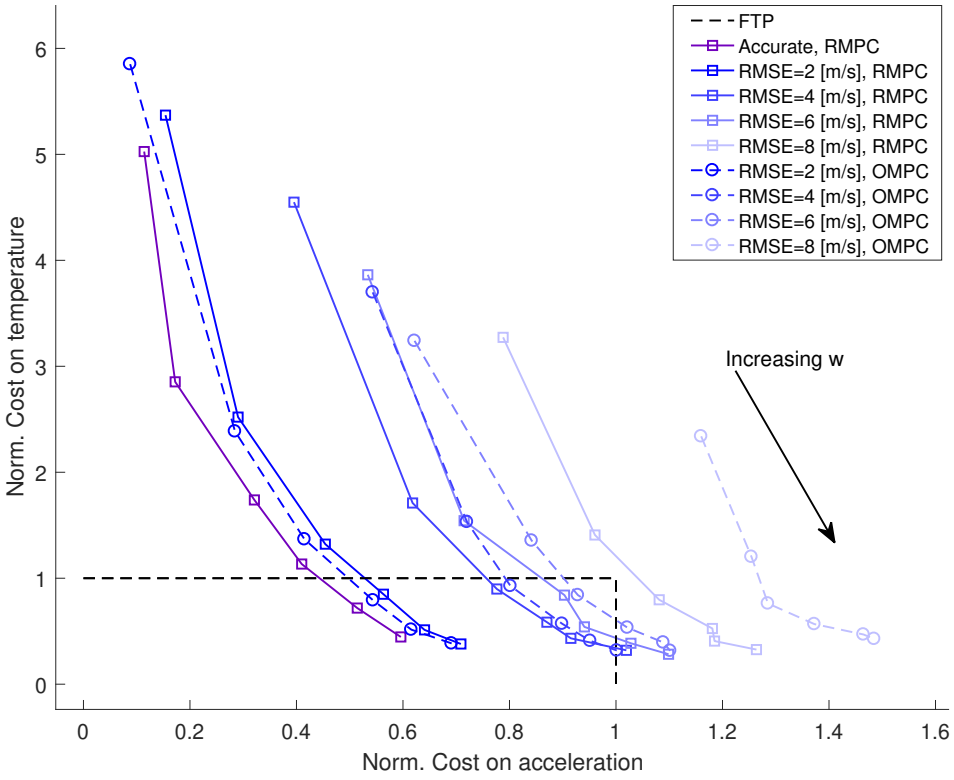

Figure 6.9: Values of the two optimized terms in the cost function when original and robust speed controller with 40 s prediction horizon and with various levels of velocity perturbation. Same as Fig. 6.7, values are normalized with the corresponding values when the vehicle is driven with the nominal FTP speed trajectory.

be a series of speed of totally N points. The probability density function $p(\mathbf{s})$ is:

$$p(\mathbf{s}) = \sum_{k=1}^{K} \pi_k \mathcal{N}(\mathbf{s}|\mu_k, \Sigma_k), \tag{6.17}$$

where K is the number of mixtures, π_k, μ_k and Σ_k are the mixing coefficients, mean vector and covariance matrix for the kth component of the distribution.

The model is trained using the Next Generation Simulation (NGSIM) dataset [24]. A two-step iterative algorithm of Expectation Minimization (EM) is applied to estimate the model parameters [11]. The mixture module implemented in scikit-learn toolbox [68] is used for model training. Both validation score and Bayesian Information Criterion (BIC) value are used as criteria to select

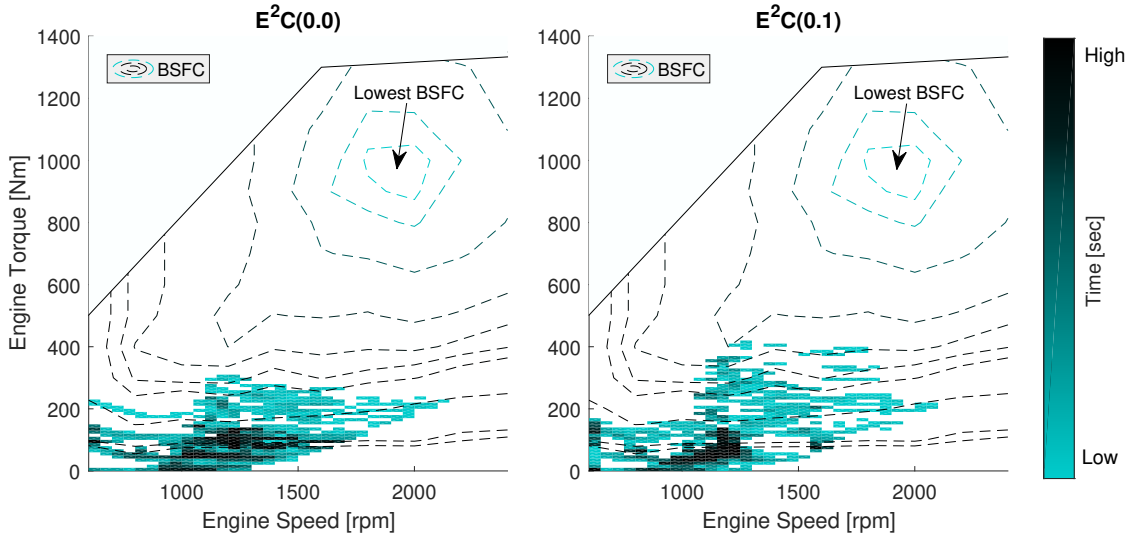

Figure 6.10: Engine visitation points with $E^2C(0.0)$ vs. $E^2C(0.1)$ when accurate information within the prediction horizon is available. The dark color represents higher visitation frequency, and the light color represents lower visitation frequency. The contour plot shows the engine BSFC map.

the best hyper-parameter, i.e., value for the number of components, to avoid overfitting the training dataset. The validation score is calculated as the per-sample average log-likelihood when the model is applied to the validation dataset [4], and a high validation score is preferred. The BIC value decreases if training score increases or model dimension decreases [74, 11], and the model with the lowest BIC value is preferred.

Figure 6.11 shows the training and validation scores, as well as the BIC values of GMM models with different number of components. Validation score achieves the highest value with 39 components, with the validation score of the model with 25 components slightly below it. The validation score also converges when using more than 25 components. BIC value is the lowest with 25 components. Since a simpler model is preferred for avoiding overfitting, GMM model with 25 components is selected.

6.3.1.2 Prediction Algorithm

With the trained model from above, Algorithm 2 describes the procedure for generating a prediction of the leader velocity $\hat{s_{f,1}}$. At each time step, the future velocity trajectory with the highest

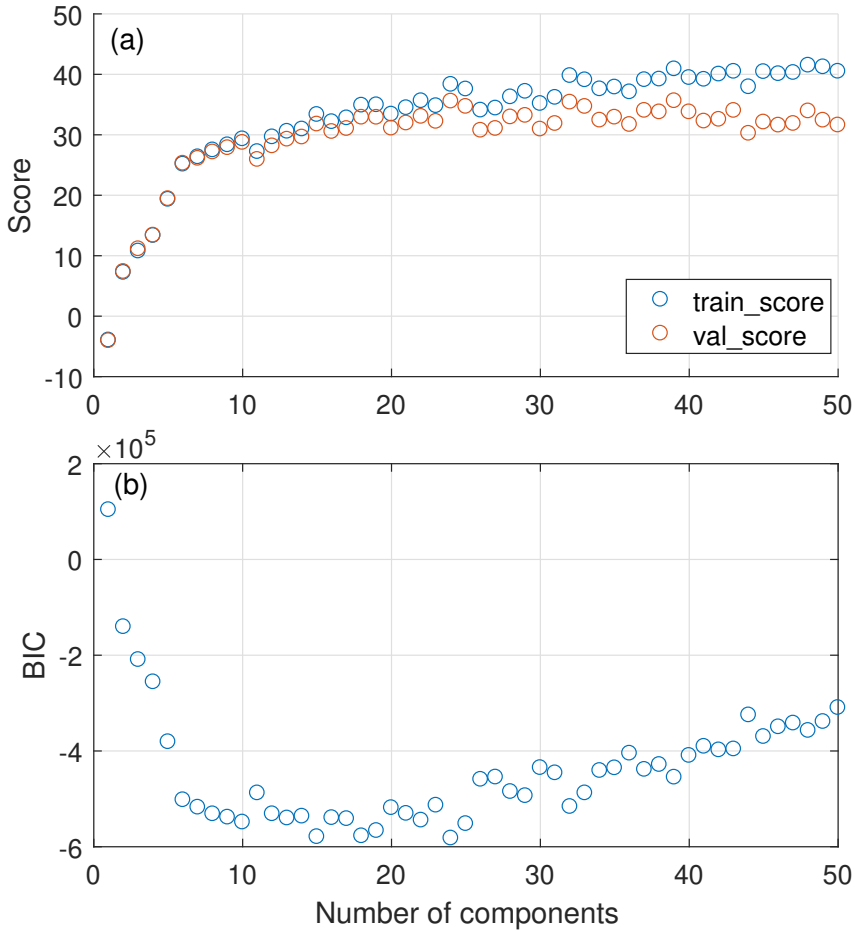

Figure 6.11: Subplot (a): Training score and validation score of GMM models with different number of components. Subplot (b): Bayesian Information Criterion (BIC) value of GMM models with different number of components.

likelihood conditioned on the past velocity is used as the prediction result. Note that, due to the filtering process mentioned in Section 6.1, the predicted velocity of the leader vehicle satisfies all the assumptions used when calculating the robust control invariant set Ω^*.

Figure 6.12 shows the prediction result for the FTP drive cycle. The solid line is the predicted mean value, which is utilized as the predicted velocity, as the mean value is the most likely outcome, and the dashed lines are showing $\pm\sigma$, the standard deviation. Figure 6.13 shows the RMSE of prediction error at each step in the prediction horizon. As observed, the error at the first 10 s is relatively smaller, but increases almost linearly with the length of prediction horizon. Once the

Algorithm 2 Prediction phase

1: Input: A Gaussian mixture model $p(\mathbf{s}) = \sum_{k=1}^{K} \pi_k \mathcal{N}(\mathbf{s}|\mu_k, \Sigma_k)$. Bounds of leader vehicle acceleration and deceleration $\overline{a_l}, \underline{a_l}$. Bounds of leader vehicle speed $\underline{v_l}, \overline{v_l}$.
2: **for** $t = 1, 2, ..., T$ **do**
3: History information of the leader vehicle's speed

$$\mathbf{s_{h,l}} = \begin{bmatrix} v_l(-N_h + 1) & v_l(-N_h + 2) & \dots v_l(0) \end{bmatrix}$$

, $\mathbf{s_{h,l}} \in \mathbb{R}^{N_h}$, N_h is the length of history information.
4: Calculate the prediction of future speed using:

$$\hat{\mathbf{s_{f,l}}} = \text{argmax}_{\mathbf{z}} p(\mathbf{z}|\mathbf{s_{h,l}})$$

, $\hat{\mathbf{s_{f,l}}} \in \mathbb{R}^{N_f}$, N_f is the prediction horizon.

prediction horizon becomes longer than 10 s, the error becomes much larger, and finally converges to 6.3 [m/s] with a very long prediction horizon.

6.3.2 Result with GMM prediction

The robust collision avoidance property of the proposed controller is studied using perturbation in Section 6.2.2.1. In this section, fuel consumption and tailpipe NOx emissions performances are discussed when the GMM predictor is applied.

The degradation of the controller performance due to inaccuracy in the speed preview is shown in Fig. 6.14. Simulation cases include prediction horizon ranges from 10 s to 40 s for both accurate speed preview and prediction from the GMM predictor. For speed planning case with accurate preview information, 30 second prediction horizon and 40 second prediction horizon are generating similar trade-off curves. This observation is also true for the case with prediction from the GMM predictor. However, when the GMM predictor is applied, simply increasing the prediction horizon does not always lead to a better trade-off curve as what happens with accurate information. In fact, Fig. 6.14 shows that for fuel-centric calibrations, e.g., $w = 0$ or 0.1, using 20 s prediction horizon is even better than 30 or 40 s. This is majorly because of two reasons. First, error in the whole prediction horizon causes deterioration of the convergence property of the optimized result, and second, there is large error in the long term prediction between 20-40 s. A maximum of 13.5%

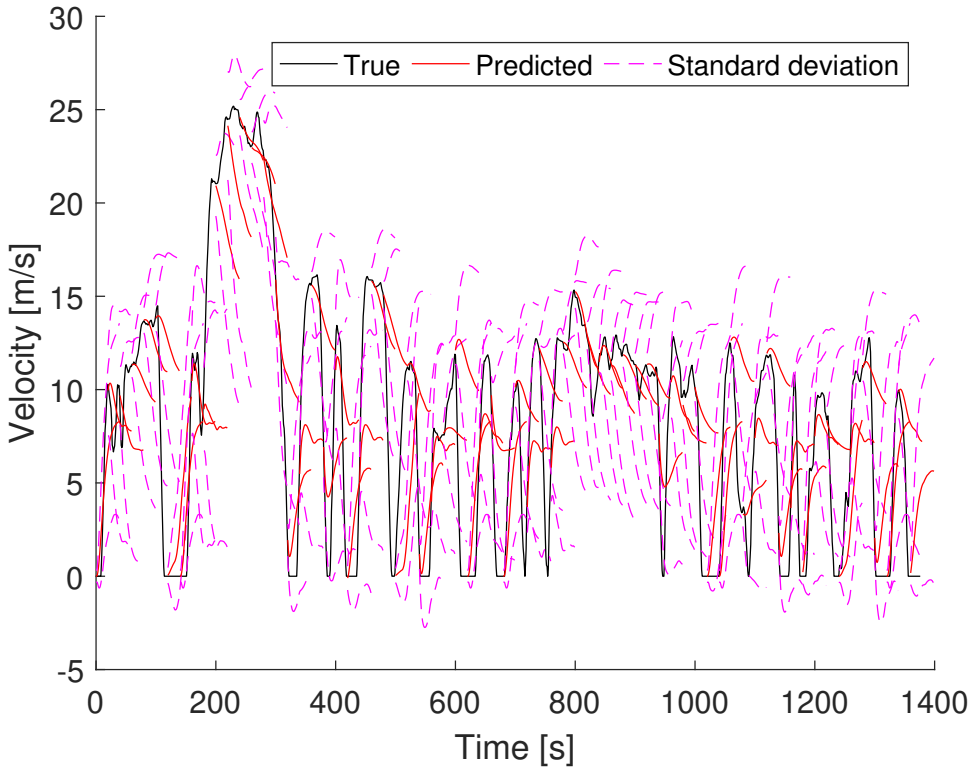

Figure 6.12: Prediction result of the FTP drive cycle.

fuel saving is achieved without increasing tailpipe NOx emissions using 20 s horizon, and 41.5% reduction in emissions is achieved at most when using 40 s horizon.

Similar to what is shown in Section 6.2.2.2, the effect of prediction inaccuracy on fuel consumption and tailpipe NOx emissions are different. With 40 seconds prediction horizon, a comparison between the controller results using accurate information and using GMM prediction is shown in Fig. 6.15. Again it is observed that an inaccurate prediction information seriously degrades the fuel saving performance of the controller, and the total fuel saving drops by 10% of the total fuel consumption during the FTP drive cycle. For tailpipe NOx emissions, however, using the GMM predictor actually improves the performance of the controller as long as the controller is calibrated to be emissions-centric. From Fig. 6.15, a more than 10% decrease in total tailpipe emissions is observed. The intuition is same as mentioned in Section 6.2.2.2. With the GMM prediction, the inaccurate preview information makes the eco-follower a more aggressive driver, which causes a higher torque level and thus higher aftertreatment temperature and efficiency. This improves the

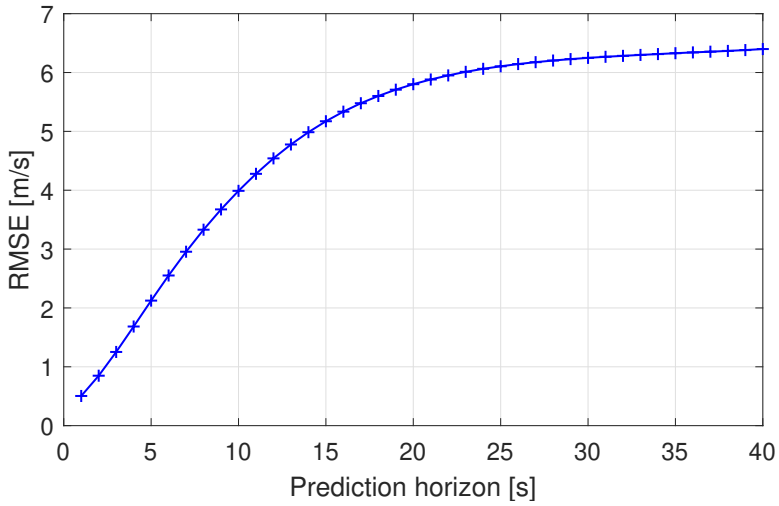

Figure 6.13: Root mean squared error (RMSE) of the prediction result.

de-NOx ability and reduces tailpipe NOx emissions.

6.4 Summary

In this chapter, an application of the predictive speed planner presented in Chapter 4 for connected and automated vehicles in a car-following scenario is studied considering the uncertainty in preview information. A robust energy and emissions-efficient optimal speed controller is presented for a diesel-powered ego vehicle and is shown in simulation to guarantee constraint satisfaction for inter-vehicular distance under preview error. Simulation is performed over the stabilized phase of the FTP drive cycle. Results show that a degradation in the overall fuel consumption and tailpipe emissions performances happens when the prediction error increases. But the effects on fuel and NOx emissions are different. It is observed that fuel reduction capability is more sensitive to the accuracy of the prediction than the emissions reduction.

Simulations also show the effectiveness of this robust controller to improve fuel and emissions performances with a Gaussian mixture regression-based speed predictor, compared with its non-optimal counterpart. It is observed that with the speed predictor instead of assuming accurate prediction, 0-13.5% of fuel saving is achieved with 0-41.5% reduction in tailpipe NOx emissions.

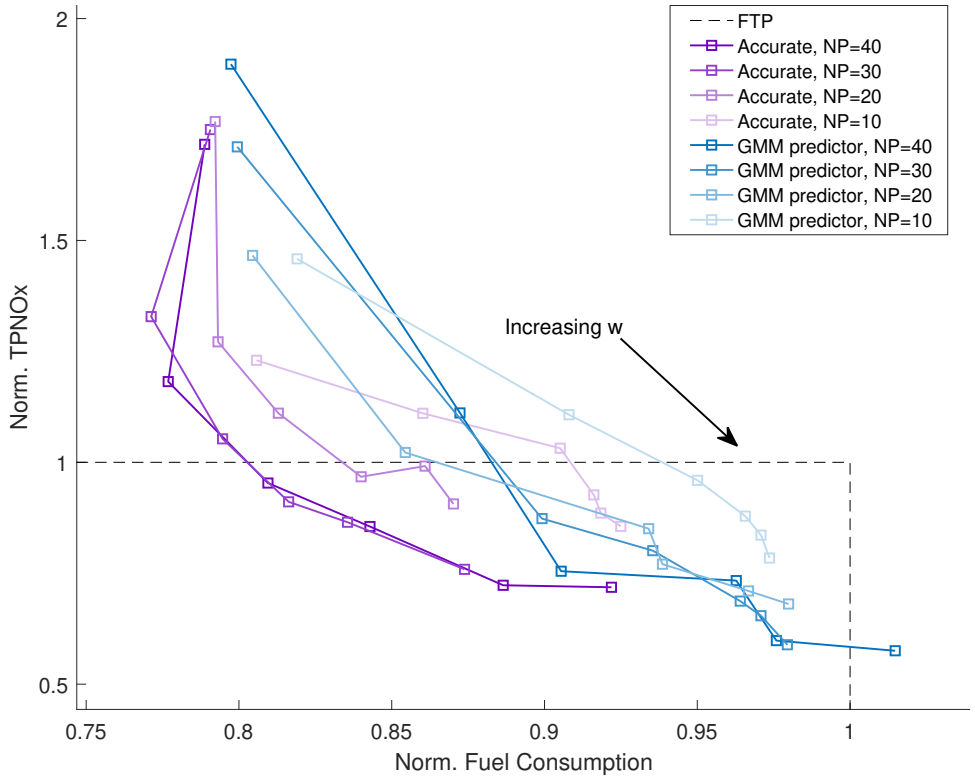

Figure 6.14: Comparison of results from the robust speed controller with GMM prediction vs. accurate prediction. Different lengths of prediction horizon are examined.

It should be noted that this is achieved using only history data, as calculation of the robust control invariant set does rely on driving pattern and vehicle parameters, e.g., velocity limits, acceleration and brake limits for the leader and ego vehicles. History data is used to identify these values as well as the parameters of the speed predictor. Hence, the dependency on real-time accurate velocity preview is relaxed. Thus, the observation shows the potential of applying the speed planner in real-world vehicle-following scenarios where accurate velocity preview of the leader vehicle is not available. It also shows the capability of the speed planner in improving fuel consumption and tailpipe emissions.

The following limitations of the current formulation should be noted. First, to calculate the control invariant set, we are assuming leader acceleration to be the only source of unknown disturbance into the system, and modeling error, computation delays, actuator delays and dynamics can

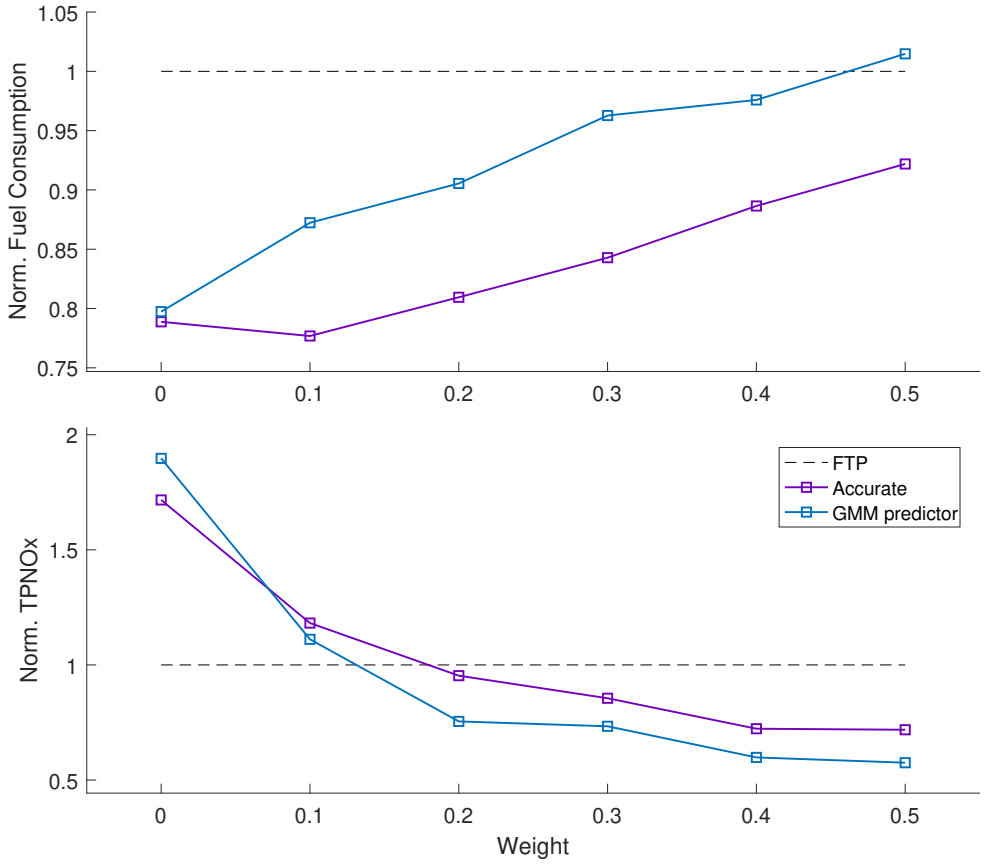

Figure 6.15: Normalized fuel consumption and tailpipe NOx emissions as a function of controller calibration. For this figure, 40 s prediction horizon and the robust controller formulation are used.

affect the result and are not considered in this chapter. Moreover, the computation is performed in discrete time, which means that constraint satisfaction is only guaranteed at the sampled time steps. The time step is selected to be 1 sec in this chapter, but in reality, a much smaller time step should be used to achieve a better approximation of the actual performance in continuous time. This will hugely increase the computation burden. In this case, some data-driving methods may provide a better approximation of the control invariant set.

CHAPTER 7

Conclusion and Future Work

7.1 Conclusion

With the emergence of vehicle autonomy and the stringent need to save energy and reduce green house gases, the goal of this thesis is to develop an optimal car-following algorithm that aims at reducing fuel and emissions for on-road automated diesel vehicles. This thesis shows the feasibility to achieve this goal by applying the presented vehicle-following algorithm with realistic and reasonable assumptions and without modifications in vehicle hardware, engine or aftertreatment system.

A model-based approach is adopted in this thesis. We first consider the most ideal case in Chapter 3, i.e., assuming full and accurate knowledge of the drive cycle, vehicle and aftertreatment model. Under this assumption, we demonstrate the fuel and emissions trade-off when driving behavior of the ego vehicle is optimized for different performance targets in an offline fashion. Total values for fuel consumption and tailpipe emissions are quantified for a specific vehicle over the FTP cycle.

Based on this observation and to relax the assumptions, Chapter 4 proposes a novel MPC-based algorithm, namely, E^2C-MPC, for online optimization of the following trajectory assuming accurate but only partial knowledge of the drive cycle, and knowledge of the accurate vehicle model. Information of the aftertreatment model is used only indirectly when coming up with a temperature threshold. Simulation results over various drive cycles are shown in this thesis and

can be indicative of a 5-15% improvement in the fuel economy with a corresponding 0-25% NOx emissions reduction.

Hardware-in-the-loop experiments are also performed to clarify the performance of the proposed planner as presented in Chapter 5. Since the detailed model and control strategy of the engine, the aftertreatment system and the low-level speed tracking controller are not fully available, the E^{2}C-MPC is not specially calibrated. The experimental results demonstrate the effectiveness of the algorithm assuming partial and accurate knowledge of the leader's drive cycle, without knowing all the details of the underlying engine and aftertreatment control strategies.

The final step taken in this thesis targets at removing the dependency on partial and accurate knowledge of the leader's drive cycle. As there is inevitable error in predicting the future speed of the leader vehicle, a robust formulation of the E^{2}C-MPC strategy is presented to keep the inter-vehicular distance between the pre-define limits. A Gaussian mixture regression-based speed prediction is applied to test the performance of the speed following strategy and the effectiveness of the algorithm without external preview information is demonstrated.

So far, an automated diesel vehicle equipped with SCR-aftertreatment system and the presented strategy is capable of balancing the reduction in fuel consumption and tailpipe NOx when following another vehicle, with partial knowledge of its own vehicle and engine properties.

7.2 Future Work

There are several limitations we mention throughout the thesis, and are summarized here, followed by some future research directions:

1. A gap for real-world implementation of the E^{2}C-MPC algorithm is that as mentioned in Chapter 4, we assume the follower vehicle could satisfy all the traffic rules by following the leader vehicle. Thus, the controller presented in this thesis is so far not capable of dealing with cases where the follower vehicle needs to stop at either stop signs or traffic intersections. Other works have presented control strategies to use signal phasing and timing information

to develop fuel-efficient speed trajectories for automated vehicles. Fuel saving is achieved by tracking a target velocity that avoids red lights [36]. Potentially, a similar idea might also be applicable here by removing the distance constraint and adding a velocity tracking term in the cost function when there is no leader vehicle or when the vehicle is near to a traffic light. The applicability of such techniques in the context of this thesis is an open research question.

2. An existing limitation for the current implementation in Chapter 5 is that a non-negligible discrepancy between the desired velocity and the actual velocity is observed. To improve the tracking performance, a potential method is to use a similar architecture as presented in [55], where the E^{2}C-MPC is the high-level controller that calculates reference setpoints, and the low-level controller can be an MPC controller that coordinates multiple actuators and accounts for disturbances in the system.

3. As mentioned in Chapter 6, the formulation presented there only deals with the uncertainty in preview information, and does not consider model uncertainty or delays in the system, e.g. computation and actuator delays. Also, the problem is solved in discrete time. These lead to two problems. First, constraint satisfaction is not guaranteed between the sampled time steps. Second, although the ego vehicle action is probably discretely determined, the leader vehicle action is continuous, and thus by approximating the leader with a discrete set of actions, we are underestimating the disturbance. In practice, using a smaller time discretization will reduce the error in calculating the control invariant set, but the calculation complexity grows, and thus theoretical approach may not be feasible. In this case, some data-driven methods may provide a better approximation of the control invariant set.

4. A necessary condition for the E^{2}C-MPC algorithm to effectively reduce tailpipe emissions when calibrated to be more emissions-centric is that an increase in SCR temperature leads to an increase in the de-NOx efficiency, and more importantly, the increase in efficiency should be large enough such that the effect of efficiency change dominates the increase in engine

NOx emissions caused by the change in driving behavior. This means that the proposed strategy should only be calibrated to be emissions-centric if the exhaust and aftertreatment temperatures are in appropriate ranges, and if the SCR is functioning correctly. Otherwise, the proposed strategy should be selected to be fuel-centric, and other thermal control techniques should be applied to improve the temperature in the aftertreatment system for emissions reduction.

5. In this thesis, the simulations and experiments are mainly studied over the FTP drive cycle. It would be interesting to also examine the other drive cycles and study the types of the drive cycle where the proposed method performs best. Moreover, considering the other NOx reduction method via modified strategy inside the engine or aftertreatment system, it would be interesting to understand how to combine different techniques to achieve the maximum NOx reduction with the smallest fuel consumption penalty. Specifically, a comparison between different techniques under different driving conditions would be worth studying. Besides, since the reference velocity trajectory is optimized by the E^2C-MPC and is known to the underlying engine and aftertreatment control strategies, these strategies, e.g., the urea injection strategy, may vary once we know the future trajectory of the ego vehicle. Utilizing this information and coordinating the multiple techniques and actuators can potentially improve the overall performance.

BIBLIOGRAPHY

[1] 40 cfr subpart n - exhaust test procedures for heavy-duty engines. https://www.law.cornell.edu/cfr/text/40/part-86/subpart-N. accessed: 2020-12-08.

[2] Danger ahead: The government's plan for vehicle-to-vehicle communication threatens privacy, security, and common sense. https://www.eff.org/deeplinks/2017/05/danger-ahead-governments-plan-vehicle-vehicle-communication-threatens-privacy. Posted: 2017-05-08.

[3] New products at the paris motor show. https://mercedes-benz-publicarchive.com/marsClassic/instance/ko.xhtml?relId=1001&fromOid=4912915&resultInfoTypeId=172&borders=true&styleId=5001&viewType=thumbs&sortDefinition=manualsort-1&oid=4912915&thumbScaleIndex=0&rowCountsIndex=5#toRelation.

[4] sklearn.mixture.gaussianmixture. https://scikit-learn.org/stable/modules/generated/sklearn.mixture.GaussianMixture.html#sklearn.mixture.GaussianMixture.score. accessed: 2021-4-21.

[5] Assad Al Alam, Ather Gattami, and Karl Henrik Johansson. An experimental study on the fuel reduction potential of heavy duty vehicle platooning. In *Intelligent Transportation Systems (ITSC), 2010 13th International IEEE Conference on*, pages 306–311. IEEE, 2010.

[6] Assad Alam, Jonas Martensson, and Karl H Johansson. Look-ahead cruise control for heavy duty vehicle platooning. In *Intelligent Transportation Systems-(ITSC), 2013 16th International IEEE Conference on*, pages 928–935. IEEE, 2013.

[7] Behrang Asadi and Ardalan Vahidi. Predictive cruise control: Utilizing upcoming traffic signal information for improving fuel economy and reducing trip time. *IEEE transactions on control systems technology*, 19(3):707–714, 2010.

[8] Behrang Asadi and Ardalan Vahidi. Predictive cruise control: Utilizing upcoming traffic signal information for improving fuel economy and reducing trip time. *IEEE transactions on control systems technology*, 19(3):707–714, 2011.

[9] AVL. AVL SESAM i60 FT SII. https://www.avl.com/-/avl-sesam-i60-ft-multi-component-exhaust-measurement-system. accessed: 2021-5-10.

[10] Kevin A Baumert. Navigating the numbers: Greenhouse gas data and international climate policy, washington dc. *http://www. wri. org/publication/navigating-the-numbers*, 2005.

[11] Christopher M Bishop. *Pattern recognition and machine learning*. springer, 2006.

[12] Sandro Brandenberger, Oliver Kröcher, Arno Tissler, and Roderik Althoff. The state of the art in selective catalytic reduction of nox by ammonia using metal-exchanged zeolite catalysts. *Catalysis Reviews*, 50(4):492–531, 2008.

[13] Delphine Bresch-Pietri, Thomas Leroy, and Nicolas Petit. Control-oriented time-varying input-delayed temperature model for si engine exhaust catalyst. In *American Control Conference (ACC), 2013*, pages 2189–2195. IEEE, 2013.

[14] Giovanni Cavataio, Hung-Wen Jen, James R Warner, James W Girard, Jeong Y Kim, and Christine K Lambert. Enhanced durability of a Cu/zeolite based SCR catalyst. *SAE International Journal of Fuels and Lubricants*, 1(2008-01-1025):477–487, 2008.

[15] Giovanni Cavataio, Hung-Wen Jen, James R Warner, James W Girard, Jeong Y Kim, and Christine K Lambert. Enhanced durability of a cu/zeolite based scr catalyst. *SAE International Journal of Fuels and Lubricants*, 1(1):477–487, 2009.

[16] Pingen Chen and Junmin Wang. Control-oriented model for integrated diesel engine and aftertreatment systems thermal management. *Control Engineering Practice*, 22:81–93, 2014.

[17] Pingen Chen and Junmin Wang. Coordinated active thermal management and selective catalytic reduction control for simultaneous fuel economy improvement and emissions reduction during low-temperature operations. *Journal of Dynamic Systems, Measurement, and Control*, 137(12), 2015.

[18] John N Chi. Control challenges for optimal nox conversion efficiency from scr aftertreatment systems. Technical report, SAE Technical Paper, 2009.

[19] Elena De Santis, Maria Domenica Di Benedetto, and Luca Berardi. Computation of maximal safe sets for switching systems. *IEEE Transactions on Automatic Control*, 49(2):184–195, 2004.

[20] Saravanan Duraiarasan, Rasoul Salehi, Fucong Wang, Anna Stefanopoulou, Marc Allain, and Siddharth Mahesh. Real-time embedded models for simulation and control of clean and fuel-efficient heavy-duty diesel engines. Technical report, SAE Technical Paper, 2020.

[21] Tulga Ersal, Mark Brudnak, Ashwin Salvi, Jeffrey L Stein, Zoran Filipi, and Hosam K Fathy. Development and model-based transparency analysis of an internet-distributed hardware-in-the-loop simulation platform. *Mechatronics*, 21(1):22–29, 2011.

[22] Tulga Ersal, R. Brent Gillespie, Mark Brudnak, J. L. Stein, and Hosam K. Fathy. Effect of coupling point selection on distortion in internet-distributed hardware-in-the-loop simulation. *International Journal of Vehicle Design*, 61(1-4):67–85, 2013.

[23] Leonard Evans. Driver behavior effects on fuel consumption in urban driving. In *Proceedings of the Human Factors Society Annual Meeting*, volume 22, pages 437–442. Sage Publications Sage CA: Los Angeles, CA, 1978.

[24] FHWA. Ngsim – next generation simulation. https://ops.fhwa.dot.gov/trafficanalysistools/ngsim.htm. accessed: 2020-01-20.

[25] Gianpiero Groppi, A Belloli, Enrico Tronconi, and Pio Forzatti. A comparison of lumped and distributed models of monolith catalytic combustors. *Chemical Engineering Science*, 50(17):2705–2715, 1995.

[26] Sébastien Gros, Mario Zanon, Rien Quirynen, Alberto Bemporad, and Moritz Diehl. From linear to nonlinear mpc: bridging the gap via the real-time iteration. *International Journal of Control*, pages 1–19, 2016.

[27] Jacopo Guanetti, Yeojun Kim, and Francesco Borrelli. Control of connected and automated vehicles: State of the art and future challenges. *Annual Reviews in Control*, 45:18–40, 2018.

[28] Jiadong Guo, Yunshan Ge, Lijun Hao, Jianwei Tan, Zihang Peng, and Chuanzhen Zhang. Comparison of real-world fuel economy and emissions from parallel hybrid and conventional diesel buses fitted with selective catalytic reduction systems. *Applied energy*, 159:433–441, 2015.

[29] Karsten Harder, Michael Buchholz, Jens Niemeyer, Jörg Remele, and Knut Graichen. Nonlinear MPC with emission control for a real-world off-highway diesel engine. In *2017 IEEE International Conference on Advanced Intelligent Mechatronics (AIM)*, pages 1768–1773. IEEE, 2017.

[30] Karsten Harder, Michael Buchholz, Jens Niemeyer, Jörg Remele, and Knut Graichen. A real-time nonlinear MPC scheme with emission constraints for heavy-duty diesel engines. In *2017 American Control Conference (ACC)*, pages 240–245. IEEE, 2017.

[31] Chaozhe He and Gabor Orosz. Safety guaranteed connected cruise control. In *IEEE International Conference on Intelligent Transportation Systems*, pages 549–554, 2018.

[32] Chaozhe R He, Helmut Maurer, and Gábor Orosz. Fuel consumption optimization of heavy-duty vehicles with grade, wind, and traffic information. *Journal of Computational and Nonlinear Dynamics*, 11(6):061011, 2016.

[33] Chaozhe R He and Gábor Orosz. Saving fuel using wireless vehicle-to-vehicle communication. In *2017 American Control Conference*, pages 4946–4951, 2017.

[34] Martin Herceg, Michal Kvasnica, Colin N Jones, and Manfred Morari. Multi-parametric toolbox 3.0. In *2013 European Control Conference*, pages 502–510, 2013.

[35] John B Heywood. Combustion engine fundamentals. *1ª Edição. Estados Unidos*, 1988.

[36] B. HomChaudhuri, A. Vahidi, and P. Pisu. Fast model predictive control-based fuel efficient control strategy for a group of connected vehicles in urban road conditions. *IEEE Transactions on Control Systems Technology*, 25(2):760–767, March 2017.

[37] Chunan Huang, Rasoul Salehi, Tulga Ersal, and Anna G Stefanopoulou. Optimal speed planning using limited preview for connected vehicles with diesel engines. In *14th International Symposium on Advanced Vehicle Control*, 2018.

[38] Chunan Huang, Rasoul Salehi, Tulga Ersal, and Anna G Stefanopoulou. An energy and emission conscious adaptive cruise controller for a connected automated diesel truck. *Vehicle System Dynamics*, 58(5):805–825, 2020.

[39] Chunan Huang, Rasoul Salehi, and Anna G Stefanopoulou. Intelligent cruise control of diesel powered vehicles addressing the fuel consumption versus emissions trade-off. In *2018 Annual American Control Conference (ACC)*, pages 840–845. IEEE, 2018.

[40] Chunan Huang, Xueru Zhang, Rasoul Salehi, Tulga Ersal, and Anna G Stefanopoulou. A robust energy and emissions conscious speed control framework for connected vehicles with privacy considerations. In *Proceedings of the American Control Conference*, 2020.

[41] M. A. S. Kamal, M. Mukai, J. Murata, and T. Kawabe. Model predictive control of vehicles on urban roads for improved fuel economy. *IEEE Transactions on Control Systems Technology*, 21(3):831–841, May 2013.

[42] Santhoji R Katare, Joseph E Patterson, and Paul M Laing. Diesel aftertreatment modeling: A systems approach to no x control. *Industrial & engineering chemistry research*, 46(8):2445–2454, 2007.

[43] Chang Hwan Kim, Michael Paratore, Eugene Gonze, Charles Solbrig, and Stuart Smith. Electrically heated catalysts for cold-start emissions in diesel aftertreatment. Technical report, SAE Technical Paper, 2012.

[44] Y. Kim, J. Guanetti, and F. Borrelli. Robust eco adaptive cruise control for cooperative vehicles. In *2019 European Control Conference*, pages 1214–1219, 2019.

[45] Manfred Koebel, Martin Elsener, and Michael Kleemann. Urea-scr: a promising technique to reduce nox emissions from automotive diesel engines. *Catalysis today*, 59(3-4):335–345, 2000.

[46] Dongsuk Kum, Huei Peng, and Norman K Bucknor. Optimal energy and catalyst temperature management of plug-in hybrid electric vehicles for minimum fuel consumption and tail-pipe emissions. *IEEE Transactions on Control Systems Technology*, 21(1):14–26, 2013.

[47] Dominik Lang, Thomas Stanger, and Luigi del Re. Opportunities on fuel economy utilizing V2V based drive systems. Technical report, SAE Technical Paper, 2013.

[48] Dominik Lang, Thomas Stanger, Roman Schmied, and Luigi del Re. Predictive cooperative adaptive cruise control: Fuel consumption benefits and implementability. In *Optimization and optimal control in automotive systems*, pages 163–178. Springer, 2014.

[49] Stéphanie Lefèvre, Ashwin Carvalho, and Francesco Borrelli. A learning-based framework for velocity control in autonomous driving. *IEEE Transactions on Automation Science and Engineering*, 13(1):32–42, 2016.

[50] Olivier Lepreux. *Model-based Temperature Control of a Diesel Oxidation Catalyst* . Theses, École Nationale Supérieure des Mines de Paris, October 2009.

[51] Olivier Lepreux, Yann Creff, and Nicolas Petit. Motion planning for a diesel oxidation catalyst outlet temperature. In *2008 American Control Conference*, pages 2092–2098. IEEE, 2008.

[52] Olivier Lepreux, Yann Creff, and Nicolas Petit. Model-based temperature control of a diesel oxidation catalyst. *Journal of Process Control*, 22(1):41–50, 2012.

[53] Shengbo Li, Keqiang Li, Rajesh Rajamani, and Jianqiang Wang. Model predictive multi-objective vehicular adaptive cruise control. *IEEE Transactions on Control Systems Technology*, 19(3):556–566, 2011.

[54] Shengbo Eben Li, Huei Peng, Keqiang Li, and Jianqiang Wang. Minimum fuel control strategy in automated car-following scenarios. *IEEE Transactions on Vehicular Technology*, 61(3):998–1007, 2012.

[55] Dominic Liao-McPherson, Mike Huang, Shinhoon Kim, Masanori Shimada, Ken Butts, and Ilya Kolmanovsky. Model predictive emissions control of a diesel engine airpath: Design and experimental evaluation. *International Journal of Robust and Nonlinear Control*, 30(17):7446–7477, 2020.

[56] Zihao Liu, Arash M Dizqah, Jose M Herreros, Joschka Schaub, and Olivier Haas. Simultaneous control of NOx, soot and fuel economy of a diesel engine with dual-loop egr and vnt using economic MPC. *Control Engineering Practice*, 108:104701, 2021.

[57] Grant Mahler and Ardalan Vahidi. An optimal velocity-planning scheme for vehicle energy efficiency through probabilistic prediction of traffic-signal timing. *IEEE Transactions on Intelligent Transportation Systems*, 15(6):2516–2523, 2014.

[58] Greg Marsden, Mike McDonald, and Mark Brackstone. Towards an understanding of adaptive cruise control. *Transportation Research Part C: Emerging Technologies*, 9(1):33–51, 2001.

[59] Carlos Massera Filho, Marco H Terra, and Denis F Wolf. Safe optimization of highway traffic with robust model predictive control-based cooperative adaptive cruise control. *IEEE Transactions on Intelligent Transportation Systems*, 18(11):3193–3203, 2017.

[60] Felicitas Mensing, Eric Bideaux, Rochdi Trigui, and Helene Tattegrain. Trajectory optimization for eco-driving taking into account traffic constraints. *Transportation Research Part D: Transport and Environment*, 18:55–61, 2013.

[61] Dominik Moser, Roman Schmied, Harald Waschl, and Luigi del Re. Flexible spacing adaptive cruise control using stochastic model predictive control. *IEEE Transactions on Control Systems Technology*, 26(1):114–127, 2018.

[62] Gary D Neely, Shizuo Sasaki, Yiqun Huang, Jeffrey A Leet, and Daniel W Stewart. New diesel emission control strategy to meet US Tier 2 emissions regulations. Technical Report 2005-01-1091, SAE, Warrendale, PA, 2005.

[63] Petter Nilsson, Omar Hussien, Ayca Balkan, Yuxiao Chen, Aaron D Ames, Jessy W Grizzle, Necmiye Ozay, Huei Peng, and Paulo Tabuada. Correct-by-construction adaptive cruise control: Two approaches. *IEEE Transactions on Control Systems Technology*, 24(4):1294–1307, 2016.

[64] Se H Oh and James C Cavendish. Transients of monolithic catalytic converters. response to step changes in feedstream temperature as related to controlling automobile emissions. *Industrial & Engineering Chemistry Product Research and Development*, 21(1):29–37, 1982.

[65] Omega Engineering Inc. . Thermocouple probes with miniature ceramic connectors. https://www.omega.com/en-us/temperature-measurement/temperature-probes/probes-with-integral-connectors/sicss-shx/p/SCAXL-125U-12-SHX. accessed: 2021-5-10.

[66] Varun Pandey, Bruno Jeanneret, Sylvain Gillet, Alan Keromnes, and Luis Le Moyne. A simplified thermal model for the three way catalytic converter. In *TAP 2016, 21st International Transport and Air Pollution Conference*, page 6 p, 2016.

[67] Jim Parks, Shean Huff, Mike Kass, and John Storey. Characterization of in-cylinder techniques for thermal management of diesel aftertreatment. Technical Report 2007-01-3997, SAE, Warrendale, PA, 2007.

[68] F. Pedregosa, G. Varoquaux, A. Gramfort, V. Michel, B. Thirion, O. Grisel, M. Blondel, P. Prettenhofer, R. Weiss, V. Dubourg, J. Vanderplas, A. Passos, D. Cournapeau, M. Brucher, M. Perrot, and E. Duchesnay. Scikit-learn: Machine learning in Python. *Journal of Machine Learning Research*, 12:2825–2830, 2011.

[69] Philipp Polterauer and Luigi Del Re. Emission constrained fuel optimal vehicle control with route lookahead. In *2018 Annual American Control Conference (ACC)*, pages 5510–5515. IEEE, 2018.

[70] Niket Prakash, Gionata Cimini, Anna G Stefanopoulou, and Matthew J Brusstar. Assessing fuel economy from automated driving: Influence of preview and velocity constraints. In *ASME 2016 Dynamic Systems and Control Conference*, pages V002T19A001–V002T19A001. American Society of Mechanical Engineers, 2016.

[71] Sasa V Rakovic, Eric C Kerrigan, and David Q Mayne. Reachability computations for constrained discrete-time systems with state-and input-dependent disturbances. In *2003 IEEE International Conference on Decision and Control*, volume 4, pages 3905–3910, 2003.

[72] Gokul S Sankar, Rohan C Shekhar, Chris Manzie, Takeshi Sano, and Hayato Nakada. Model predictive controller with average emissions constraints for diesel airpath. *Control Engineering Practice*, 90:182–189, 2019.

[73] Roman Schmied, Harald Waschl, Rien Quirynen, Moritz Diehl, and Luigi del Re. Nonlinear MPC for emission efficient cooperative adaptive cruise control. *IFAC-Papersonline*, 48(23):160–165, 2015.

[74] Gideon Schwarz et al. Estimating the dimension of a model. *Annals of statistics*, 6(2):461–464, 1978.

[75] Antonio Sciarretta and Lino Guzzella. Fuel-optimal control of rendezvous maneuvers for passenger cars (treibstoffoptimale annäherung von straßenfahrzeugen). *at-Automatisierungstechnik*, 53(6/2005):244–250, 2005.

[76] Thomas Stanger and Luigi del Re. A model predictive cooperative adaptive cruise control approach. In *American Control Conference (ACC), 2013*, pages 1374–1379. IEEE, 2013.

[77] Olle Sundstrom and Lino Guzzella. A generic dynamic programming matlab function. In *2009 IEEE control applications,(CCA) & intelligent control,(ISIC)*, pages 1625–1630. IEEE, 2009.

[78] Darbha Swaroop and KR Rajagopal. A review of constant time headway policy for automatic vehicle following. In *2001 IEEE Intelligent Transportation Systems Conference*, pages 65–69, 2001.

[79] Louis Tate, Simone Hochgreb, Jonathan Hall, and Michael Bassett. Energy efficiency of autonomous car powertrain. SAE Technical Papers. Technical Report 2018-01-1092, 2018.

[80] Florian Tschopp, Tobias Nüesch, Mu Wang, and Christopher Onder. Optimal energy and emission management of a diesel hybrid electric vehicle equipped with a selective catalytic reduction system. Technical Report 2015-24-2548, SAE, Warrendale, PA, 2015.

[81] Valerio Turri, Bart Besselink, Jonas Mårtensson, and Karl H Johansson. Fuel-efficient heavy-duty vehicle platooning by look-ahead control. In *Decision and Control (CDC), 2014 IEEE 53rd Annual Conference on*, pages 654–660. IEEE, 2014.

[82] United States Environmental Protection Agency. Protection of environment, 40 C.F.R, 2018.

[83] Devesh Upadhyay and Michiel Van Nieuwstadt. Modeling of a urea scr catalyst with automotive applications. In *ASME International Mechanical Engineering Congress and Exposition*, volume 36290, pages 707–713, 2002.

[84] Ardalan Vahidi and Antonio Sciarretta. Energy saving potentials of connected and automated vehicles. *Transportation Research Part C: Emerging Technologies*, 95:822–843, 2018.

[85] Joseph Vardi and WILLIAM F Biller. Thermal behavior of exhaust gas catalytic convertor. *Industrial & Engineering Chemistry Process Design and Development*, 7(1):83–90, 1968.

[86] Zhaodong Wang, Xiqun Chen, Yanfeng Ouyang, and Meng Li. Emission mitigation via longitudinal control of intelligent vehicles in a congested platoon. *Computer-Aided Civil and Infrastructure Engineering*, 30(6):490–506, 2015.

[87] H Wassen, J Dahl, and A Idelchi. Holistic diesel engine and exhaust after-treatment model predictive control. *IFAC-PapersOnLine*, 52(5):347–352, 2019.

[88] Frank Willems, Robert Cloudt, Edwin Van Den Eijnden, Marcel Van Genderen, Ruud Verbeek, Bram de Jager, Wiebe Boomsma, and Ignace van den Heuvel. Is closed-loop scr control required to meet future emission targets? Technical report, SAE Technical Paper, 2007.

[89] Frank Willems, Paul Mentink, Frank Kupper, and Edwin Van den Eijnden. Integrated emission management for cost optimal egr-scr balancing in diesels. *IFAC Proceedings Volumes*, 46(21):711–716, 2013.

[90] Lingyun Xiao and Feng Gao. A comprehensive review of the development of adaptive cruise control systems. *Vehicle system dynamics*, 48(10):1167–1192, 2010.

[91] Peng Ye, Bhaskar Prabhakar, and André L Boehman. Experimental investigation of the impact of post-injection on emissions, combustion and lubricant dilution in a diesel engine with b20 fuel. *International Journal of Engine Research*, 14(1):12–22, 2013.

[92] Michael Zabat, Nick Stabile, Stefano Farascaroli, and Frederick Browand. The aerodynamic performance of platoons: A final report. 1995.

[93] Stephan Zentner, Jonas Asprion, Christopher Onder, and Lino Guzzella. An equivalent emission minimization strategy for causal optimal control of diesel engines. *Energies*, 7(3):1230–1250, 2014.

[94] Xueru Zhang, Chunan Huang, Mingyan Liu, Anna G Stefanopoulou, and Ersal Tulga. Predictive cruise control with private vehicle-to-vehicle communication for improving fuel consumption and emissions. *IEEE Communications Magazine*, 57(10):91–97, 2019.